Master Thesis of Science

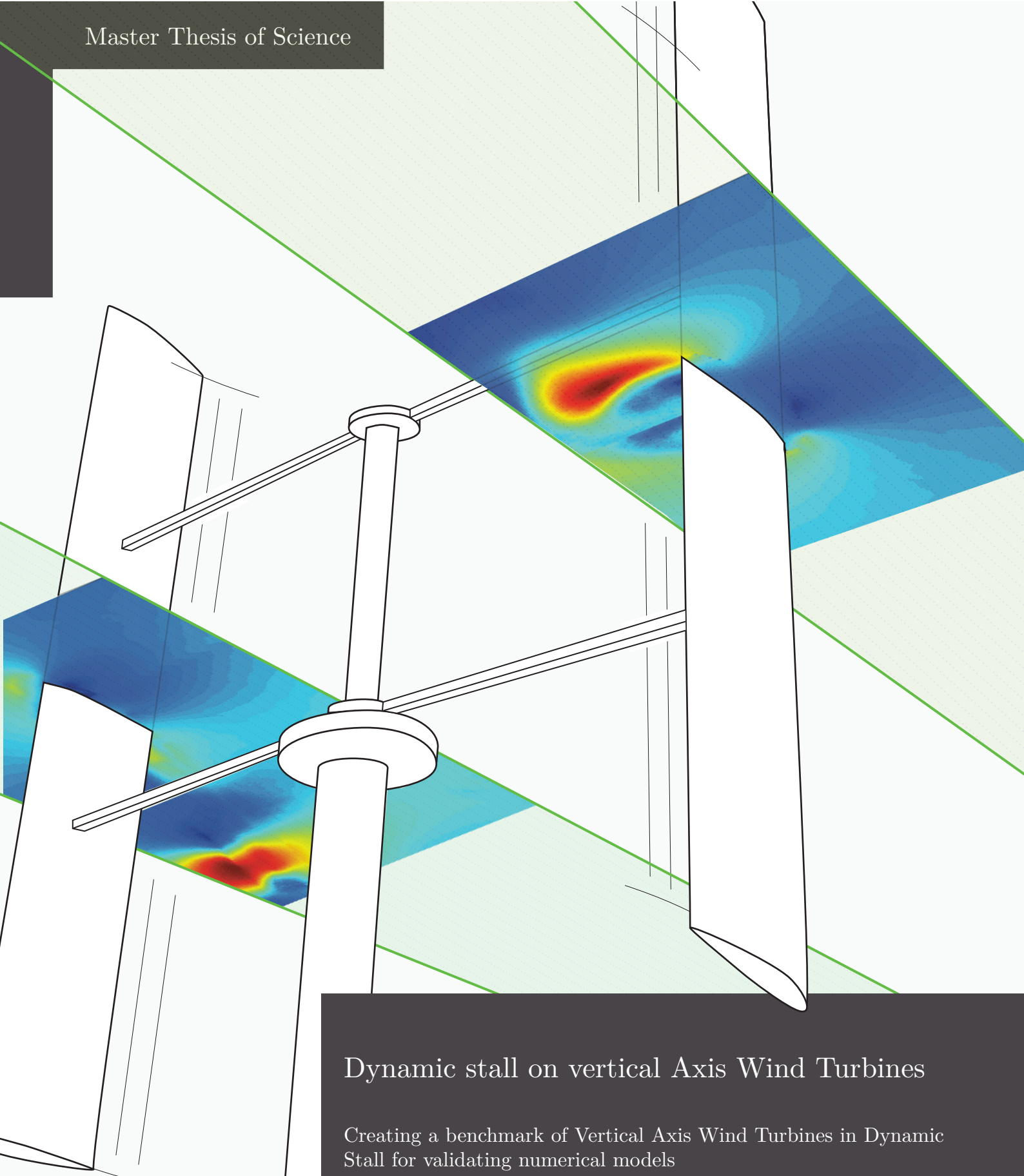

Dynamic stall on vertical Axis Wind Turbines

Creating a benchmark of Vertical Axis Wind Turbines in Dynamic Stall for validating numerical models

D. Castelein

March 26, 2015

TU Delft Delft University of Technology

DTU

EWEM

Dynamic Stall on Vertical Axis Wind Turbines

Creating a benchmark of Vertical Axis Wind Turbines in Dynamic Stall for validating numerical models

Master of Science Thesis

For obtaining the degree of Master of Science in Aerospace Engineering

D. Castelein

March 26, 2015

European Wind Energy Master - EWEM

European Wind Energy Master - EWEM
Of
Rotordesign Track

The undersigned hereby certify that they have read and recommend to the European Wind Energy Master - EWEM for acceptance a thesis entitled **"Dynamic Stall on Vertical Axis Wind Turbines"** by **D. Castelein** in partial fulfillment of the requirements for the degree of **Master of Science**.

Dated: March 26, 2015

Head of Department: _____
Prof. Dr. G.J.W. van Bussel of TUDelft

Supervisor: _____
Dr.Ir. C.J. Simão Ferreira of TUDelft

Supervisor: _____
Dr. Ir. M. Gaunaa of DTU

Reader: _____
Dr. Ir. D. Ragni of TUDelft

Reader: _____
Ir. G. Tescione of TUDelft

SUMMARY

An experimental campaign using a phase-locked Particle Image Velocimetry (2C-PIV) technique has been conducted on an H-type Vertical Axis Wind Turbine (VAWT). The turbine is operated at tip speed ratios (TSR) 4.5 and 2, at accordingly average chord-based Reynolds number of $1.6 \cdot 10^5$ and $0.8 \cdot 10^5$. At both TSR, the velocity fields are presented in the mid (symmetry) plane of the blade for eight azimuthal positions. The velocity fields are directly derived from PIV, while the loads are obtained through an integral approach presented by Noca et al.

The experiment, as well as the load determination method, is submitted to a sincere uncertainty analysis in order to validate the approach used in this thesis. This will provide future researchers a load determination method able to predict forces from PIV measurements, with masked areas in the field and in dynamic stall conditions.

The overall goal of this research was to create a benchmark from the experimentally gathered loads, for validating and comparing different numerical models. The aim of evaluating the two different TSR is identifying the effect of Dynamic Stall (DS), which is not present at the higher TSR, while dominant at the lower. The DS phenomenon makes it numerically computationally expensive to model all scales of phenomena, so a solid benchmark for a VAWT in DS is of great interest.

Velocity fields were presented for TSR of 4.5 and 2 at eight azimuthal positions. The velocities of the TSR 4.5 case are comparable to the velocity fields from the numerical inviscid panel code. This illustrates that the experiment can be compared to numerical models.

At both TSR the experimental normal forces give similar results as the numerical models predicted. For two positions, namely the 130° azimuth position at TSR 4.5 and the 90° azimuth position at TSR 2, the rotational velocity of the turbine was unsteady during the experiment. This increases the uncertainty off the load measurements at these positions, and it was therefore deemed necessary to reject the tangential force at the 90°, and all outcomes at the 130° azimuthal position. All tangential loads of the TSR 4.5 case can not be used for comparisons. The loads are small, and the relative error is dominant when calculating the mean.

The experimental results in normal direction can all be used as a benchmark for numerical models of a vertical axis wind turbine at these conditions, and for the TSR 2 also the tangential forces can be compared.

The preliminary findings from this thesis were presented on the 33rd Wind Energy Symposium at the AIAA SciTech conference in January 2015 in Kissimmee, Florida. The full paper can be found in Appendix F as a reference.

ACKNOWLEDGEMENTS

The end of an era, that is how this feels to me. Studying was not only obtaining my diploma, but also obtaining some wisdom and common sense. Although this period might have last a couple of months more than usual, I am quite certain I can say I learned more than enough about myself to appreciate these extra months.

At the beginning of the thesis, I mostly felt like this:

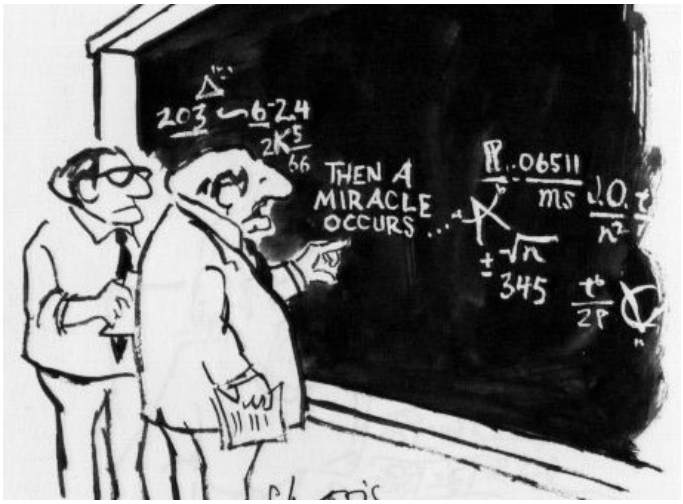

Friends, family, and supervisors helped me through this highly uncomfortable period.

For this, I really want to thank my first supervisor: Carlos Simão Ferreira, who really kept my both feet on the ground at all times, and was there for some 'wisdom' at times I really did not see any :). Thank you also for showing me that being serious does not necessarily means being uncertain. You gave me a lot of good baggage about the professional me for my future career. Mac Gaunaa, who pushed me to some other limits, although he might not even have known he did so. He was always available for a very interesting skype chat. I really want to thank you both, because without the two of you, this was never made possible.

Giuseppe Tescione and Daniele Ragni, you guys were there for me at all times. I only

had to bust your doors, and it would go open for me. I really do appreciate the time, effort, maybe even the faith you put into me and the project. Therefore, a special thanks to the both of you. Again I can say that without you both, this project was never made possible.

Then there is my family. Never on the foreground, but always in my back. If I would ever have any problem, I could go to them. Basically, that is how it went through this thesis period. The moments I really did not see any convenient way, I went to Belgium, to my family, just to relax. This would always give me insights. Thank you very much parents, sisters, Johan and grandparents for always taking so good care of me.

All friends that were there for me during this period: thank you for all the support. If it wasn't for you guys, I might have only sat behind my desk all evenings. Thank you for showing me also some very good times, and keeping that party part of me alive ;).

Tom Berdowski and Rody Kemp: Both of you kept me on the right path in your own particular way. Rody showed me the path of being myself, and the not always being too serious kind of guy, and Tom in keeping me still to work, and focussing on my project. I think that without you two, my whole experience of graduating would have been different. I really enjoyed the times I have spent with you guys in this period, and hope these times can keep on going.

Lukas Kuijken, thank you for all the good times we shared during the thesis period. We shared a lot of laughs, coffees and especially beers together to discuss the existing problems in the thesis. These moments were memorable, and helped me through some difficult times.

Klaas Akkerman, I really want to thank you in particular. You invested a lot of time and effort in me. Even when I told you times were worse than ever, you would listen, and stay put. You made my thesis look better than ever, and made me proud of my work. I hope we can share a lot of these moments in the future, and that I can help you as you helped me. Thank you so much for everything you have done for me.

To my friends, here are two quotes that I will live by:

"In the End, we will remember not the words of our enemies, but the silence of our friends." - Martin Luther King

"It is one of the blessings of old friends that you can afford to be stupid with them. - Ralph Waldo Emerson

Delft, The Netherlands D. Castelein
March 26, 2015

CONTENTS

NOMENCLATURE

Latin Symbols

a	Normal Induction Factor	$[-]$
a'	Tangential Induction Factor	$[-]$
c	Chord Length	$[m]$
C_D	Drag Coefficient	$[-]$
C_d	Drag Coefficient	$[-]$
C_N	Normal Force Coefficient	$[-]$
C_P	Power Coefficient	$[-]$
C_T	Tangential Force Coefficient	$[-]$
$C_{L_{max}}$	Maximum Lift Coefficient	$[-]$
C_L	Lift Coefficient	$[-]$
D	Diameter	$[m]$
f	Focal Length	$[mm]$
$f_\#$	F Stop	$[-]$
$N_{Samples}$	Number of Samples	$[-]$
p_∞	Static Pressure	$[Pa]$
R	Radius	$[m]$
R	Specific Gas Constant	$[\frac{J}{kg \cdot K}]$
Re	Reynolds Number	$[-]$
T	Temperature	$[K]$
u	Upwind Interference Factor	$[-]$
u'	Downwind Interference Factor	$[-]$
U_∞	Free Stream Velocity	$[\frac{m}{s}]$

V_u	Velocity at the Tunnel Exit	$[\frac{m}{s}]$
V_∞	The Free Stream Velocity	$[\frac{m}{s}]$
V_{eff}	The Effective Velocity acting on the Blade	$[\frac{m}{s}]$
V_{rot}	The Rotational Velocity	$[\frac{m}{s}]$
X_{True}	True Value	$[-]$

Greek Symbols

α	Angle of Attack	$[^\circ]$
α_{eff}	The effective Angle of Attack	$[^\circ]$
ϵ_t	Wind Tunnel Blockage Ratio	$[-]$
Γ	Circulation	$[\frac{m^2}{s}]$
λ	Tip Speed Ratio	$[-]$
μ	Dynamic Viscosity	$[\frac{kg}{s\dot{m}}]$
ν	Kinematic Viscosity	$[\frac{m^2}{s}]$
ω	Rotational Velocity	$[\frac{rad}{s}]$
ρ	Density	$[\frac{kg}{m^3}]$
σ	Standard Deviation	$[-]$
σ	The rotor solidity	$[-]$
θ	Azimuthal angle	$[^\circ]$

Abbreviations

$2C-PIV$	Two-Component standard Particle Image Velocimetry
AoA	Angle of Attack
BL	Beddoes-Leishman
CCD	Charge-coupled Device
DES	Detached Eddy Simulation
$DMST$	Double Multiple Stream Tube
DS	Dynamic Stall
FOV	Field of View
$HAWT$	Horizontal Axis Wind Turbine
OJF	The Open Jet Facility at TUDelft
PIV	Particle Image Velocimetry
Re	Reynolds
TSR	Tip Speed Ratio
$VAWT$	Vertical Axis Wind Turbine

CHAPTER 1

INTRODUCTION

Recent developments in the wind energy sector identify a potential cost reduction for offshore applications with VAWT. Compared to Horizontal Axis Wind Turbines (HAWT), VAWT possess higher potentials for scalability [31], a simpler design due to the absence of yaw or pitch mechanisms and a lower center of mass, since the generator is not constrained at the top of the tower (see Figure 1.1). It is believed that these advantages could lead to less maintenance and thus a lower cost. The prospect of the reduced costs and the possibility to displace the electric generator under water are of major interest in floating offshore applications [56]. Moreover some previous studies on VAWT hypothesised a faster wake recovery, leading to a reduction of the turbine spacing and more clustered arrays in a wind farm scenario [17].

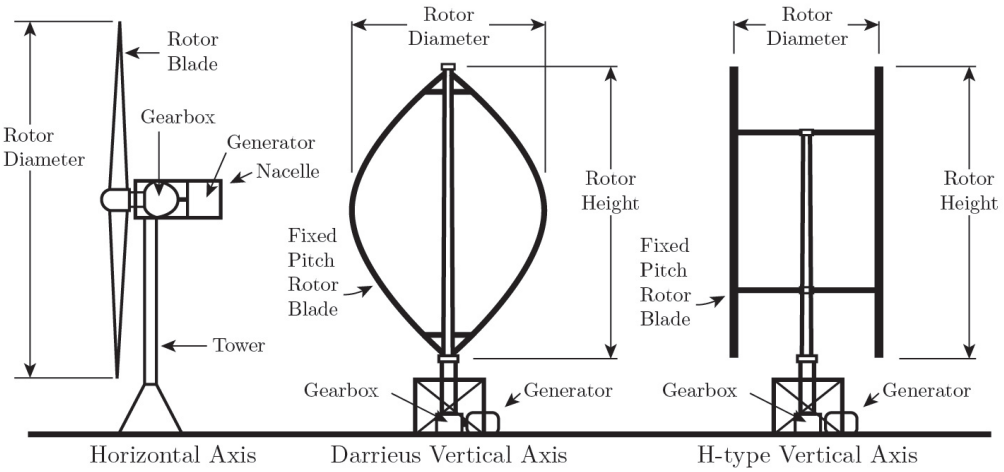

Figure 1.1: *Benefits of a VAWT.*

In order to supply the growing interest and questions of VAWTs, there is a need for more accurate numerical models. This can only be achieved by validating those numerical models on experimental data, and therefore many different experimental tests are required.

The emphasis of this experiment lies on dynamic stall, thus especially lower TSRs are investigated.

On the computational side, most of the numerical models in the industry are based upon actuator disk and stream tube models, which have been adapted from the HAWTs field. They are not entirely addressing the underlying physics of the VAWT. Although the role of the airfoil design has been found more relevant for the blade loading rather than for the energy conversion (Islam et al. [15], Claessens [6], Simão Ferreira [43]), the effects of the unsteady vorticity field generated by the blade cannot be neglected in the study of the evolution from the blade to the rotor wake. From the 3D point of view the wake of a VAWT has been characterised mainly from numerical analysis (Dixon [9], Simão Ferreira [43]), with models based on potential flow and vortex methods, though a continuous and extensive experimental activity is still missing. In the present thesis a detailed experimental investigation of the loads acting on an H-type VAWT (Figure 1.1) by the use of planar and stereoscopic particle image velocimetry (PIV) measurements is presented.

1.1 Research questions

Dynamic stall (on VAWT) creates large and sudden fluctuations in force, see Section 2.2.2. The DS phenomenon is numerically very hard to model, so a solid benchmark for a VAWT in DS is of great interest.

The research objective is to visualise the dynamic stall on VAWTs, and to compare different numerical models that predict this phenomenon. The research questions for this thesis are a threefold:

1. *Is it possible to capture the flow field around VAWT blades (in DS)?*
2. *What are the loads on VAWT blades, and what are they during DS?*
3. *How do numerical models predict these loads, compared to the experimental loads?*

The aim of this thesis is to present the experimental flow fields, and the validated loads on the blades for TSR 4.5 and 2. Later in this thesis, a benchmark for the loads on VAWT is created for (future) engineering models that predict these loads on VAWTs. The work is basically divided in four main tasks: 1) Conduct experiments on a VAWT with and without dynamic stall. 2) Visualise, by means of Particle Image Velocimetry (PIV), the velocity field around the blades. 3) Calculate the loads on the blades with the method proposed by Noca et al. [28] on these velocity fields are used to 4) Use the loads as a benchmark to determine the validity of the following numerical models:

1. *A Double Multiple Stream tube Model, with a Beddoes Leishmann DS model.*
2. *A 2D free Vortex Lifting Line Model, with an Øye DS model.*
3. *An inviscid Panel Model, without a DS model.*
4. *A Double Wake Panel Model.*

To accomplish these tasks, the work has been divided in three main phases. These phases are illustrated in Figure 1.2. All of the phases, are divided in sub-phases. The thesis is a series of successive steps as seen in the work breakdown structure in Figure 1.2. The first phase is the literature study. Here more information about what VAWT are, what DS is, how it affects the turbine, and how it can be modelled, is acquired. With this background, the experiment phase begins in phase two. In this phase the preparation for the experiment are done, the set-up is build in the wind tunnel, and the actual tests on the turbine are done. After the experimental phase is terminated, the processing of the PIV images can start. This is also the start of phase three: the programming phase. All the processed images of the PIV system are an input for the program that will calculate the loads. These can now be compared with the numerical models displayed in phase three. On the bottom of the figure, reporting is seen. The reporting is done throughout the entire thesis time.

1.2 State of the art

In this section an introduction in the previous experimental work done on VAWT, and on VAWT in dynamic stall is presented. Also in this section is an introduction about the origin and evolution of dynamic stall models. This gives also an overview of the different DS models that exist, and about the ones that are used.

1.2.1 Experimental work

Previous experimental work on the effect of DS on VAWT analysed the rotor from a performance point of view (see Laneville and Vittecoq [18]) or using flow visualisation techniques without quantification of the flow (see Brochier et al. [5]). Fujisawa and Shibuya [11] and Fujisawa and Takeuchi [12] developed a first attempt at flow field measurements of a Darrieus turbine using PIV at Reynolds numbers Re = 3000 and Re = 1000 (water flow).

In the last decade Paraschivoiu [29] compared experimental measurements of the averaged 2D induction field with prediction models (double multiple stream tube models). These models poorly estimated the energy recovery in the wake due to the way their downstream part of the rotor is modelled.

Simão Ferreira [46] visualised the flow around a VAWT by means of PIV. This was done for TSRs of 2, 3 and 4 with $Re = 5 \cdot 10^5$ & $7 \cdot 10^5$. This research focussed on visualising the vortex shedding and vortex roll-up due to DS. Therefore only flow fields from the upwind to the leeward positions of the turbine were presented. In this research there was no investigation of the loads acting on the blade.

Later research of Simão Ferreira [44] compared CFD simulations with the experiment conducted in previous mentioned research [46]. This was done in order to validate which model simulated the experiment best in terms of shed vorticity. This was found to be the DES (Detached Eddy Simulation) model. In this research, again no investigation of the loads on the blades were evaluated nor compared.

This thesis will present measured velocity fields at eight azimuthal positions for a VAWT at TSRs 4.5 and 2 . This thesis will also present the loads acting on the blade for those fields, calculated with the force calculation method by Noca et al.[28], as proposed by Simão et al. [45]. These velocity fields and loads will be made publicly available for future research on VAWTs and DS.

1.2.2 Dynamic stall models

In the early 1970', helicopter engineers found out that they failed to predict the performance of high-speed helicopters with their knowledge of the conventional aerodynamics. In 1973 Crimi and Yaggi [7] suggested that the forward flight was not limited due to aeroelastic behaviour, but due to the stalling and unstalling of the blades. Dynamic stall was identified, and during the rest of the 70's, a lot of research has been carried out. The first semi-empirical such as the UTRC methods, Boeing-Vertol model, and ONERA model were born in these times. The most famous model proposed by Beddoes and later refined by Leishman due to its extensive physical representation of the high speed unsteady phenomena that occur, was also developed during this research phase.

There are two different types of models that exist which can recreate dynamic stall. The first type are the empirical models. Which solve the Navier-Stokes or inviscid Euler equations. They are very computationally expensive, but give a very good insight of the physics of dynamic stall. The second type are the semi-empirical models by which the observed phenomena are modelled [29]. These models are much faster in calculations, but are less accurate. For reliable results, the semi-empirical model should be able to describe the phenomena, such as the delayed lift during attached flow, the delayed separation point during stall, the leading-edge separation, and the interaction of leading- and trailing-edge vortices. Also the model should be able to cope with a range of frequencies and amplitudes. The semi-empirical models can be sorted in three groups [19]:

1. The effects of the different flow conditions are modelled.
2. The characteristics of the lift curve are modelled.
3. The unsteady effects are captured in a dynamic angle of attack.

In the 1990's, dynamic stall models for wind turbine applications have been developed. Unstable atmosphere, yawed flow, sheared flow, skewed flow, rotational augmentation, and the active pitch control with rapid vibrations of the turbine, have pushed the wind energy industry in developing unsteady models for wind turbines. Most of those models are based on the work by Beddoes and Leishman, but mostly with a lot of simplifications for the typical wind turbine environment. Øye's model for instance discards all the unsteady effects except for the trailing edge separation delay. All in all, most models are derived from the Beddoes-Leishman model, and as such are of the first group of dynamic stall models. For that reason the Beddoes-Leishman model will be outlined including its mathematical description in Appendix B.

1.3 Thesis outline

This thesis is divided into six chapters. The first chapter is concluded with this section, and was an introduction to the thesis work. Chapter 2 is explaining all the theory used. This chapter will cover everything from the aerodynamics on the VAWT, to the numerical models used for comparisons in this thesis. This chapter will cover phase one shown in Figure 1.2.

In Chapter 3 the experimental set-up and the image processing is explained. This chapter is entirely dedicated to the experimental work conducted in this thesis, and covers phase two of Figure 1.2.

Phase three in Figure 1.2 is divided in two chapters. The entire method used in this thesis was first submitted to a sincere uncertainty analysis in Chapter 4. If the method has proven its reliability, the results are presented and discussed in Chapter 5.

Chapter 6 is the conclusion of the thesis work. In this chapter also some recommendations are made for future research.

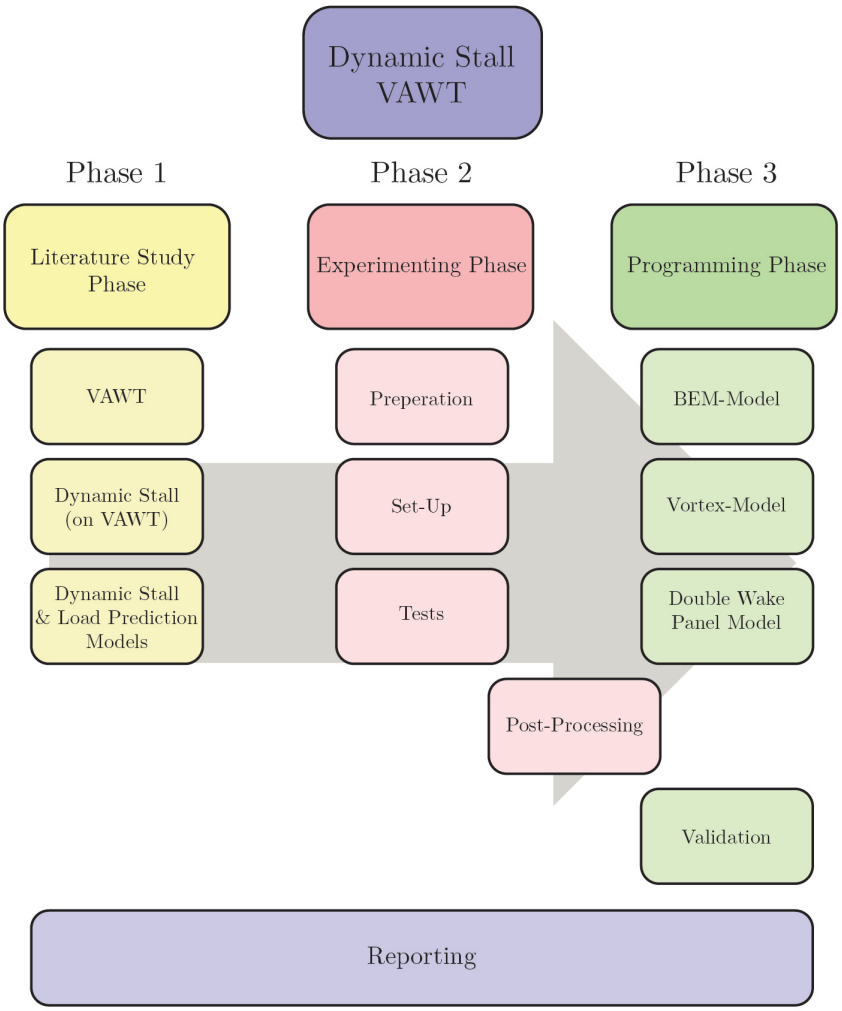

Figure 1.2: *The work breakdown structure.*

CHAPTER 2

THEORETICAL BACKGROUND

In this chapter, the work in this thesis that had to be done regarding phase 1 in Figure 1.2 is presented. This chapter will provide the background knowledge required to answer the research questions posed in this thesis.

First the unsteady aerodynamics that might occur on a VAWT are explained in Section 2.1. In this section the difference between static conducted test and dynamic tests, such as the one conducted in this research, is explained.

In Section 2.2 the stall phenomena that might occur during the experiment are elaborated. There are different ways an airfoil can get into stall. In this research the blade will be in dynamic stall during the TSR of 2. In order to understand dynamic stall, first static stall will be explained in Section 2.2, and afterwards the dynamic stall, together with the reasons why dynamic stall occurs on VAWTs.

When the theory about dynamic stall is explained, the PIV with all its components is explained in Section 2.3. This is necessary background information in order to conduct the experiment. From this experiment, the velocity fields can be used to calculate the loads with the load calculation method elaborated in Section 2.4.

If the loads acting on the turbine are known, they can be used to be compared to different numerical models. The theory behind these models can be read in Section 2.5, and the dynamic stall models that had to be implemented in some of the models can be seen in Section 2.6.

2.1 Unsteady wind turbine aerodynamics

Since the VAWT considered in this thesis work is mostly subjected to unsteady aerodynamics, an overview of the different unsteady aerodynamics is given in this section.

There are two groups that can be distinguished when considering unsteady aerodynamic effects on wind turbines, see Snel and Schepers [47]. The first one is the instationary profile aerodynamics, which are the aerodynamics considering the time dependent changing

sectional angle of attack. The second one is the dynamic inflow. This is the part that covers the influence of the shed and trailing wake vorticity on the inflow velocity of the rotor. Several phenomena can occur for both groups, and will be accounted for in this section.

2.1.1 Instationary profile aerodynamics

There are two unsteady effects that can be distinguished when considering instationary profile aerodynamics for regular wind turbines, as explained by Pereira, Schepers, and Pavel [32]. This is the Theodorsen effect, an effect of inviscous nature that delays the lift during attached flow, and the dynamic stall. The latter is a complex viscous effect, and will be elaborated more in Section 2.2. The last effect covered in this section is the blade-wake interaction, which is an effect that only occurs on VAWT.

Theodorsen effect

In Figure 2.1, side (A) left of the dotted line, the Theodorsen effect can be seen as it is described by Larsen, Nielsen, and Krenk [19]. They state that this Theodorsen effect will occur when rapidly changing the AoA during attached flow on the airfoil. Under these unsteady conditions it takes some time for the flow to reach the stationary flow pattern. The result is a delayed and thus lower lift for increasing angles of attack, and a higher lift the other way around in comparison with the steady case.

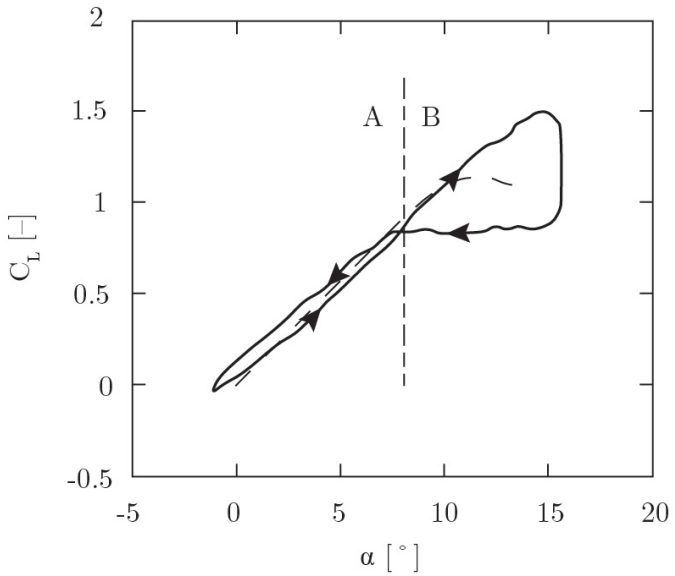

Figure 2.1: *Lift coefficient under static (- -) and dynamic (—) attached and stall situations [19].*

In order to understand the delay in lift, first a description of the two lift contributors proposed by Theodorsen [14, 51] has to be explained. The first lift contribution is the non-circulatory lift term. This lift term is caused by the airfoil accelerating the surrounding fluid. Therefore, this part is linked closely to the acceleration of the airfoil, and there

is no delay or lag involved. Second is the lift originating from the bound circulation on the airfoil. When changing the AoA, the circulatory lift term will inevitably change. According to Kelvin's theorem, a counter rotating vortex of equal strength formed at the trailing edge is shed into the wake. This shed vorticity will counteract the lift force on the airfoil. Since it is time dependent, there will be a delay in lift for a short time. For this theory to be valid, Theodorsen assumed attached flow, a flat plate airfoil assumption, and a straight wake. Hence, the case of delayed lift under attached conditions is known as the Theodorsen effect.

Dynamic stall

In contrary to the Theodorsen effect that is occurring under attached flow conditions, dynamic stall is occurring on airfoils in detached flow conditions, i.e. when the static stall angle is exceeded [α_{max}]. In Figure 2.1 the dynamic stall effect can be seen at side (B), right of the dotted line. It can be observed that the motion of the lift is now in opposite direction of the Theodorsen effect (lift is higher for increasing AoA, lower for decreasing AoA). This is caused due to the delay in lift when pitching over the α_{max}. The dynamic stall effect will delay the stall angle, and higher lift forces can be observed due to this phenomenon. Since the complexity of dynamic stall, a more elaborated explanation of the dynamic stall phenomenon is given in Section 2.2.

Blade-wake interaction

VAWT machines are the only turbines that have the ability to have a blade-wake interaction. This is due to the interaction of the blade downstream with the wake which was shed upstream. This unsteady phenomenon will have consequences on the force production of this blade. When increasing the number of blades, the tip speed ratio or the blade loading, the effect of this phenomenon will become more pronounced. Research by Ferreira [43] indicates that due to blade-wake interactions, the blades downstream could locally even reenergise the flow. Thereby even becoming a propulsion system. This makes this phenomenon, thereby an interesting and important unsteadiness for VAWT operations.

2.1.2 Dynamic inflow

The inviscid natured dynamic inflow phenomenon is caused by the time-varying trailing wake shedding [47] and will act as an unsteady rotor inflow velocity. The time scale at which this phenomenon occurs ($\frac{D}{U_\infty}$) is said to be about one or two orders higher than for the instationary profile aerodynamics($\frac{c}{V_{eff}}$), and that when unsteady effects would have a higher order timescale, they are treated as quasi-steady. As dynamic inflow is caused by fluctuating wake shedding, the origin lies in the time dependent inflow angle on the blade. Reasons include the unsteady wind profile itself (wind gusts), blade pitching, or 1P phenomena (for instance yawed flow).

2.2 Dynamic stall

In order to get a more elaborated view on dynamic stall, as it was introduced in Section 2.1, an introduction of static stall will be given first in Section 2.2.1. Understanding the theory behind dynamic stall is key in order to understand the complexity of this thesis work. A lot of numerical models are not able to simulate the dynamic stall phenomenon. To compensate, there are some dynamic stall models that can be implemented into these models.

2.2.1 Static stall

A short introduction for static stall is given according to Crimi and Yaggi [7]. The static stall phenomenon can be divided three forms of stall: trailing edge stall, leading edge stall and thin airfoil stall. A combination of leading and trailing edge stall is also possible. Figures 2.2-2.4 show the flow over an airfoil in different conditions.

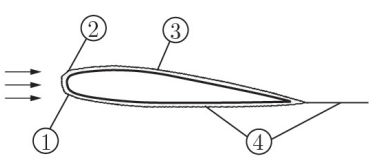

Figure 2.2: *Attached flow [7].*

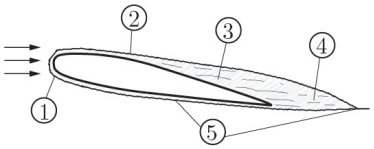

Figure 2.3: *Leading-edge stall [7].*

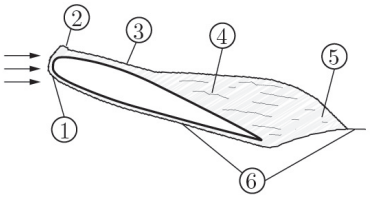

Figure 2.4: *Trailing-edge stall [7].*

In Figure 2.2 the flow is entirely attached to the airfoil and no separation takes place. There is only a small laminar separation bubble near the leading edge that can form at a fairly low incidence angle (2). However, this bubble is of such small dimensions, it has a negligible effect on the pressure distribution. At the transition point (3) the boundary layer will transition to turbulent, but will re-attach to the airfoil due to an increase in energy. As explained before, a vortical wake (4) will be formed due to the time dependent changes in circulation on the airfoil. The flow outside the boundary condition is considered to be potential flow.

A phenomenon that can happen when the AoA would be increased, is that the leading edge bubble would move towards the leading edge, and would grow in size until it eventually bursts. This is called leading-edge stall, seen in Figure 2.3, and results in full separation and a sudden loss of lift, also seen in Figure 2.5 at leading edge stall. From the point of separation the flow is now governed by a laminar shear layer up till the point of transition (3) after which the shear layer becomes turbulent. Finally a turbulent pressure recovery region (4), a vortical wake (5), and potential flow outside the boundary and shear layer are apparent.

The trailing edge stall (Figure 2.4) is the most common stall, and is a combination of the previously mentioned attached flow, and the leading-edge stall mechanism. In the laminar state, the boundary layer could have a laminar separation bubble. At the transition point (2) the boundary layer will become turbulent, and in case of a bubble, the flow will re-attach. At the given moment (3) the turbulent boundary layer will separate from the

airfoil. This will form a turbulent shear layer (4), where outside this layer, the flow is considered potential again. Point (5) shows the pressure recovery region, and point (6) shows the vortical wake being formed. As can be seen in Figure 2.5 the forces will drop smoothly with trailing edge stall.

The last form of stall, the thin-airfoil stall, is not shown in Figures 2.2-2.4. The occurrence of this stall is characterised by a laminar separation bubble bursting at very low AoA. As for the leading edge stall, this bubble will not move forward before bursting, but will grow progressively bigger before separation occurs. This can only occur on thin airfoils. In Figure 2.5 the thin-airfoil stall is also displayed, where it can be seen that the slope of the lift is less steep, and the separation occurs earlier than in a laminar boundary state.

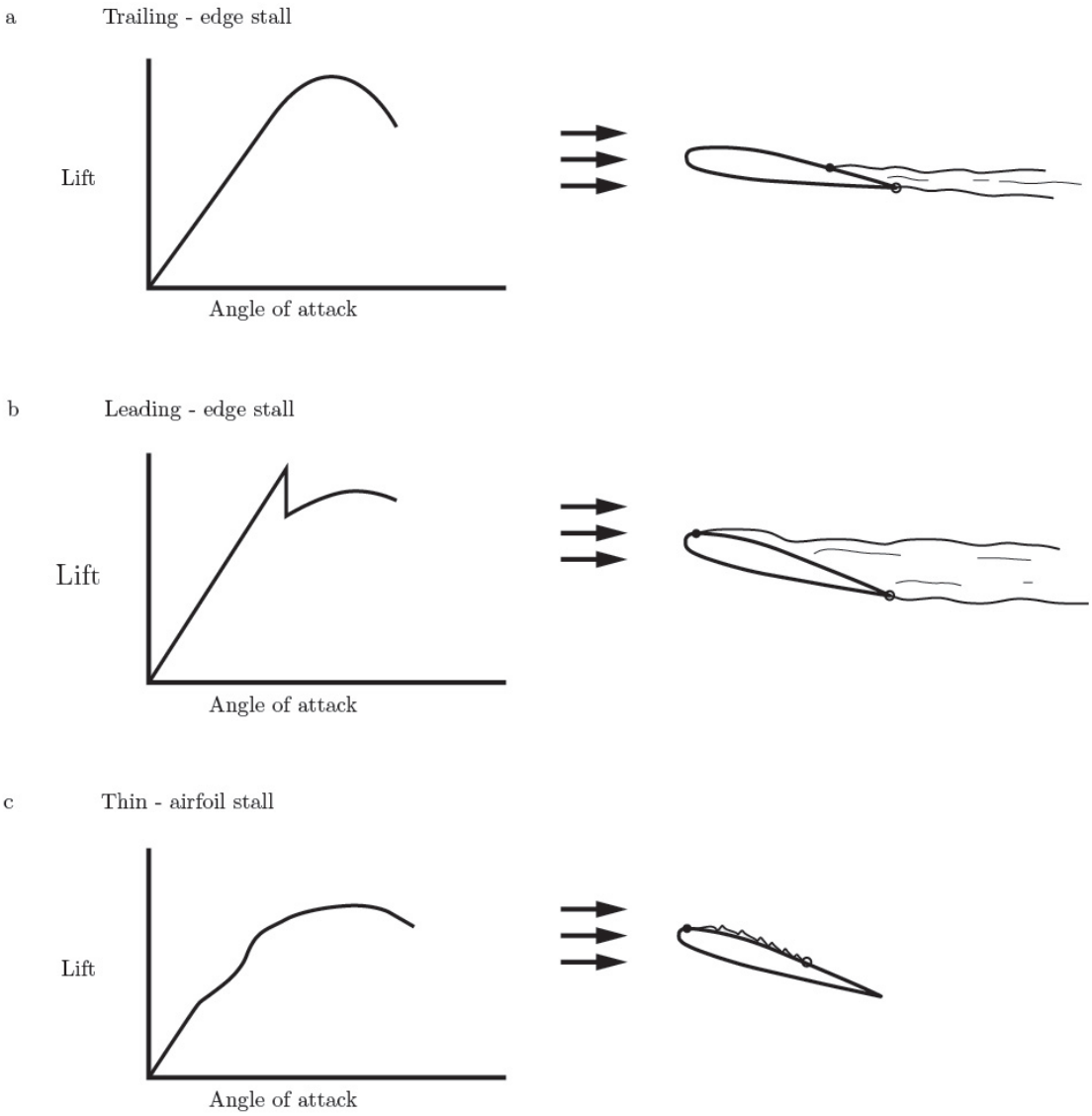

Figure 2.5: *Three types of airfoil stall [7].*

2.2.2 Dynamic stall

The dynamic stall phenomenon will occur on airfoils that are subjected to unsteady conditions. During a cyclic motion of the AoA, and during this motion the critical AoA [α_{Stall}] is exceeded. Due to the VAWT characteristics, it is common for airfoils to be in dynamic stall, definitely at low TSR, more elaborated in Section 2.2.3.

According to Larsen et al. [19] for the phenomenon of dynamic stall to occur, a leading-edge separation bubble needs to develop. In the quasi-static case two types of flow separation can occur at the same time which will also result in two different lift curves. One is that the boundary layer will reattach due to the turbulent layer behind the bubble. Second is the boundary layer will separate at the bubble and over the complete suction side. This is what is called double stall.

Under dynamic conditions, full boundary separation can occur. At the leading-edge a vortex will start growing linearly with increasing AoA, which will create a big suction peak. Due to this peak, the lift will keep on increasing. At some point, the vortex will detach from the leading edge, and will start travelling downstream over the airfoil with a speed of approximately $\frac{1}{3}U_{\infty}$. While travelling down, the lift is still growing due to the vortex. When the trailing edge is reached, a trailing edge vortex with opposite circulation will start growing, which will counteract the strength of the original vortex. During the decreasing AoAs the flow will re-attach again from the leading edge. While lowering the AoAs even more, the separation point will gradually move backwards, until the full airfoil is in attached flow again. During this process of re-attachment, the lift produced by the airfoil will be much lower than in the static case for the same AoAs.

In Figure 2.6 the lift, drag and moment curve of an airfoil in dynamic stall is presented. This figure presents a good overview of the unsteady aerodynamics that were discussed above. Between point 1 and 2 the flow is attached on the airfoil. The lift exceeds the static polar, but yet no big increase in neither the drag nor moment curve can be seen. The leading edge vortex appears at point 2, and grows until point 3. This vortex keeps adding a linear lift behaviour, but also induced a larger drag and moment on the airfoil. At point 3 the vortex will detach and travel downstream. The lift will still be increasing linearly due to the big suction of the vortex, whereas the drag and moment curves show big changes at this point. Due to the vortex moving along the airfoil (with its big suction peak) the moment curve drops drastically, and the drag coefficient will increase drastically. At point 4 the leading edge vortex is at the trailing edge, and the lift drops, whereas the moment coefficient rises a little again, and the drag drops a little. At point 5 the trailing edge vortex creation can be seen, where the lift will increase a little again, where the moment coefficient drops again, and the drag rises. The leading edge re-attachment occurs at point 6.

According to McCroskey [23], there are a few things that affect dynamic stall. On thin airfoils and airfoils with a relatively sharp leading edge, leading edge stall is more likely. This can lead to a sudden separation and a leading-edge vortex creation, which will eventually lead to the changes in lift, drag and moment, as shown in Figure 2.6. On thicker airfoils, it is more likely that trailing-edge stall occurs. Here the separation point will increase more gradually to the leading edge, and less abrupt changes in force will occur. It is shown that unsteady effects will suppress the separation more than for thin airfoils, and negative aerodynamic damping is less likely. The airfoil will play an important

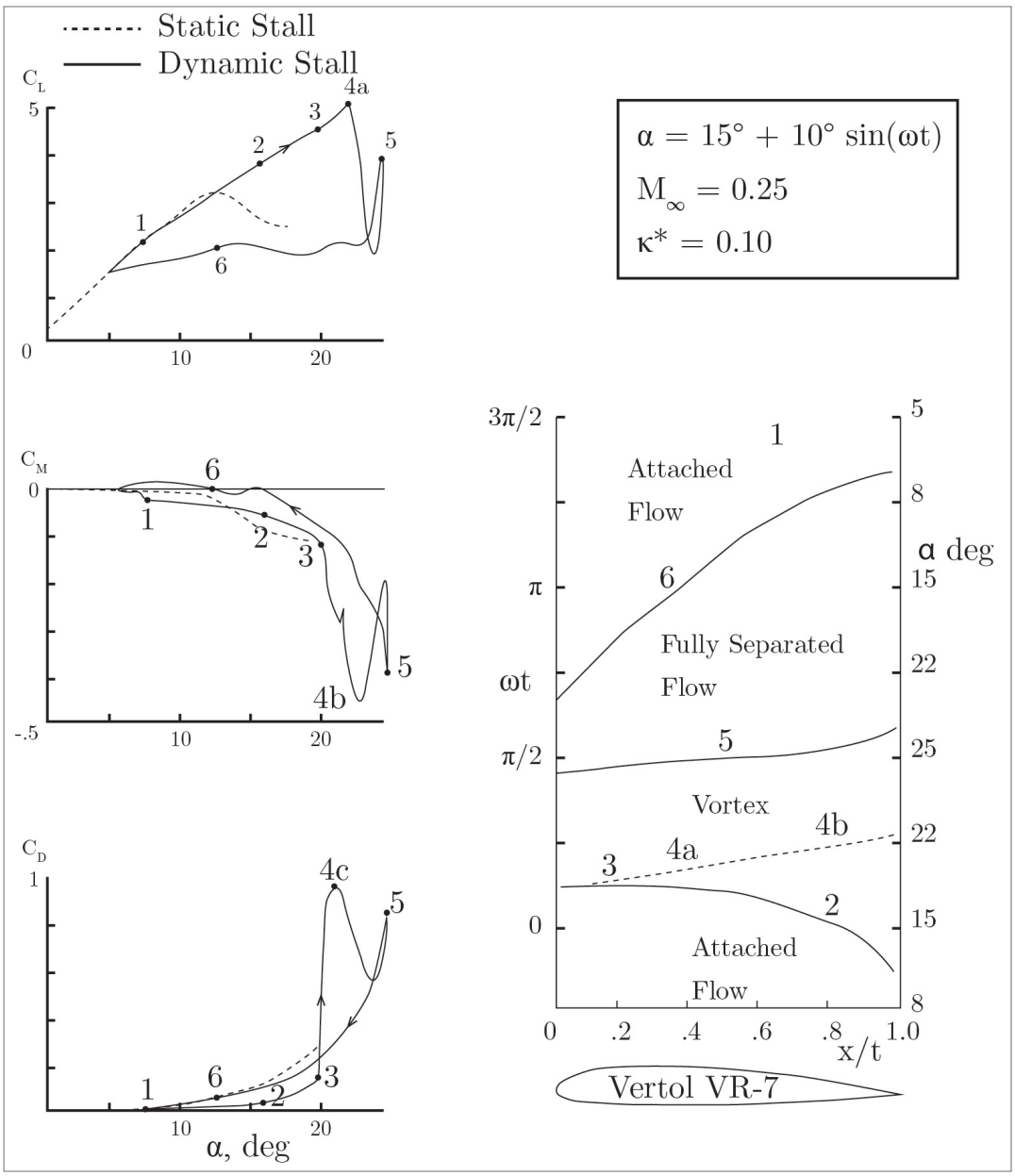

Figure 2.6: *Lift, moment, and drag coefficients under static (- -) and dynamic (—) stall [23, 29].*

role when designing a turbine [42]. The Mach number is also interesting to look at. Shock waves can occur near, or on the leading edge, which can cause the flow to separate. Although in the wind turbine industry, where airfoils are not exceeding a Mach larger than 0.2, the effects concerning this will be small. The most important parameters are the reduced frequency (defined as $k \equiv \omega c/2V$), and the mean angle and amplitude of the oscillation. It is also shown that the influence of the Reynolds number is small for at least low Mach numbers.

Pereira et al. [32] show an overview of the importance of reduced frequency on the unsteady process. They stated that the problem can be assumed quasi-steady for $k < 0.05$, where the unsteady effects are small and can be neglected. For a higher reduced frequency, the flow is assumed unsteady. For $k > 0.2$, the unsteady influences begin to dominate the flow behaviour. It has to be noted that for horizontal axis wind turbine applications, it is generally assumed that $k > 0.02$ already results in unsteady flow.

2.2.3 Dynamic stall on vertical axis wind turbines.

Due to the a VAWT configuration, dynamic stall occurs frequently on these turbines. This due to several reasons: the cyclic variation of AoA over each rotation, the flow curvature the turbines blades are subjected to and the operational TSR are important aspects in knowing the (stall) conditions of the turbine. All these aspects will be explained separately in this section.

Cyclic angle of attack

The AoA is determined by the rotational speed (V_{rot},ωR), the free stream velocity (V_∞), and the loading of the turbine; resulting in an induced flow component (induction factors) [a, a'], mainly opposite to V_∞ (in Figure 2.7 the induction [$V_\infty(1-a)$] is already compensated for). In this figure it can be seen that the azimuthal position, due to the direction of the free stream velocity and the rotational velocity at this position, has a big influence on the AoA of the turbine. Figure 2.8 shows the variation of AoA at azimuthal positions varying from 0 to 360°. This plot was made for a turbine with TSR of 4.5 [42].

As explained in Section 2.2.2, cyclic AoAs cause dynamic stall. In Figure 2.8 can be seen that there are large AoA variations in the cycle of the VAWT. Especially the regions between 0-180 [°] there is a big AoA variation that stimulates the occurrence of dynamic stall.

Flow curvature

Shown in Figure 2.9 is an airfoil subjected to a curved flow. Due to the circular motion of a VAWT blade, it will always be subjected to a curved flow, and this will have to be taken into account.

Blade properties (C_l, C_d) are measured in wind tunnels in a laminar, straight flow. Compensation for the flow curvature effect can be done by either adding an artificial camber in the airfoil (bottom airfoil, Figure 2.9.) or by adding an artificial AoA, or both [24]. As the radius of the VAWT becomes larger, the effect of flow curvature minimises.

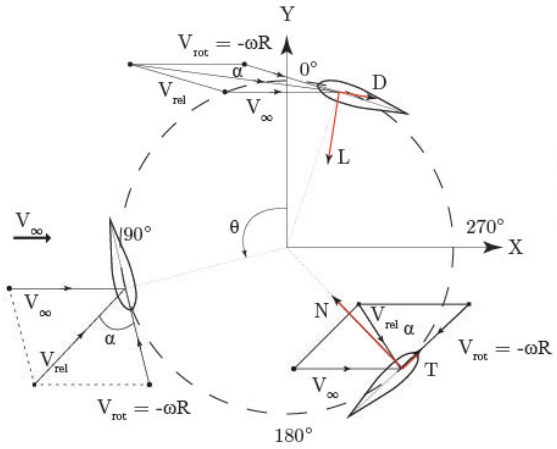

Figure 2.7: *The forces and velocities acting on a VAWT.*

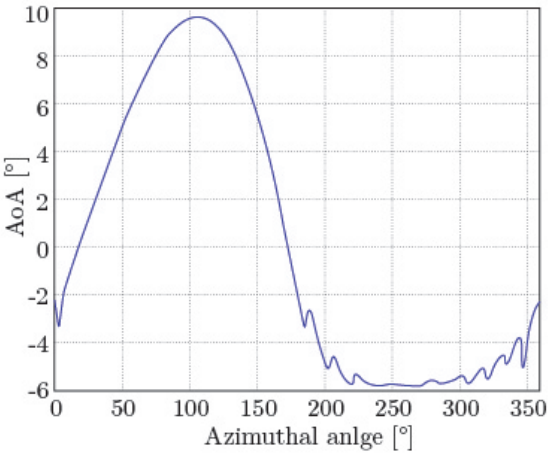

Figure 2.8: *The AoA for an entire rotation at TSR = 4.5 [-] [42].*

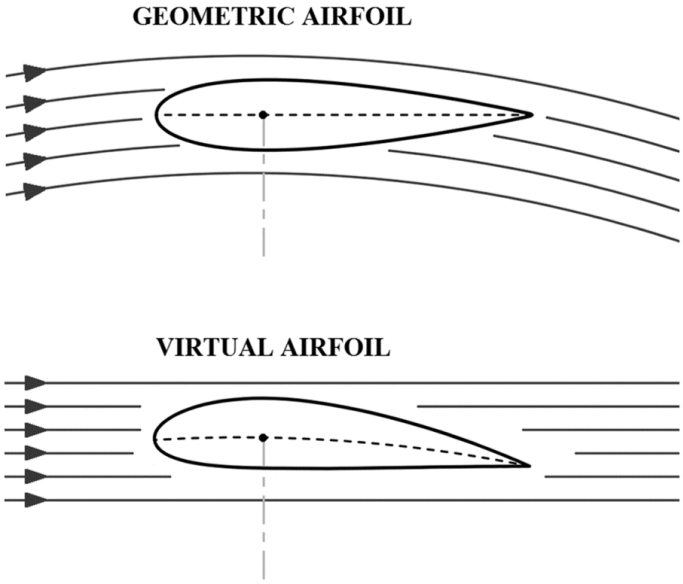

Figure 2.9: *The effect of the curved flow [24].*

Tip speed ratio

The operation condition of the machine is represented by the Tip Speed Ratio (TSR, λ), shown in Equation 2.1. When the turbine is operating at lower TSRs, the variation in AoA is higher. In Figure 2.10 the cyclic variation of the AoA can be seen for different TSR. Turbines operating at a TSR lower than 5 typically have an AoA exceeding the critical AoA, and the occurrence of dynamic stall is possible.

$$\lambda = \frac{\omega R}{V_\infty} \tag{2.1}$$

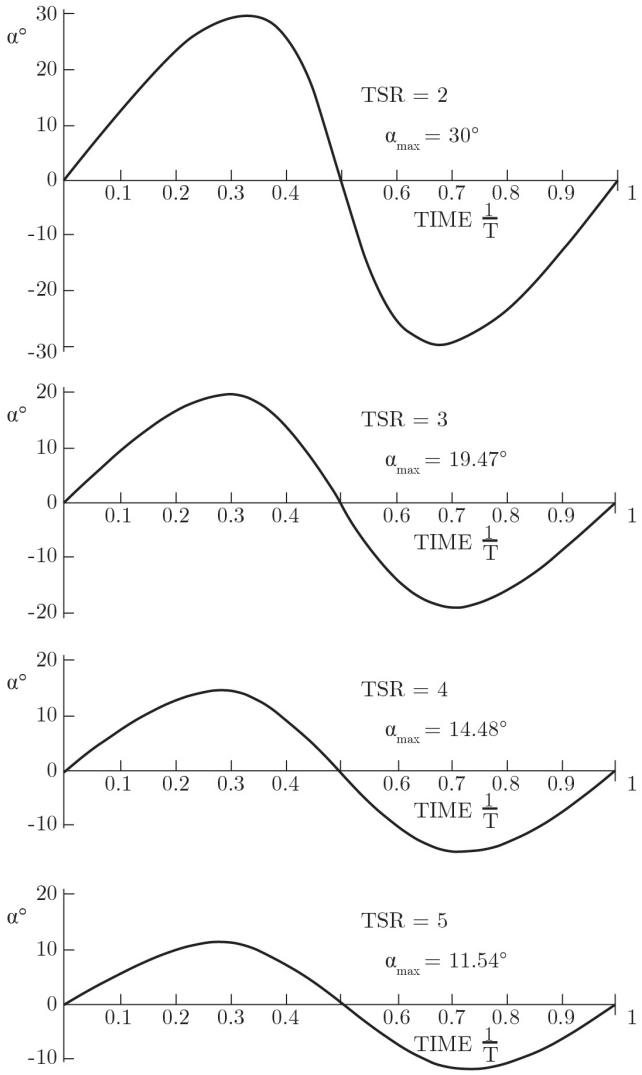

Figure 2.10: *The influence of the TSR on the max AoA [α_{max}] [57].*

2.3 Particle image velocimetry

The method used to capture the velocity fields around the blade will be Particle Image Velocimetry (PIV).

PIV is a non-intrusive flow diagnostic technique allowing flow field measurements. Comparing with intrusive flow measurement techniques like hot wire anemometer or pressure tube, PIV eliminates the need of instrumental intrusions by using non-intrusive laser light and tracer particles. It captures large fields with even small fluctuations in a short time [33]. PIV is the perfect tool in the design of a dynamic stall experiment on VAWTs.

Due to fast developments and research with this technique, of-the-shelf programs have become reliable and ready for use. LaVision® is one of the main companies developing PIV systems. The four main components of a PIV system are discussed in this section. The

PIV instrumentation consists of the seeding device, the laser to illuminate the particles, the camera to capture the illuminated particle and the software to process the data.

2.3.1 Seeding generator

Since the flow through the open jet wind tunnel will be transparent, seeding is needed to visualise the flow. For this purpose a simple fog generator is sufficient, in this case the *Safex Fog Generator* shown in Figure 2.11. The fog is non-toxic and based on water-glycol. The mean particle diameter is $1[\mu m]$ as can be seen in Figure 2.12. Due to the small diameter, these particles follow the flow excellently. It is also recommended as a visualiser for PIV [33].

Figure 2.11: *The safex fog generator [8].*

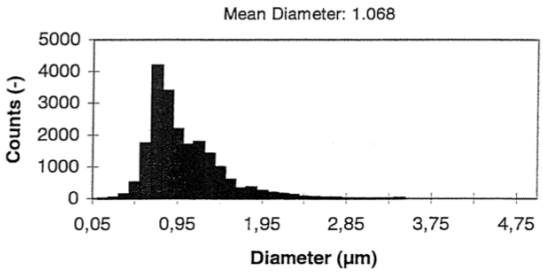

Figure 2.12: *Particle diameter.*

2.3.2 Laser

The laser is needed in PIV experiments in order to illuminate the particles generated by the seeding device. In this practical a *Quantel Evergreen* laser is used, which is double pulsed with two cavities producing infrared light. In the laboratory the light was clearly green, this is due to the fact that the light is made visible with a second harmonic generator. Although the laser beam is filtered the intensity is so high that it is highly hazardous for the eye, so safety goggles are always worn. The energy pulse is controlled through the software *Davis*, and has a pulse duration of $8[ns]$ and a repetition rate of $30[Hz]$. Finally all the information is sent to the digital delay control unit, which controls the triggering signals for both the laser and the camera.

2.3.3 Charge-coupled device camera

The illuminated particles are captured by a *LaVision Imager Intense* CCD camera, which consists of 4870x3246 pixel with $7.4[\mu m]$ pixel pitch, can record 12-bit black and white images and has a recording rate of $5[Hz]$. Thus only one of the three laser pulses can be used. The first exposure, frame A, has a duration of $10[\mu m]$, while the second, frame B, has a longer exposure, $100[ms]$, and therefore captures more ambient light causing less accurate recordings. A daylight filter is mounted on the lens, which only transmits light in a narrow band around the laser wavelength. This largely reduces the effect of background light due to ambient light. The recordings from the camera are received by the control box. Finally, for the capturing the particles a *Nikon* $f = 105[mm]$ lens is used and the $f_{\#}$ can be set from 2.8 to 32.

Figure 2.13: *LaVision imager intense CCD Camera [20].*

2.3.4 PIV software

The *Davis* software uses the cross-correlation principle to process the data. This algorithm sets an initial guess of the particle displacement from the window of image A and B, and with an iterative procedure determines the actual displacement. This process decreases the interrogation window and deforms the correlation window after the first iteration in order to account for the local deformation of the tracer particle pattern. It outputs all the velocities from all the final interrogation windows, these can be used for further investigation.

2.4 Load calculation method

From the PIV measurements, the velocity fields around the blades of the VAWT are gathered. From the resulting velocity fields different methods are used to compute, by integration, the loads acting on the blade. The methods rely on the direct use of the velocity in an unsteady Bernoulli equation [55] or by the use of the vorticity [54], explained in Section 2.4.1. By integrating these quantities along a contour around the blade the forces can be derived with the load calculation method proposed by Noca et al. [28], elaborated in Section 2.4.2.

2.4.1 The Bernoulli approach

The force per unit unit density can be calculated with Equation 2.2. The representation of this equation is shown in Figure 2.14.

$$\frac{F}{\rho} = \overbrace{-\frac{\mathrm{d}}{\mathrm{d}t}\int_{V_{(t)}} u\mathrm{d}V}^{Acceleration\ Term} \overbrace{+\oint_{S_{(t)}} \hat{n}.\left[-\frac{p}{\rho}\vec{I} - (u-u_S)u + T\right]\mathrm{d}S}^{Pressure\ Term} \overbrace{-\oint_{S_{b(t)}} \hat{n}.\left[(u-u_S)u\right]\mathrm{d}S}^{=0} \tag{2.2}$$

Where T is the viscous stress tensor (Equation 2.3).

$$T = \mu(\nabla u + \nabla u^T) \tag{2.3}$$

In Equation 2.2 two terms will pose problems: one being the velocity integral over the entire integration area ($\mathrm{d}V$) in the acceleration term, and the other the pressure term (p). The integration over the entire field can be made impossible due to shadow effects or reflections. The pressure terms are unknown, and will have to be derived. By deriving those pressures, more errors will occur in the results. Adding more errors to the load calculations was not an option, so this method is disregarded.

2.4.2 Load calculation method by Noca et al.

Another method, proposed by Noca et al. [28], is used to calculate the loads on the blades, as proposed by Simão et al. [45].

The Noca et al. method uses a Flux Equation formulation seen in Equation 2.4 [27]. The representation of this equation is shown in Figure 2.15.

$$\begin{aligned}\frac{F}{\rho} =& \overbrace{+\oint_{S_{(t)}} \hat{n} \cdot \gamma_{flux} \mathrm{d}S}^{Flux\ Term} \\ & \overbrace{-\oint_{S_{(t)}} \hat{n} \cdot [(u - u_S)u]\,\mathrm{d}S}^{=0} \\ & \overbrace{-\frac{\mathrm{d}}{\mathrm{d}t}\oint_{S_{b(t)}} \hat{n} \cdot (ux)\mathrm{d}S}^{Movement\ Term}\end{aligned} \tag{2.4}$$

With in the flux term (γ_{flux}), shown in Equation 2.5 [27].

$$\begin{aligned}\gamma_{flux} =& \frac{1}{2}u^2\vec{I} - uu - \frac{1}{N-1}u(x \times \Omega) + \frac{1}{N-1}\Omega(x \times u) \\ & - \frac{1}{N-1}\left[(x \cdot \frac{\partial u}{\partial t})\vec{I} - x\frac{\partial u}{\partial t} + (N-1)\frac{\partial u}{\partial t}x\right] \\ & + \frac{1}{N-1}\left[(x \cdot (\nabla \cdot T)\vec{I} - x(\nabla \cdot T)\right] + T\end{aligned} \tag{2.5}$$

As can be seen in Equation 2.4 & 2.5, the pressure term as seen in Equation 2.2 has vanished due to the use of the flux term. The flux term uses vorticity in stead of pressure. Since the vorticity can be directly calculated from the velocity field, less errors will occur with this method. The area integral has also vanished. Only a contour integral for all terms is needed. This makes much more sense when integration over masked regions in term of interpolation. The inputs this model needs are:

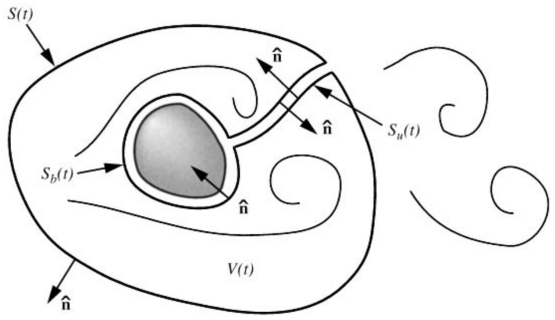

Figure 2.14: *Control volume analysis [28].*

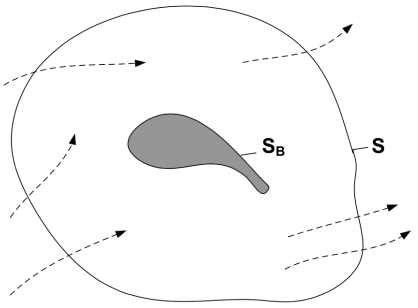

Figure 2.15: *Representation of the control volume bounded by the outer contour S and the body contour S_B [43].*

- Coordinates ($[X, Y]$)
- Velocity vector ($[U, V]$)
- The flow acceleration ($[\frac{\partial U}{\partial t}, \frac{\partial V}{\partial t}]$)
- Density (ρ), viscosity (μ)

All the inputs, except for the acceleration terms ($\frac{\partial U}{\partial t}\frac{\partial V}{\partial t}$), came directly from the experiment post-processing. For the acceleration term, for every azimuthal position (θ) seen in Table 3.2 also the angles $\theta^{\circ}_{T\pm1}$ are taken. The acceleration terms are computed with Equation 2.6.

$$\begin{aligned} \frac{\partial U}{\partial t} &= \frac{(U_{\theta_{T+1}} - U_{\theta_{T-1}})}{2 \cdot \mathrm{d}t} \\ \frac{\partial V}{\partial t} &= \frac{(V_{\theta_{T+1}} - V_{\theta_{T-1}})}{2 \cdot \mathrm{d}t} \end{aligned} \tag{2.6}$$

With dt being the time it takes the blade to travel approximately 1°. More about this in Section 4.3.

Since more positions have been used to calculate this acceleration term, more masked regions with lost velocity components will exist. to minimise the error, it was opted to remove all the regions from the corresponding fields from all three azimuthal angles when calculating the acceleration terms to derive the force.

The second term will be zero in this case, since there is no suction or blowing applied to this experiment. The flux term however, has to be calculated along contours, see Chapter 5. The flux term will have the biggest impact in terms of magnitude of force. The movement term will be added to this term. The movement term is the force due to the rotational velocity of the blade. This force will be the same at every θ, in the assumption the rotational velocity is constant. This term can be calculated using Equation 2.7. These

two term together will give the total load acting on the blade.

$$\begin{aligned}\frac{\mathrm{d}}{\mathrm{d}t}\oint_{S_{b(t)}} \hat{n}\cdot(ux)\mathrm{d}S &= \begin{bmatrix} n_1 & n_2 \end{bmatrix}\begin{bmatrix} U_x & U_y \\ V_x & V_y \end{bmatrix} \\ &= \begin{bmatrix} n_1\cdot U_x + n_2\cdot V_x & n_1\cdot U_y + n_2\cdot V_y \end{bmatrix}\end{aligned} \tag{2.7}$$

The results for both tip speed ratios are given in non-dimensional velocity in Table 2.1.

Table 2.1: *Results from the movement term for both TSR cases.*

	Normal Force [-]	**Tangential Force [-]**
TSR 4.5	0.0351	0.0123
TSR 2	0.0123	0.0024

2.5 Numerical models

The loads can now be extracted from the experiment. These loads will be compared to different numerical models. In order to do so, the models will be elaborated in this section.

In Table 2.2 the different numerical models, with their capability to model DS by itself, or the DS model that is added so it will be able to model DS, can be seen. In this table the developers of the models are stated. These models were not built by the author of this thesis, only used to compare the results.

As is seen in Table 2.2, only one model is capable of predicting the loads on the blade in DS without any DS model addition: The double wake panel model. It is assumed that these will predict the loads relatively well compared to the other models. All the other models have an extension for the prediction of DS, except for one: the inviscid panel model. This model will not be compared in the TSR 2 case because of it's inviscid nature. The BEM model used, is the Nenuphar [26] model, which is used to build large (6MW) offshore VAWT, and has a Beddoes-Leishmann DS model built in to it. It is expected that this model will be able to predict the DS load relatively well in the upwind region. The lifting line is the model used by Berdowski as demonstrator for his final thesis work [4]. He developed this code with an Øye DS model, and compared his values to the experimental work done by Paraschivoiu [29]. In this thesis his model will be validated again with the experimental data gathered from this experiment. In section 2.6, the DS models that are used are more elaborated.

2.5.1 Double actuator, multiple stream tube model

One of the most popular methods to model the VAWT is the double (actuator) multiple stream tube model (DMST model), developed by Strickland [49]. An extensive explanation of the model is given by Paraschivoiu [30], and his way of notation will be used throughout this section.

Table 2.2: *Numerical models and their DS modelling capabilities.*

Numerical Model	Can model DS	DS model	Developed by
BEM model	NO	Beddoes Leishmann	Nenuphar [26]
Lifting Line Model	NO	Øye	T. Berdownski [4]
Inviscid Panel Model	NO	none	C.J. Simão Ferreira [43]
Double Wake Panel Model	YES	not needed	A. Zanon [58]

The DMST is a momentum method based on the actuator disk theory from Glauert [13], where the induced velocities are computed with the balance of momentum in the flow. An important aspect in the stream tube model is that the downwind rotor is producing in the wake of the upwind rotor. Therefor both actuator disks are operating with different free stream and induced velocities. Furthermore, the flow in the VAWT is modelled as a series of separate stream tubes. This will compensate for the alternating thrust the blades apply on the flow over the rotation, due to the operation nature of a VAWT. Finally 3D phenomena and the wake expansion could be modelled, but those are left out of the current analysis.

Model description

The definitions for this model are presented in Figure 2.16. The velocities are given in the free stream, the upwind and downwind actuator disk, and in the equilibrium position. In Equations 2.8 to 2.11 it can be seen how these velocities are calculated. u and u' are the upwind and downwind interference factors.

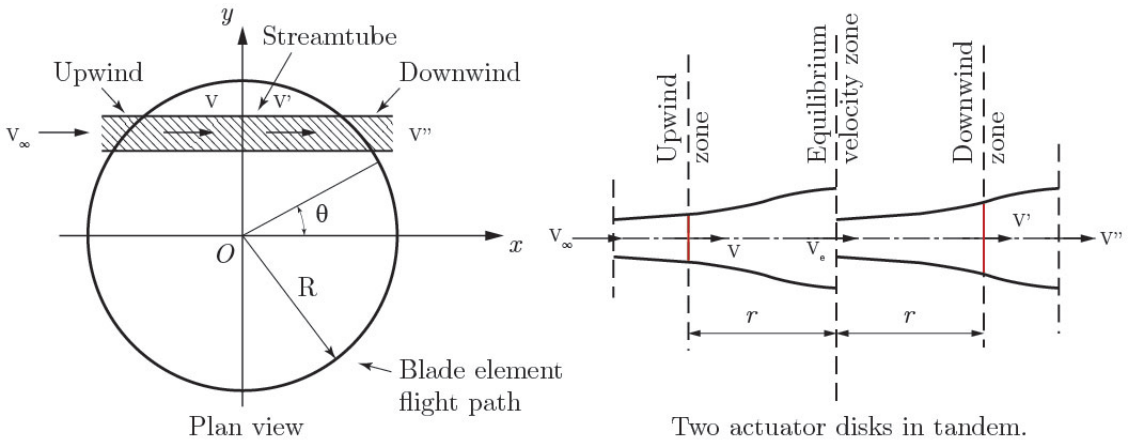

Figure 2.16: *The definitions used in the multiple streamtube model [30].*

$$V = uV_\infty \tag{2.8}$$

$$V_e = (2u - 1)V_\infty \tag{2.9}$$

$$V' = u'V_e = u'(2u-1)V_\infty \tag{2.10}$$

$$V'' = (2u-1)(2u'-1)V_\infty \tag{2.11}$$

The relative velocity (V_{rel}) and the local AoA (α) on the blade of a H-type VAWT, can be calculated with Equation 2.12 and 2.13 accordingly. In these equations only the upwind calculations are shown. The downwind calculations can be obtained by substituting the downwind values denoted with an accent ($'$).

$$V_{rel}^2 = V^2[(\lambda - \sin\theta)^2 + \cos^2\theta] \tag{2.12}$$

$$\alpha = \sin^{-1}\left[\frac{\cos\theta}{\sqrt{(\lambda-\sin\theta)^2+\cos^2\theta}}\right] \tag{2.13}$$

In order to calculate the normal and tangential force, the local Reynolds number has to be calculated. This is done with Equation 2.14. With the reynolds number given, the lift and drag polars can be acquired. The resulting normal and tangential force are calculated with Equation 2.15 and 2.16 accordingly.

$$\mathrm{Re}_b = \frac{V_{rel}c}{\nu_\infty} \tag{2.14}$$

$$C_N = C_L\cos\alpha + C_D\sin\alpha \tag{2.15}$$

$$C_T = C_L\cos\alpha - C_D\sin\alpha \tag{2.16}$$

The blade force coefficients can be used to calculate the induced velocities. The relationship for the induced velocities, when having multiple stream tubes, is given in equation 2.17. f is a function that characterises the flow and is described by equation 2.18. The geometric parameters are $K = 8\pi R/Nc$, and $K_0 = \sin(\theta + \Delta\theta/2) - \sin(\theta - \Delta\theta/2)$.

$$u(\theta) = KK_0 \Bigg/ \left[KK_0 + \int_{\theta-\Delta\theta/2}^{\theta+\Delta\theta/2} f(\theta)\mathrm{d}\theta\right] \tag{2.17}$$

$$f(\theta) = \left(\frac{V_{rel}}{V}\right)^2 [C_N\cos\theta + C_T\sin\theta] \tag{2.18}$$

As the angle of attack and the induced velocities are interdependent, an iteration over the above described algorithm should lead to a convergence of the solution. The power capabilities are finally calculated by averaging the torque over the rotor and multiplying

the outcome by the overall tip speed ratio $\lambda_e q$ (which can be described by equation 2.1, by substituting V_∞). This is shown in equation 2.19 and 2.20.

$$\bar{C}_Q = \frac{Nc}{2\pi S} \int_{\text{up/down}} C_T \left(\frac{V_{rel}}{V_\infty} \right)^2 \mathrm{d}\theta \tag{2.19}$$

$$C_P = (\bar{C}_Q + \bar{C}'_Q)\lambda_{EQ} \tag{2.20}$$

This DMST model, with the Beddoes-Leishman dynamic stall model explained in Section B implemented, will be used for load comparisons with the experimental results. It is expected to give reasonable results in the first actuator disk, but poor results in the second.

2.5.2 2D free vortex lifting-line model

In this section a simple vortex method is outlined which will ultimately be coupled to a dynamic stall model. It has been decided to develop a 2D free vortex lifting-line model, as for instance applied by Strickland [48] and described by Paraschivoiu [29]. The lifting-line model is a relatively simple model, that predicts the loads on VAWT with a much higher confidence than the BEM, but is faster in calculations than panel models, although slower than BEM models. The current model follows the description of T. Berdowski [4]. In this model the airfoil is replaced by a single vortex bound at the quarter-chord point.

Free vortices are shed into the wake, which will define the induced velocity field. The importance of such a vortex model lies in the fact that a VAWT operates in its own wake downstream. A BEM method will be unable to capture the occurring phenomena of vortex interactions, which have a very significant influence on the local induced velocities when the blade loadings become high (for high tip speed ratios and high blade solidities). Although the lifting-line model covers a very simplified representation of the airfoil, it is still a very valuable tool for an overall prediction of the turbine's aerodynamic performance.

Model description

A bound vortex at the airfoil defines the lift. Due to the 2D assumption no trailing vortices are apparent. At the trailing edge, free vortices will be shed which will move with the free stream. Each vortex has a certain strength Γ which results in an induced rotating flow field around the vortex center. The velocity field is thus defined by the free stream wind, and the velocities induced by the bound and shed vortices. The total velocity representation at a certain control point in space and in the reference frame of that control point, is given in equation 2.21. As this is the representation in the point's own reference frame, it also includes the relative velocity due to the motion of the point itself in the fixed reference frame.

$$\mathbf{V_{cp}} = \mathbf{V}_\infty + \mathbf{V_{rot}} + \mathbf{V_\Gamma} \tag{2.21}$$

An essential part of a vortex model is the calculation of the induced velocities by all the vortices. The Biot-Savart law gives the velocity at an arbitrary point in space induced by a vortex at a certain distance. The Biot-Savart law in its general form is given by equation 2.22. **dl** is the length of the vortex segment, **r** is the vector between a certain control point in space and the vortex segment. **dV** is the speed in the control point. Note that a singularity occurs in the center of the vortex where the velocity is infinite.

$$\mathbf{dV} = \frac{\Gamma}{4\pi} \frac{\mathbf{dl} \times \mathbf{r}}{\|\mathbf{r}\|^3} \tag{2.22}$$

As the model is 2D, the bound vortex and shed vortices will extend to either the boundaries of the fluid or infinity in both directions in and out of plane. If the Biot-Savart law is applied on an infinite long and straight vortex filament, equation 2.22 can be rewritten in the form of 2.23. r is the perpendicular distance between the vortex filament and the control point. The velocity V at the control point is then given in the same direction and in the plane of the circulation Γ.

$$V = \frac{\Gamma}{2\pi r} \tag{2.23}$$

Kelvin's circulation theorem states that the circulation remains constant over the fluid, in case of an inviscid, incompressible flow which is only subject to conservative forces. This means that the change of circulation is equal to zero as in equation 2.24 and represented in Figure 2.17. Any bound vortex strength that is being built up on the airfoil, has to be counteracted by a contra rotating vortex of equal strength. According to the Kutta condition, this vortex is shed into the wake at the trailing edge. This shed vortex will travel with the free stream, and will maintain its strength as the flow in the fluid is assumed potential and thus no viscous phenomena will occur that can change that vortex strength.

$$\frac{d\Gamma}{dt} = 0 \tag{2.24}$$

The vortex strength is related to the lift per unit span L' at the vortex center via the Kutta-Joukowski theorem as in equation 2.25. The lift is defined as being perpendicular to the far upstream velocity V_∞ relative to the vortex, and the notation is for an anti-clockwise positive circulation. For an airfoil represented by a single lifting-line, the bound vortex at the quarter point on the chord represents the total circulation around the airfoil. The strength of the bound vortex (and therefore the strength of the shed wake) can thus be found by using this theorem if the lift is known. The lift on itself is however a function of the effective angle of attack, for which the induced velocities from the shed vortices have to be known as shown in equation 2.26 and 2.27. Hence, an initial lift or bound vortex strength has to be guessed, after which an iteration procedure will lead to a convergence of the solution of the correct lift and vortex strengths. Note that if the free vortices in

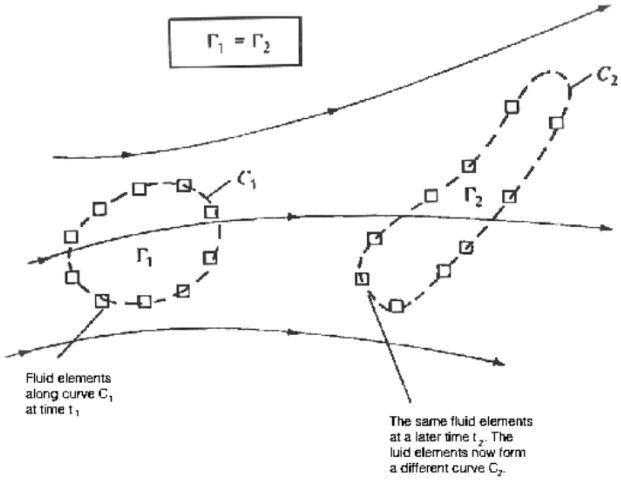

Figure 2.17: *Kelvin's theorem [1].*

the wake are not subjected to a lifting force, as these vortices move with the free stream, the relative velocity and thus the lift is zero in this case.

$$L' = -\rho_\infty V_\infty \Gamma \tag{2.25}$$

$$L' = C_l(\alpha_{eff})\frac{1}{2}\rho V^2 c \tag{2.26}$$

$$\alpha_{eff} = \alpha - \alpha_i = \tan^{-1}\left(\frac{V_{z,\infty} + V_{z,rot} + V_{z,\Gamma}}{V_{x,\infty} + V_{x,rot} + V_{x,\Gamma}}\right) \tag{2.27}$$

A full description of the vortex model is given at this point. With the implementation of Øyes dynamic stall model, described in Section 2.6.1, the results can be compared to those of the experiment.

2.5.3 Inviscid panel model

The panel model is the third numerical model that was used. It was constructed with the panel model presented in the work of C.J. Simão Ferreira [43]. Panel methods are in fact an extension to vortex methods in that they model the wake in a similar fashion. Beneficial, is that they do not require C_l and C_d data of the airfoil, but rather model the geometry directly using the Laplace equation for inviscid/incompressible flow or the Prandtl-Glauert equation for inviscid flows with compressibility effects ($M < 0.6$).

The airfoil will be discretised in sources and doublet panels that form the airfoil (Figure 2.18 black dots). At every panel, a Dirichlet boundary condition will be set (no flow through the panel) of uniform potential inside the airfoil. The wake of the airfoil is modelled with doublets, whereas the mid and far wake is modelled with vortex points. The Kutta condition will be set at the trailing edge of the airfoil. The airfoil experiences

a perceived velocity/potential varying over the surface as a result of the relative motion of the blade, the incoming wind and the potential induced by the wake and the other airfoils (blades). A simple cutoff radius is applied to overcome the singularity at the vortex core. A second order differentiation is used for calculation of the blades displacement. In Figure 2.18 a representation of the model is given.

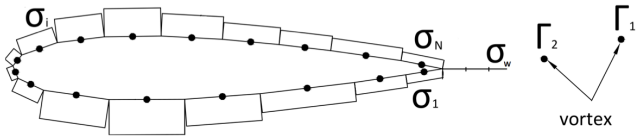

Figure 2.18: *Representation of panel distribution over the airfoil and in the wake for a panel model.*

This model is inviscid, and has no dynamic stall model included. The model is not expected to give good results for the TSR 2 case, but should give reasonable results for the TSR 4.5 for the normal forces. Due to the inviscid flow, the tangential forces are insignificant.

This model was set up with a different solidity than the experiment. Since this model in inviscous, the solidity is changed as shown in Equation 2.28, according to Simão Ferreira. The solidity was changed from 0.12 to 0.095 for the inviscid panel model.

$$\left(\frac{\mathrm{d}C_l}{\mathrm{d}\alpha}\sigma\right)_{inv} = \left(\frac{\mathrm{d}C_l}{\mathrm{d}\alpha}\sigma\right)_{viscous} \tag{2.28}$$

2.5.4 Double wake panel model

Another numerical model that was used to simulate the conducted experiments, was the double wake panel model. This model was constructed by A. Zanon [59] and solves the unsteady potential flow panel equations together with the integral boundary layer equations. The double wake panel model is an extension to the panel model in such that it can solve airfoils in (dynamic) stall.

The theory behind this model is when the flow around an airfoil is separated, vorticity is continuously shed along the shear layer between the flow and the separation bubble. The boundary layer model predicts the location of this separation point by using Drela's integral approach for steady flows [10], which is based on von Karmans momentum equation and shape parameter equation. A simplified e^N method is used to approximate the laminar-turbulent transition.

The value of the skin friction coefficient $[C_f]$ is used in the current model as the separation criterion. When C_f becomes negative, the flow is reversed, and separation has occurred. This technique has proved reliable in previous work [37], but fails when applied to medium-low Reynolds numbered pitching airfoils. The model does not allow for the re-attachment

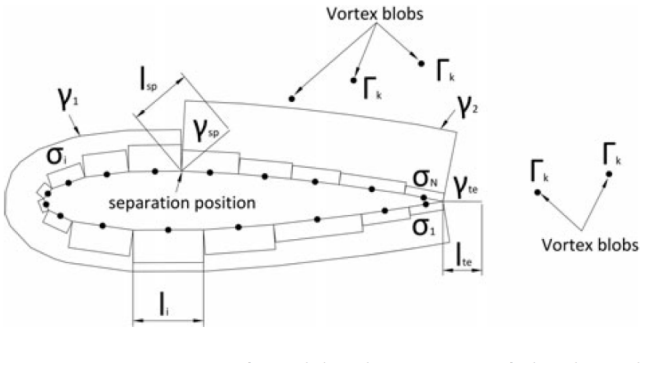

Figure 2.19: *Representation of panel distribution over the airfoil and in the wake for a double wake panel model.*

after deep stall occurred at the leading edge. Therefor, a criterion prescribed by [58] is used to compensate the turbulent re-attachment.

The double-wake model is able to capture the complex evolution of the vorticity field associated to the energy conversion process of the VAWT. Since the model takes into account a viscous boundary layer, the predicted values of the loads can be used directly from the model on the experiment.

2.6 Dynamic stall models modified for wind energy applications

In Section 2.5 the numerical models used for comparisons with the experimental loads are explained. The BEM model and the lifting line model needed an extra DS model to model the loads of a blade in DS. In this section the DS models used are more elaborated. These models are a simplification, or modification of the BL model explained in Appendix B.

Originally, DS models were created for helicopter purposes. There is a big difference between helicopters and wind turbines. Wind turbines are mostly in the incompressible flow region (M<2), and the rotational frequencies are much lower. Most of the DS models were adapted from the helicopter industry in order to fit the wind turbine purposes. As a consequence, nowadays multiple dynamic stall models exist in the wind turbine industry: Øye (1991), Risø (2004), ECN (2004), Larsen-Nielsen-Krenk (2007), BL (2008-2011). The models described in this section are the models used in the previous described models. In order to simulate the experiment namely the Øye and the BL are used. The Øye was chosen due to its simplicity, while the BL was chosen because of the completeness of the model.

2.6.1 Øye model (1991)

An early model developed for wind energy applications is a method proposed by Øye in 1991 [16]. They strived for a model that did not need all the unsteady flow description as

found in the models designed for helicopter purposes. Øye left out the unsteady attached modelling, the compressibility effects, and the leading-edge vortex lift contribution. A basic relationship of the unsteady separation is left. In this model, the same static data requirements are used, such that the model is of the first category semi-empirical dynamic stall models. On the other hand, Øye used a simple linear first-order filter model, where he replace the static separation parameter f by an interpolation between the stationary attached lift coefficient C_{L0} and the static lift coefficient at fully separated flow C_{L1}. At the separation AoA (α_{sep}) of the airfoil, the flow is assumed fully separated. The C_{L1}-curve runs from the point of $C_{L0} = 0$ to $C_L(\alpha_{sep})$ by a hermit interpolation, where the initial and final slopes are $\frac{1}{2}$ and $\frac{1}{12}$ of the slope of $\partial c_L/\partial\alpha|_{\alpha_0}$ respectively. f follows from Equation 2.29. The dynamic separation parameter f_d is found by the approach with indicial functions, the same as for the BL model as presented in Equation B.6. The dynamic lift coefficient $C_L(t)$ is gathered by substituting $f(\alpha)$ with $f_d(t)$, $C_L(\alpha)$ and $C_L(t)$ in Equation 2.29 to obtain Equation 2.30. This is the final dynamic lift coefficient, since no other effects are modelled than the unsteady separation. In the state-space representation of the system, only one differential equation is needed in order to obtain the single state variable f_d, shown in Equation2.31.

Øye assumed that there are only two profile dependent variables needed, the time constant for the description of the dynamic separation parameter ω_3, and the static angle of attack at full separation α_{sep}. Øye also used the flat plate approach for the definition of $\partial c_{L0}/\partial\alpha$, which results in the initial and final slope of C_{L1} to be equal to π and $\pi/6$ respectively.

$$f(\alpha) = \frac{C_L(\alpha) - C_{L1}(\alpha)}{C_{L0}(\alpha) - C_{L1}(\alpha)} \tag{2.29}$$

$$C_L(t) = C_{L,d}(t) = f_d(t)\left(C_{L0}(\alpha) - C_{L1}(\alpha)\right) + C_{L1}(\alpha) \tag{2.30}$$

$$\mathbf{z}(t) = \left[f_d(t)\right], \quad \mathbf{A} = \left[-\omega_3\right], \quad \mathbf{b}_0 = \left[\omega_3 f(\alpha)\right], \quad \mathbf{b}_1 = [0] \tag{2.31}$$

2.6.2 Adapted Beddoes-Leishman model by Sheng, Galbraith, and Coton (2008)

The BL helicopter model showed some deficiencies when applied on a wind turbine. According to Sheng, Galbraith, and Coton [41] these deficiencies are: a too early prediction of the stall onset, a lack of including stalled flow convection over the upper surface during the return phase, and that a negative chord wise force in the fully separated state is not accounted for in the model. They proposed some modifications: a new stall-onset criterion replacing the Evans-Mort correlation, a new modelling of the return from the stalled state, a new formula for the chord wise force, and a revision of the dynamic vortex formation and convection modelling.

2.6.3 Adapted Beddoes-Leishman model by Pereira, Schepers, and Pavel (2011)

From the data gathered by the MEXICO (Model Rotor Experiments under Controlled Conditions) experiment, [32], the BL model is validated for a HAWT under presence of yaw misalignment. In the validation, it is assumed that the flow is incompressible and unsteady thick airfoil data is included. The unsteady thick airfoil data indicates that the validation could not omit a leading-edge separation, regardless of the thickness. Therefore, they provide a linear relationship for the leading-edge separation AoA, depending on the leading-edge thickness at 1.25% of the chord length. The time constants for the attached flow are adopted from the BL model, as these can be assumed Mach number and airfoil shape independent to a large extent. The time constants related to the separated case (the pressure lag, vortex lift, and viscous lag constants) need to be gathered from experimental data, since they are strongly dependent on both the Mach number and the airfoil shape. Data for the time constant related to the pressure lag was not available, and therefore also adopted from the BL model.

CHAPTER 3

EXPERIMENTAL SET-UP & IMAGE PROCESSING

When an overview of the theoretical background of this research is created, phase 1 of the research in Figure 1.2 is terminated. This means inevitably the beginning of the next phase (phase 2); the experimental phase. In this chapter the experimental phase is fully covered.

To start, the conventions and the turbine reference system used are explained in Section 3.1. These are necessary basics to understand the set-up of the experiment, explained in Section 3.2.

How the PIV images are acquired, with the reference frame of the experiment, and what issues were involved with taking those PIV images, can be read in Section 3.3. The positions at which the PIV images are taken is elaborated in Section 3.4.

How the images are processed is explained in Section 3.5. These processed images can be stitched together, and can form an entire flow field around the blade. This can be seen in Section 3.6.

3.1 System of reference and conventions

To make the presentation and the following discussion on the results easier to follow, some common terminology has to be defined. Following the work of Simão Ferreira [43] and Tescione et al. [50], the blade orbit is divided in 4 regions:

Here, θ is the blade azimuthal position and $\theta = 0°$, $90°$, $180°$ and $270°$ are respectively the most windward, upwind, leeward and downwind positions, as seen in Figure 3.1. The adopted division refers to the blade orbit. The coordinate system is a Cartesian frame with origin at the turbine center; x-axis directed positively downwind the turbine, positive y-axis pointing to the windward side and z-axis positive upwards. A positive rotation of the turbine is counter clockwise seen from the top.

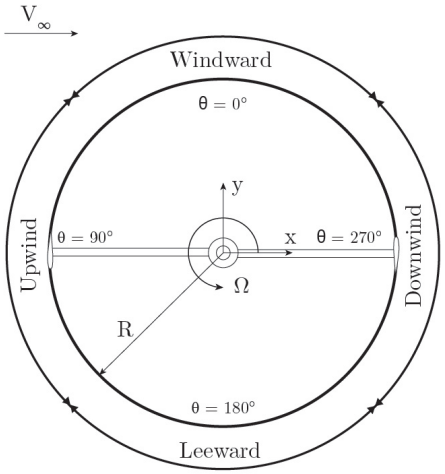

- upwind: $45° < \theta < 135°$;
- leeward: $135° < \theta < 225°$;
- downwind: $225° < \theta < 315°$;
- windward: $315° < \theta < 45°$;

Figure 3.1: *Schematic of the blade motion on the VAWT [50].*

3.2 Experimental set-up

In this section all important aspects of the experimental set-up are discussed. In Section 3.2.1 the VAWT used is elaborated, and in Section 3.2.2 the wind tunnel that will be used to produce the flow around the blades of the turbine. Section 3.2.3 explains the operation conditions of the wind tunnel. This is important as it will affect the reynolds number and the tip speed ratio of the turbine. Finally in Section 3.2.4 the PIV system set up is presented which will capture all the required data from the experiment.

3.2.1 VAWT model

The VAWT is a H-type Vertical Axis Wind Turbine with two blades. The blades are 1m long, and the turbine has a radius of 0.5m. The profiles of the blades are a NACA0018 and have a chord of 6cm. Considering the chord-based Reynolds number range of the tests, the airfoil has been tripped[1], to avoid the occurrence of laminar separation bubbles [25, 53], and to limit the level of unsteadiness of the blade flow. The blade-tower connection is obtained with two aerodynamically profiled struts (NACA0030, chord 0.046 R) per blade, installed at 0.18 R from the blade tips. The location of the connections minimises the maximum deformation at blade mid-span and blade tips due to centrifugal effects. The strut-blade connection has been shaped to minimise the flow interference [50]. Each blade is supported by two aerodynamically profiled struts (0.5m) mounted at 0.2 R inboard of the blade tips, giving an aspect ratio of 1.8 and a blade solidity of 0.11 [50]. The entire turbine model, including blades, struts and supporting shaft is painted in black to reduce laser reflections. The VAWT model can be seen in Figure 3.2.

The turbine is supported by a 3m steel shaft which is connected to a Faulhaber® brushless DC motor at the bottom of the shaft. The maximum output power of the motor is 202W.

[1] A 3D-turbulator tape developed by Glasfaser Flugzeug (6 mm point distance, 0.20mm thick, 12mm width, 60° zig- zag tape) at 8% of the chord on both sides has been applied, following the recommendations [25, 50, 53].

The motor is connected to a 5:1 gearbox system, which ensures the torque to be high enough for the operating regimes. On the shaft a trigger is installed to ensure the right timing for the phase locked PIV system. Every time it triggers (once per revolution) the PIV system will take a picture at the desired azimuthal angle.

3.2.2 Open jet wind tunnel facility

The PIV experiments have been conducted in the Open Jet Facility (OJF) of TU Delft. The OJF is a closed-circuit, open-jet wind tunnel with an octagonal nozzle of 2.85 x $2.85m^2$ and a contraction ratio of 3:1. The tunnel jet is free to expand in a 13.7 x 6.6 x $8.2m^3$ test section. Driven by a 500kW electric motor, the OJF delivers free stream velocity range from $3\frac{m}{s}$ to $34\frac{m}{s}$ with a flow uniformity of $\pm 0.5\%$ and a turbulence level of 0.24% [35]. A 350 kW heat exchanger maintains a constant temperature of $20°C$ in the test section. A schematic of the wind tunnel is shown in Figure 3.3.

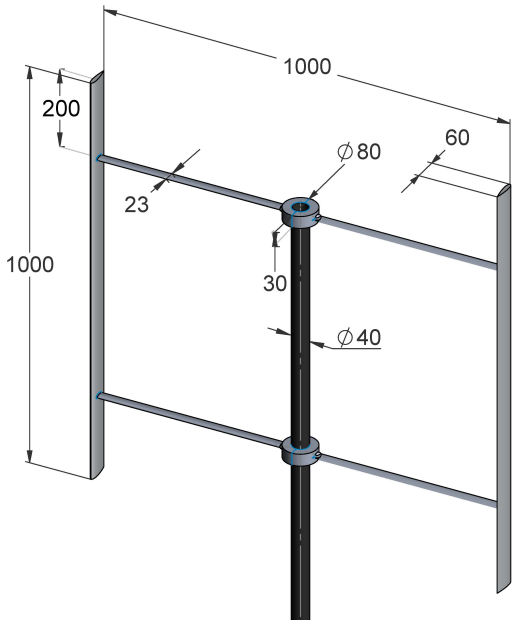

Figure 3.2: *The VAWT model.*

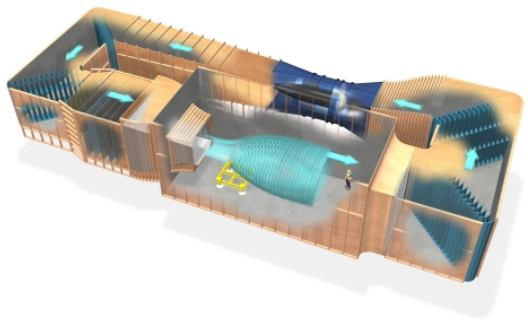

Figure 3.3: *Schematics of the OJF [36].*

The model is placed in the middle of the OJF's test section at 1m away from the nozzle. This means the turbine is in the potential core of the jet [22], and it can be said that the flow has not lost any velocity due to flow expansion in the test section [22]. No extra loss for flow expansion needs to be considered.

3.2.3 Operation conditions

The experiment is conducted for two TSR. Due to engine shortcomings, the Reynolds-Number (Re) could not be equal for both TSR. Since it was more important to perform the experiment at the right TSR, the experiments were opted to be conducted at different

Re-numbers. The Re-numbers are calculated with Equation 3.1 and are presented, with their according TSR, in Table 3.1.

$$Re = \frac{\rho \omega R c}{\mu} \tag{3.1}$$

The influence of the Re-number on the experiment is the slope of the $C_l - \alpha$ and $C_d - \alpha$ -curve as shown in Figure 3.4. The influence of the Re-number becomes smaller when going into low regimes. All necessary data $(C_l, C_d - \alpha)$ for the a range of Re-numbers varying from $10 \cdot 10^3 - 5 \cdot 10^6$ were documented for AoAs from -180 to 180 [°] [40]. This data can be used for the conditions of this experiment.

Table 3.1: *Operating conditions for both TSRs.*

Tip Speed Ratio [-]	Free Stream Velocity$[\frac{m}{s}]$	Reynolds Number [-]
4.5	9.1	163300
2	10.2	83063

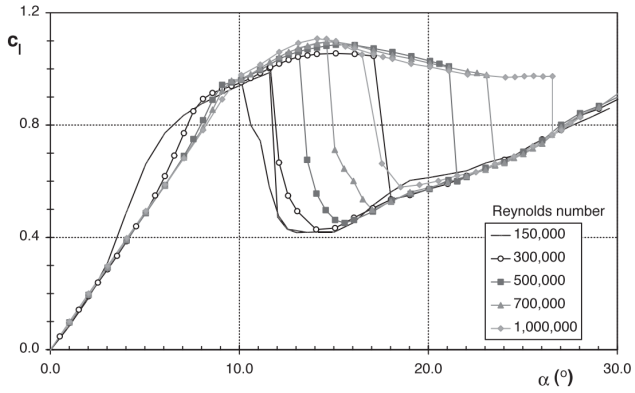

Figure 3.4: *The influence of the Re-number on the C_l-curve [53].*

3.2.4 PIV set-up

For capturing all the velocities around the airfoil, PIV is used. The set-up of the PIV-equipment is explained in this section. In Figure 3.5 the whole set-up can be seen. All the different aspects that were explained in Chapter 2.3 are put in place.

Seeding generator

The Safex Fog Generator was set in the wind tunnel. In principle it is not of great importance where the fog generator is placed. Important is the distribution of the particles are equally distributed in the test section, and that the fog generator can be operated from the control room.

When placing the fog generator, keep in mind it uses a lot of fluid. Since the testing can take a long time, the liquid might run out during the tests. This should be prevented at

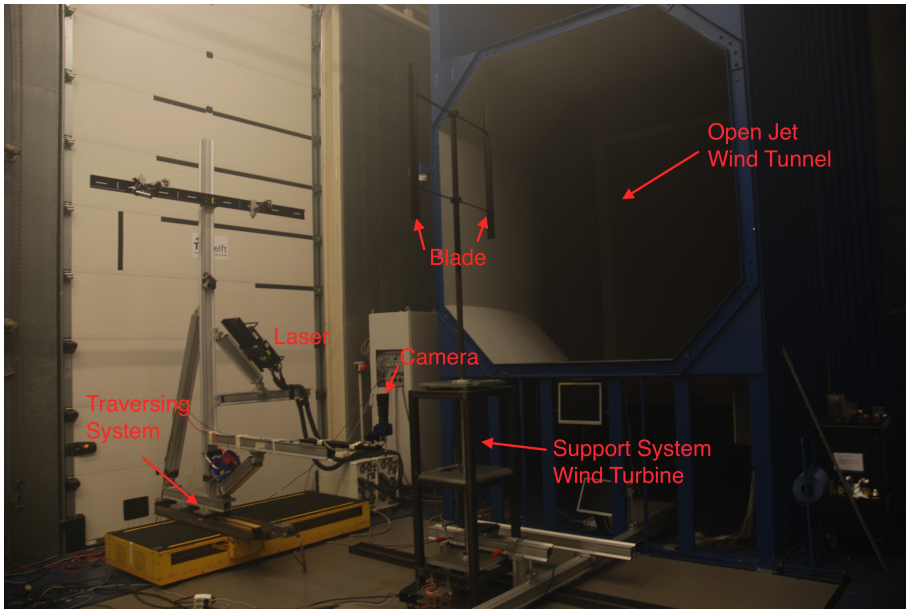

Figure 3.5: *The set-up for the PIV system.*

all times, since the particle distribution is an important aspect for minimising the PIV errors. The fog generator was positioned with easy access for refilling.

Traversing system

To run all experiments smoothly, a traversing system was used on which the camera and the laser were mounted. In Figure 3.5 the traversing system is displayed (yellow box left-bottom corner). On top of the traversing system, a truss structure was build to position the laser and the camera at the correct location for the PIV measurements.

The advantage of having a traversing system is the set-up and calibration only needs to be done once. The traversing system can position the camera and laser at any coordinate in its range up to an accuracy of 0.001m from its initial position.

Laser

In a previous experiment conducted by Tescione et al. [50], one single laser sheet was shot on the blade element and two cameras shooting from the bottom. It was found that the waste due to the shadow of the laser was quite large. To compensate this effect, it was opted to have two laser sheets shooting at the same section from different angles. Waste due to the shadows of the laser by using this technique is minimised.

In Figure 3.6 the laser set up is shown. It was shooting at a 45° angle and was split in two beams, one going straight, the other reflected by 90°. At this point, the beams are: travelling at 45°, and the other at -45°. Following the instructions of Raffel [33], with the use of mirrors, diverging and converging plates (and some skill) the laser beams are made into two sheets, which both have their minimum thickness at the positions of the blade (middle section of the turbine, 2970mm height).

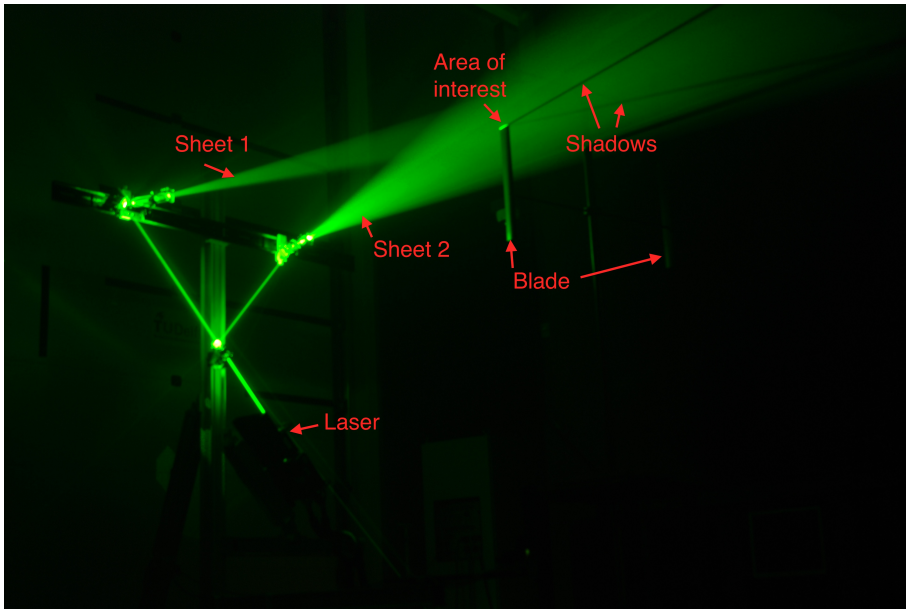

Figure 3.6: *The set-up for the laser.*

In Figure 3.6 the shadows of both sheets can be seen. Although these shadows are compensated by the light of the other sheet, there is still a small area right behind the blade that is not illuminated. This is the only blind spot that will exist due to laser shadows. In this area no particles can be captured, and no velocity components can be found.

CCD camera

The Camera was connected to a long spar on the traversing system, seen in Figure 3.7. The camera is attached to the end of the spar, with the lens looking upwards. This was calibrated with a spirit level, and made sure that in every direction the camera was levelled to minimise errors.

The maximum height of the lens is still kept beneath the jet exhaust, to keep disturbances due to the jet minimal. What should be taken into account, because of the low position of the camera, is that the camera is able to hit the support system of the wind turbine, as can be seen in Figure 3.7. This is more elaborated in Section 3.3.

The length of the spar on the traversing system ($\approx$ 2.5m) was calculated that when the camera is capturing the leeward positions, the laser system will still have a safe distance from the blades in the windward position. No disturbance will be felt by the turbine from the laser system, or the camera.

Calibration

For the calibration of the whole system, a plate with millimetres paper was used. This plate was set at 2970mm height, so the mid positions of the blade. The calibration had two main objectives: calibrating the two laser sheets, and calibrating the camera.

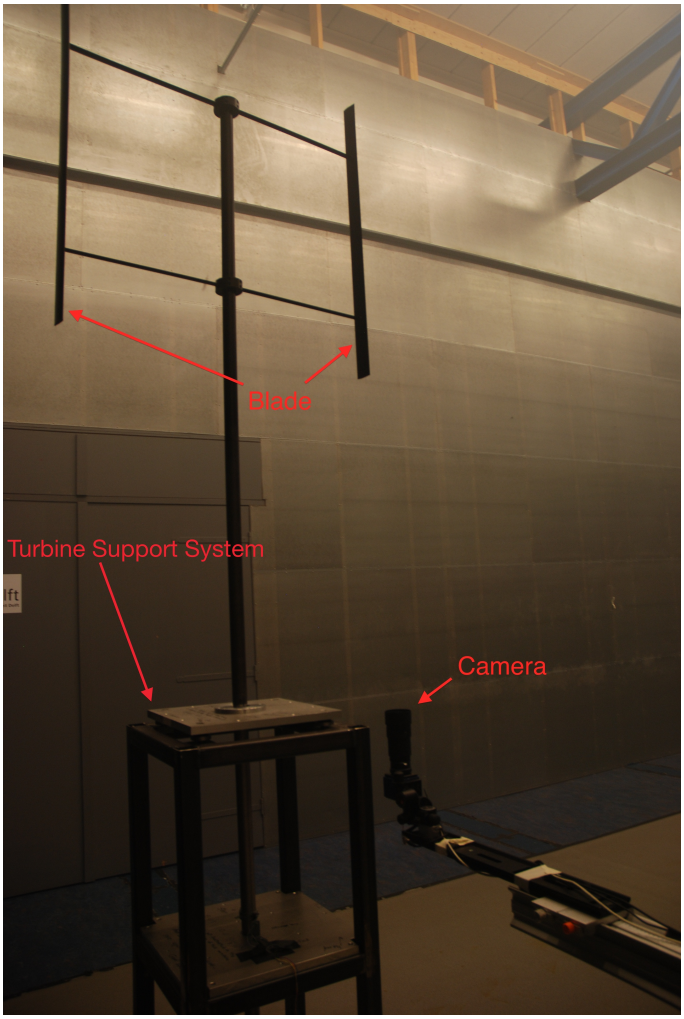

Figure 3.7: *The set-up for the camera.*

The plate was first set vertically, with the millimetres paper pointing towards the lasers (see Figure 3.8). The plate was calibrated with a spirit level laser (red laser in Figure 3.8), and the lasers are set at the same height with the use of the horizontal lines on the millimetres paper. To know that they are calibrated to the middle of the turbine, the spirit level laser was set to the middle of the turbine.

When the lasers are both perfectly horizontal and at the same height, the plate is turned horizontally (Figure 3.9), and once more calibrated with a spirit level. The camera can now be focussed on the plate, and a picture of the millimetre paper can be shot. This gives us the length scales for the pictures that will be used during the PIV measurements. This calibration picture can be inserted in DAVIS and the program will automatically calibrate all the pictures to the right length scales during the post-processing.

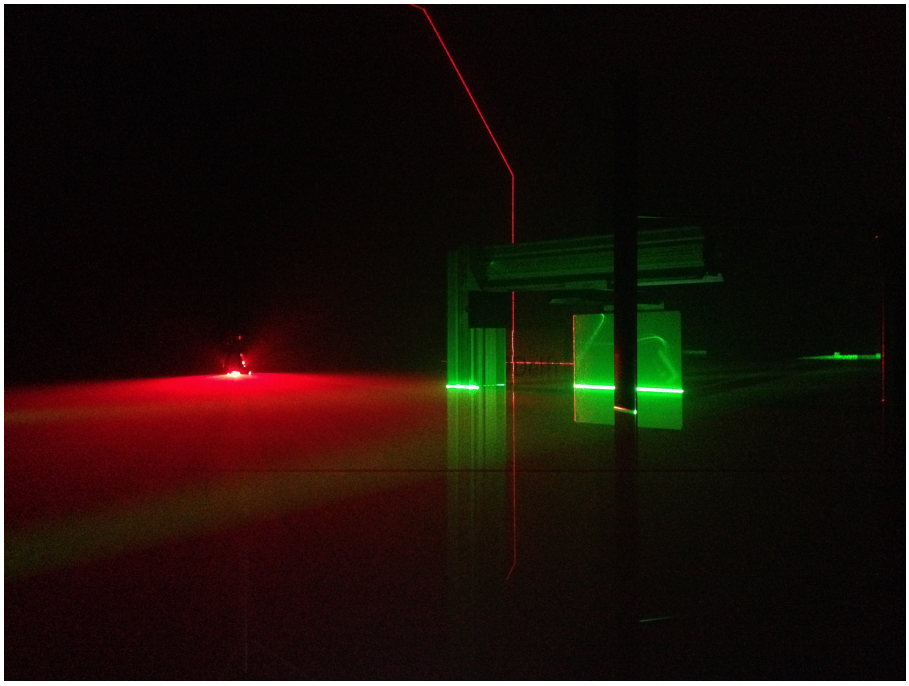

Figure 3.8: *Calibration of the lasers.*

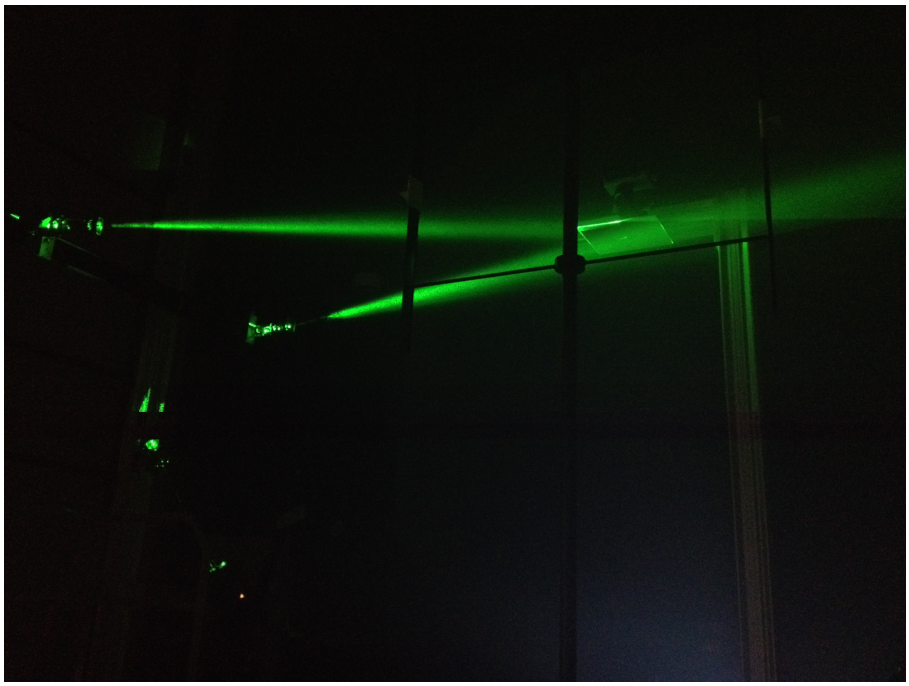

Figure 3.9: *Calibration of the camera.*

3.3 Image acquisition

In this Section the acquisition of the images is more elaborated. How a reference for the system is made in order to capture all azimuthal positions, is explained in Section 3.3.1.

All the issues related to the acquisition are governed in Section 3.3.2.

3.3.1 System of reference & field of view

In this section, a reference frame for the experiment is created. This reference frame is to position all the PIV hardware at the correct coordinate during the experiments. In Figure 3.10 the coordinate system of the traversing system, as well as the turbine coordinate system are presented, where the traversing coordinate system is used during experiments and the turbine reference frame for processings.

Camera & traversing system reference frame

The traversing system can move in two directions: X and Y. This is rather convenient, however knowing the exact position of the camera, with the use of a reference system, is an important aspect to minimise errors.

The origin of the camera and the traversing system reference where the blade is at the most upwind position of the rotor, at $\theta = 90°$ (see Figure 3.10). The x-axis is now defined parallel and with positive direction as the free stream flow vector. The y-axis is perpendicular on the x-axis, with the positive direction pointing to the left. This is done so the rotation of the turbine would be positive.

As can also be seen in Figure 3.10 there are red lines and red hashed areas on this figure. These are all the positions that the camera and traversing system are not able to reach. In the middle of the turbine, there is the turbine's support structure. Since the camera is able to hit this structure, good knowledge on where the camera can not go is needed. The hashed area in the bottom is the extreme position of the traversing system, which makes the camera also limited in this direction. These limitations should all be considered when the azimuthal positions are chosen in Section 3.4.

Turbine reference frame

For convenience in all calculations and processings, it makes more sense to have all the positions known in the turbine reference frame. Therefore a second coordinate system is shown in Figure 3.10. The origin of this reference frame lies in the centre of the turbine, with the x- and y-axis pointing the same direction as for the camera & traversing system reference frame. Switching from one reference system to the other is quite convenient, and shown in Equation 3.2.

$$\begin{aligned} X_{Turbine} &= X_{Camera} - R \\ Y_{Turbine} &= Y_{Camera} \end{aligned} \tag{3.2}$$

The reason the traversing reference frame and the turbine reference frame are not equal, is that when shutting down the traversing system, the system automatically resets its coordinates when waking up. Since the traversing system was not able to reach the origin of the turbines reference frame, it was convenient to have a separate, although very easily switchable, reference frame for the traversing system.

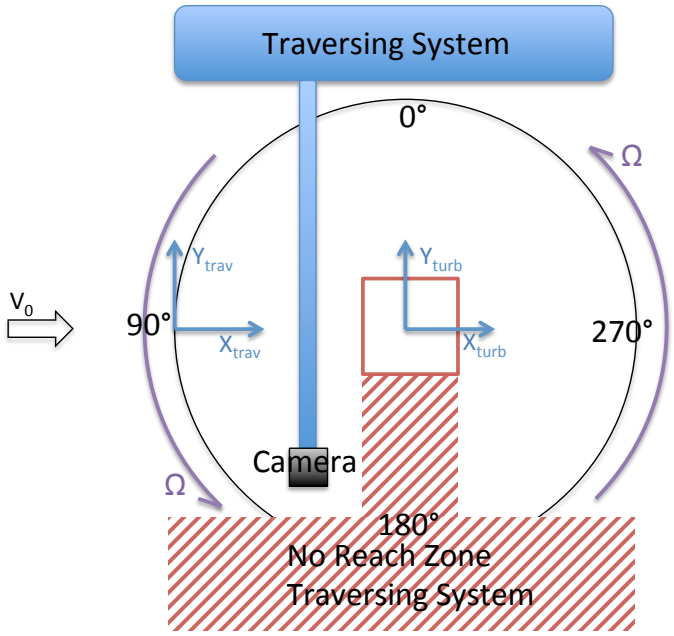

Figure 3.10: *Reference system of the traversing system and the VAWT.*

3.3.2 Acquisition issues

Since it is not just a matter of putting the camera beneath the blade and taking the pictures, all issues involving the acquisition are commented on in this section.

Azimuthal acquisition positions

The camera can not reach every possible positions around the turbine. Yet to capture the velocity fields around the entire rotation of the turbine, as much azimuthal positions around the turbine must be evaluated. All the azimuthal angles for which the flow fields are examined are presented in Section 3.4.

The alert reader should understand that there is one azimuthal position at which it is not possible to capture the velocity fields, namely the $\theta = 180°$ azimuthal position (see Subsection 3.3.1). For this position the blades were turned upside down, and the turbine was set to rotate in the other direction. This way the rotor had its $\theta = 180°$ position where previously the $\theta = 0°$ was[2].

Avoiding masked regions due to strut

In this particular experiment, the middle part of the blade is examined. When the camera would be positioned with the blade perfectly in the middle of the picture, the strut would cover particles in the section of interest. However, the FOV of the camera is quite large, so it is opted to put the camera more to the sides, such that the camera can see the airfoils

[2]The blades were entirely calibrated again before the turbine was set to rotate in the other direction. This was done to prevent errors.

in one of its corners. In Figure 3.11 it can be seen that the two cameras are shooting sidewards to the section of interest. In the post-processing the velocity fields can be put back together to one entire velocity field field (see Section 3.6). This has two advantages, first advantage is that the area which is covered around the blade is larger, an the second advantage is the velocity field will be without any black spots due to the strut.

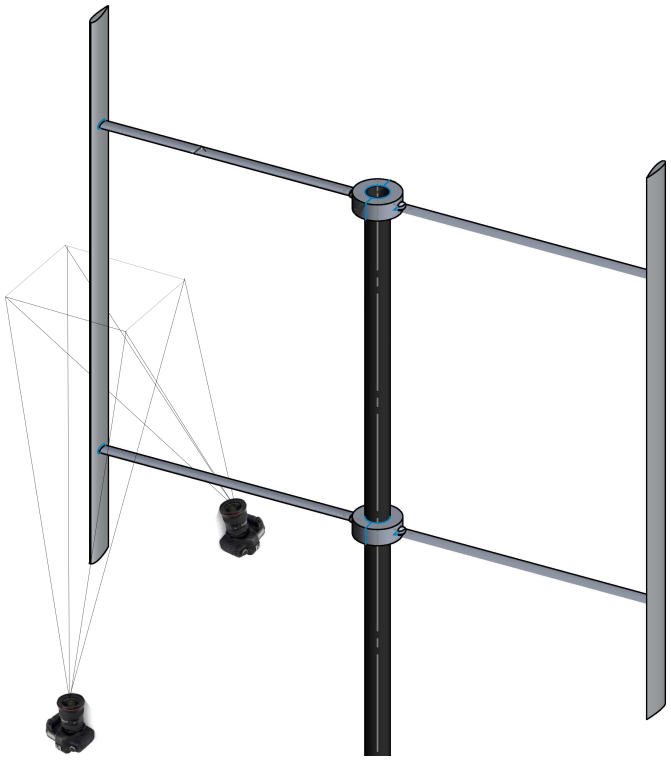

Figure 3.11: *Multiple camera positions are used to remove the lower strut in the stitched velocity field.*

3.4 Measurement cases

In Figure 3.12 all the acquisition positions are displayed. At most azimuthal positions, four pictures were shot in order to remove the strut. For two positions however, only two pictures were taken: 90 and 270°. Here the blade and strut chord are parallel to the long axis of the FOV. Only two pictures are needed to capture the entire field around the blade and remove the lower strut from the velocity fields. In Figure 3.12 all the positions are given a number, and their corresponding coordinates can be found in Table 3.2. All the acquisition positions are expressed in both the turbine and the traversing system reference frame in Table 3.2.

The entire test matrix is presented in Appendix A. In this matrix all the information about the wind tunnel parameters and the turbine parameters for every measurement position are also documented.

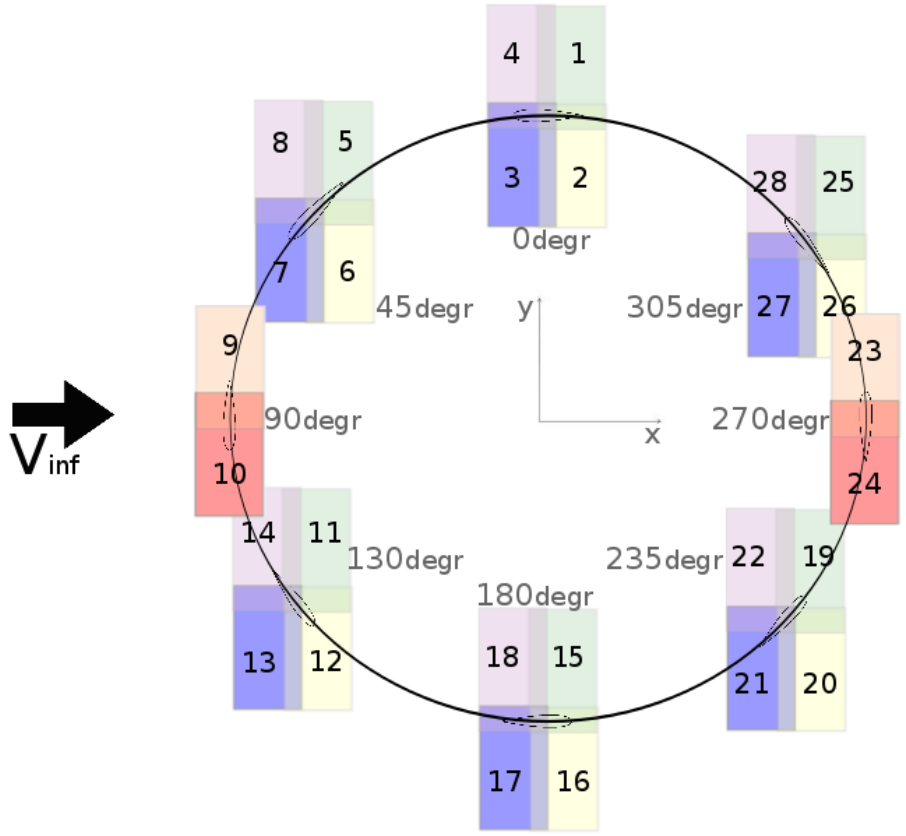

Figure 3.12: *The different positions of the camera.*

3.5 Image processing

LaVision® DAVIS [21] is used by the TUDelft university as processing tool for all the PIV experiments. In the data processing of PIV images (Figure 3.14), there are three important steps: pre-processing, processing and post-processing.

During the pre-processing, the background noise is removed by subtracting the minimum average. A 3x3 Gaussian filter was used to ensure a Gaussian profile shape and to reduce the effect of peak locking; spatial disparities of image intensity were excluded by removing the sliding background, seen in Figure 3.14.

In the processing phase, DAVIS uses a multi-pass correlation to come to the velocity field. The settings used for this experiment is a 16x16 pixel window, multi-pass with and a 50% overlap window. The technique is illustrated by Figure 3.13.

In the post-processing phase the outliers that arise in the cross-correlation results are removed using a median filter, as an example is show in Figure 3.16. These final results can be exported in DAT-format, which can be used as input for the MATLAB function. These DAT-files include:

- Velocity vectors: V_x,V_y,V_z,$|V|$
- Standard deviation: σ_x,σ_y,σ_z,$\sigma_{|V|}$

Table 3.2: *Measurement cases for the experiment.*

		Coordinate System				
		Turbine		Traversing System		Azimuth Angle
	#	X [m]	Y [m]	X [m]	Y [m]	θ [°]
TSR = 2 & TSR = 4.5	1	0.11	0.489	0.61	0.489	0
	2	0.1	0.37	0.6	0.37	0
	3	-0.04	0.37	0.46	0.37	0
	4	-0.04	0.489	0.46	0.489	0
	5	-0.28	0.47	0.22	0.47	45
	6	-0.26	0.32	0.24	0.32	45
	7	-0.39	0.25	0.11	0.25	45
	8	-0.39	0.47	0.11	0.47	45
	9	-0.475	0.14	0.025	0.14	90
	10	-0.475	-0.1	0.025	-0.1	90
	11	-0.333	-0.22	0.167	-0.22	130
	12	-0.327	-0.353	0.173	-0.353	130
	13	-0.43	-0.375	0.07	-0.375	130
	14	-0.43	-0.2	0.07	-0.2	130
	15	0.1	0.489	0.6	0.489	180
	16	0.1	0.39	0.6	0.39	180
	17	-0.1	0.39	0.4	0.39	180
	18	-0.06	0.489	0.44	0.489	180
	19	0.48	-0.2	0.98	-0.2	235
	20	0.48	-0.37	0.98	-0.37	235
	21	0.36	-0.37	0.86	-0.37	235
	22	0.36	-0.2	0.86	-0.2	235
	23	0.51	0.1	1.01	0.1	270
	24	0.51	-0.11	1.01	-0.11	270
	25	0.48	0.37	0.98	0.37	305
	26	0.48	0.2	0.98	0.2	305
	27	0.36	0.2	0.86	0.2	305
	28	0.36	0.37	0.86	0.37	305

- Reynolds stress: τ_{xy},τ_{xz},τ_{yz},τ_{xx},τ_{yy},τ_{zz}

This exported data is based on the local camera coordinate system. Important when inputting this data is reversing the coordinate system to the turbine coordinate system with the use of Figure 3.12 and Table 3.2.

3.6 Stitching of the images

When all data sets (DAT files) are given its turbine reference system coordinates, the images can be stitched together in order to come to a large velocity field around the blade. Each data set will have an overlap with one or more other data set. In this case

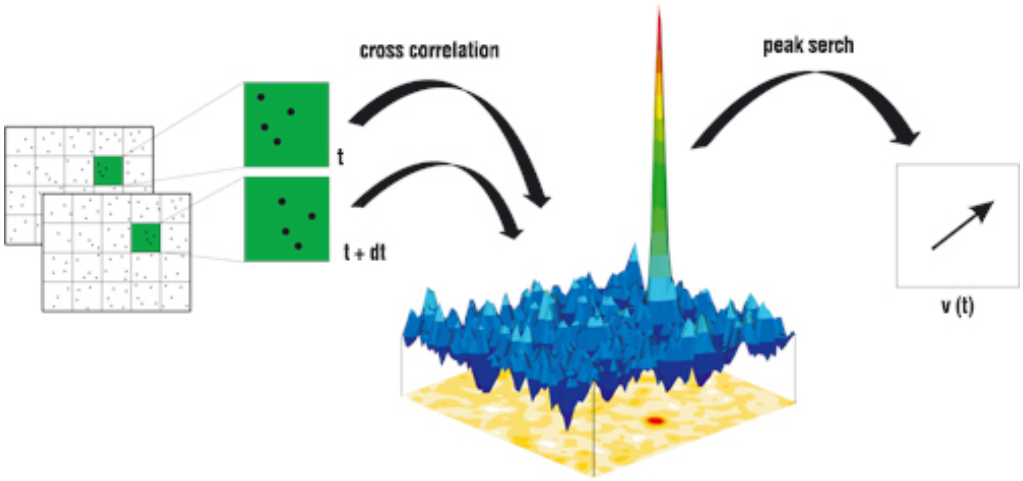

Figure 3.13: *The cross-correlation technique used by DAVIS [21].*

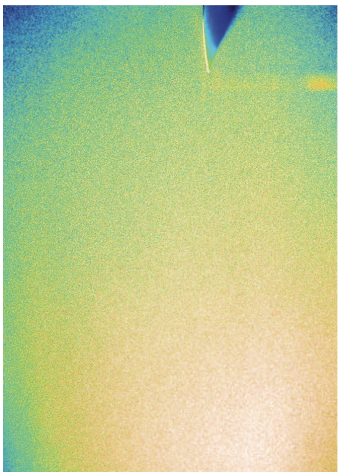

Figure 3.14: *The raw image taken in the experiment.*

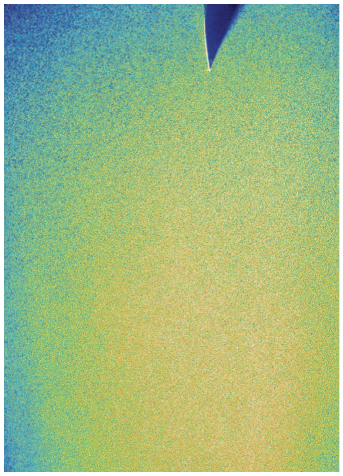

Figure 3.15: *The pre-processed image by DAVIS.*

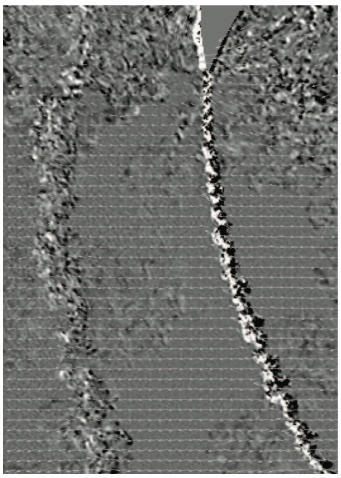

Figure 3.16: *The processed image by DAVIS.*

the best data will be used in the final velocity field. Areas that were not covered in one image can be compensated for by another image.

CHAPTER 4

UNCERTAINTY ANALYSIS

At this point, phase 1 and 2 in Figure 1.2 are terminated and explained. In this chapter the modelling phase (phase 3) is started. Before the actual loads are presented, and the comparisons with the different numerical models is performed, an uncertainly analysis of the entire method used in this thesis is conducted.

Two types of errors that can influence the measurement accuracy exist: random and systematic errors. Random errors are statistical fluctuations due to inherent imperfection of equipment or measurement techniques. Systematic errors are a result of a system bias. This causes the results to have a constant deviation from the actual value. In PIV measurement a mis-calibration is a common systematic error.

When the operational conditions are not constant during the measurements, prescribed quantities (e.g. free-stream velocity) or model operational conditions (e.g. rotational frequency) can get uncertainties in their instantaneous measurements. By averaging more instantaneous samples, the uncertainty can be decreased as shown in Equation 4.1.

$$\bar{M} = X_{True} + \frac{\sigma_{ins}}{2\sqrt{N_{Samples}}} \tag{4.1}$$

A convergence analysis was performed in order to to determine a proper number of averaging samples for which both TSR cases will converge. For the TSR 4.5 case, 150 samples of the flow was considered converged, whereas the TSR 2 case needed 200 samples to reach the same convergence level, see Figure 4.1.

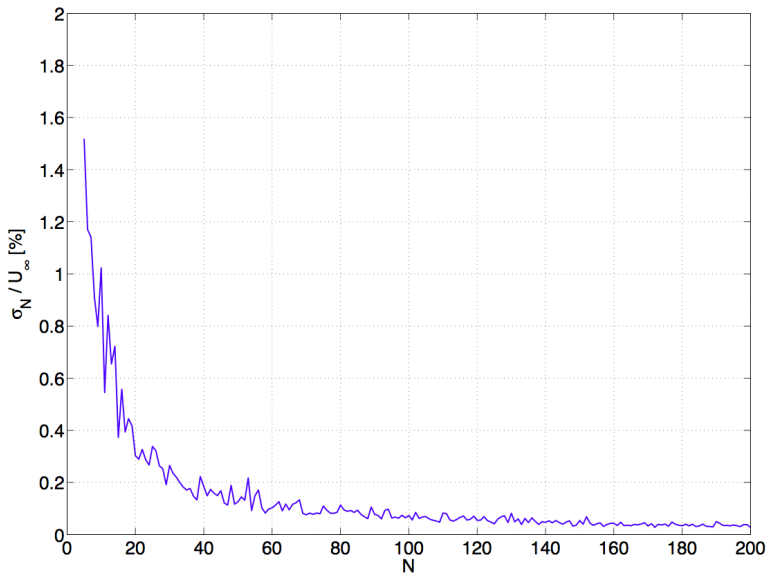

Figure 4.1: *Statistical convergence of the phase-locked mean components.*

Uncertainties can originate from different causes. In this chapter the most dominant causes will be elaborated:

- Uncertainty due to variations in free-stream velocity (Section 4.1.1).
- Uncertainty due to model imperfections and changes in model operating condition (Section 4.2).
- Uncertainty in PIV measurements (Section 4.3).
- Uncertainty in PIV data processing (Section 4.4).
- Uncertainty in the load calculation method (Section 4.5).

After the uncertainty analysis, some preliminary conclusions will be drawn based on the results. These will be used when presenting and discussing the results from the experiment. The preliminary conclusions are discussed in Section 4.6.

4.1 Uncertainty in the free-stream velocity

When considering the experiment, it is assumed there is a steady inflow of the free stream velocity. Although the turbulence intensity of the OJF is low, and the uncertainty on the free stream is below 1%, an analysis on the variation in the velocity, as well as the wind tunnel blockage due to the turbine, is investigated.

4.1.1 Variations in free-stream velocity

Variations in the free-stream velocity will induce force variations on the wind turbine and its blades. Fluctuations in temperature can have an effect on the free stream velocity.

For this uncertainty analysis, it will be assumed that the flow obeys the ideal gas law $p_\infty = \rho RT$. The tunnel sets a constant fan rpm for an inputted wind speed. This rpm is calibrated for a temperature of 20°C. During the tests, a temperature difference of +/- 0.7°C was noticed. With the OJF not being completely sealed, the static and the total pressure are assumed constant. By using the ideal gas law (Equation 4.2) the change in density can be calculated. These densities can be inserted in the Bernoulli equation (Equation 4.3), to find a difference in free stream airspeed about ±0.13% for both TSRs, which is neglectable.

$$\begin{aligned} upper\ bound: \rho_u &= \frac{p_\infty}{R \cdot T_u} = \frac{101325}{287.1 \cdot (19.3 + 273.15)} = 1.2068\ \frac{kg}{m^3} \\ lower\ bound: \rho_l &= \frac{p_\infty}{R \cdot T_l} = \frac{101325}{287.1 \cdot (20.7 + 273.15)} = 1.2010\ \frac{kg}{m^3} \end{aligned} \tag{4.2}$$

$$\begin{aligned} p_\infty + \frac{1}{2}\rho_l V_u^2 &= p_\infty + \frac{1}{2}\rho_u V_l^2 \\ \Rightarrow V_{l,TSR\ 4.5} &= \sqrt{\frac{\rho_\infty}{\rho_u}} V_\infty = \sqrt{\frac{1.204}{1.2068}} 9.1 = 9.0894\ \frac{m}{s} \\ V_{l,TSR\ 2} &= \sqrt{\frac{\rho_\infty}{\rho_u}} V_\infty = \sqrt{\frac{1.204}{1.2068}} 10.22 = 10.2081\ \frac{m}{s} \\ \Rightarrow V_{u,TSR\ 4.5} &= \sqrt{\frac{\rho_\infty}{\rho_l}} V_\infty = \sqrt{\frac{1.204}{1.2010}} 9.1 = 9.1114\ \frac{m}{s} \\ V_{u,TSR\ 2} &= \sqrt{\frac{\rho_\infty}{\rho_l}} V_\infty = \sqrt{\frac{1.204}{1.2010}} 10.22 = 10.2328\ \frac{m}{s} \end{aligned} \tag{4.3}$$

4.1.2 Wind tunnel blockage

The blockage effect of a closed wind tunnel can be calculated according to Ross et al. [38, 39]. The frontal area of the turbine is relatively small compared to the outlet area of the open jet wind tunnel. The wind tunnel blockage ratio can be calculated with Equation 4.4.

$$\epsilon_t = \frac{1}{4}\frac{ModelFrontalArea}{TestSectionArea} = 0.035[-] \tag{4.4}$$

Following Ross with the wind tunnel blockage ratio a new wind tunnel velocity can be calculated, as shown in Equation 4.5.

$$V = V_u(1 + \epsilon_t) \tag{4.5}$$

The increase in velocity is 3.5%. The assumptions made by Ross et al. are for a Savonius rotor type. In case of an H-type VAWT, this blockage will be less, but it is assumed that the blockage of the turbine for a closed jet can not be neglected.

CFD work of Simão Ferreira et al. [46] showed the blockage effect of the VAWT in the closed wind tunnel was negligible for his purposes. Since for a VAWT most induction is concentrated at the rotor axis height.

For the OJF facility, a lot of research is still done on this topic. According to Battisti et al. [2], the corrections used for turbines in closed and open wind tunnels are not valid for VAWTs. A project is proposed to investigate the blockage effect in the OJF [34] by turbines.

Following the CFD work of Simão Ferreira et al. [46] in the closed wind tunnel, it will be assumed the blockage of the turbine can be neglected for this experiment in the OJF. This assumption is made since the blockage in open wind tunnels will be lower due to the ability of the flow to expand in the open test section.

4.2 Uncertainty due to model imperfections and changes in model operational condition

An uncertainty can be added due to errors related to model imperfections, elaborated on in Section 4.2.1, or due to uncertainties in the operational conditions of the turbine, as explained in Section 4.2.2.

4.2.1 Model imperfections

The model used in the experiment was designed to have a 0° pitch angle. When measuring the leading and trailing edge positions of the blade at the most upwind positions for 70 cases, the pitch could be calculated for both TSR. Since the blades were replaced before conducting the TSR 2 experiment, different pitch angles are calculated for both cases.

In Figure 4.2 the resulting pitch can be seen for the TSR 4.5. It can be concluded that the turbine has, on average, a negative pitch of 0.83 +/- 0.07° in this case. This angle will be added to the numerical models to which the experiment will be compared in Section 5.2. For the TSR 2, it was found there was a 0° pitch angle. No compensation is needed in the numerical models for this TSR.

4.2.2 Operational conditions

The motor of the turbine was not able to keep the turbine spinning at a constant RPM. Although it should be stable at 13Hz, a variation between 12.8 - 13.05Hz was observed. This means there was a -1.5% error, and a +0.35% error on the TSR 4.5 case. At the TSR 2 it varied from 6.6 - 6.61Hz, meaning only an error of +0.15%. The uncertainties in TSR 2 will be much less due to fluctuations in the rotational velocity.

Due to the centrifugal forces, the blades will deform at the blade tips and in the middle of the rotor, which coincides with the measurement position. To compensate for this behaviour, the initial position of the blade (to be used for PIV processing) was taken while the turbine was already moving. This would compensate for the difference between standstill and moving due to the centrifugal forces.

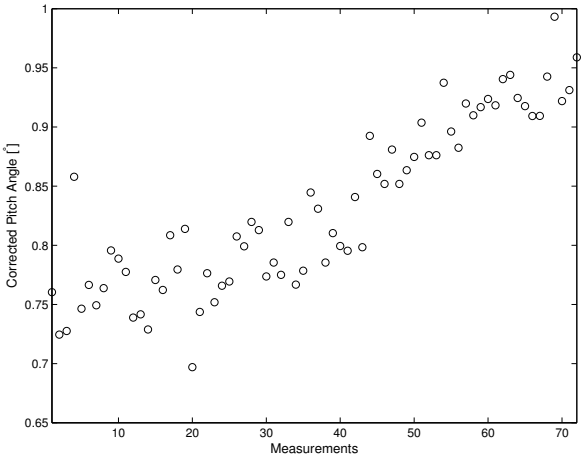

Figure 4.2: *The resulting Pitch angle = 0.83 +/- 0.07° for TSR 4.5.*

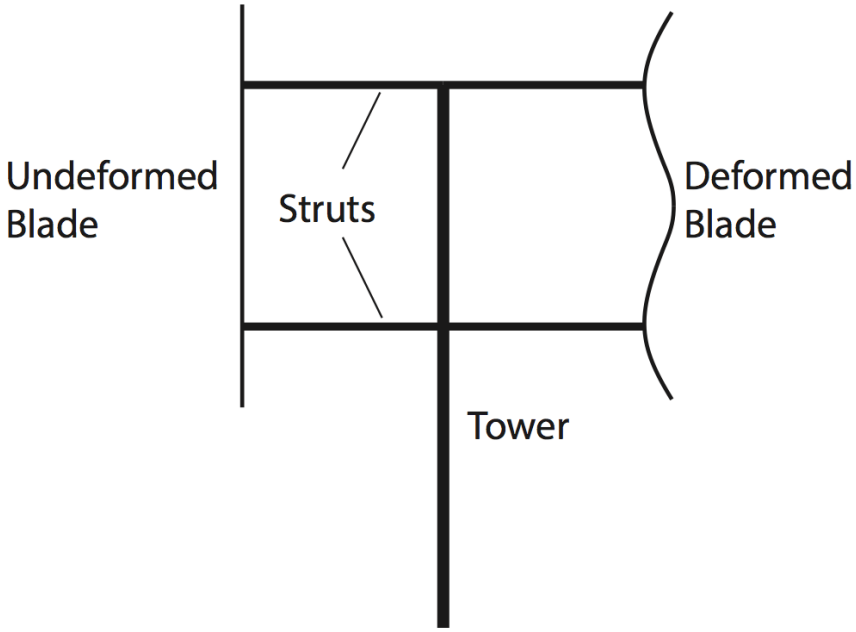

Figure 4.3: *Schematic of blade deformation (exaggerated).*

4.3 Uncertainty in measurements

Misalignments during the set-up of the experiment are a source of error in the results. If the camera calibration plate was not perfectly horizontal, there will be an out of plane component in the velocities. Same thing will occur with a misalignment of the laser sheet, or a (too) thick laser sheet.

Possible misalignment of the traversing system and the incoming flow direction would

result in step-wise window shift and relative rotation between neighbouring images. Over a large measurement distance, a small misalignment could add up to a significant error. Linear window shifts had been corrected manually by matching characteristic flow features at image boundaries, while image rotation had not been corrected for due to the complexity of angle determination. Since flow measurements were performed at different times, flow field misalignment was not completely removed after the corrections.

During the experiment, phase locking is the main source of error. By locating the leading edge of the blade in the phased locked images in the most upwind location, the position of the leading edges could be mutually compared between the images. It could be seen that the blade would never move more than 0.7° in azimuthal position from the original position in TSR 4.5 case, and not more than 0.5° for TSR 2. This error is small, but cannot be neglected; especially not for the calculation of the acceleration terms, as explained in Section 2.4.

To compensate for the error in radial direction, every shift in radial direction between the steps was calculated, as presented in Table 4.1. This reduces the amount of errors considerably. The resulting angles will be used to calculate the acceleration term of the load calculation method, as proposed by Noca et al. [28]. The azimuthal position that should be corresponding to 131° is in fact 136°, and will be disregarded in the calculations of the acceleration terms. At this position a backward scheme will be used to calculate the acceleration of the flow.

Table 4.1: *Difference in azimuthal positions.*

TSR 4.5					**TSR 2**				
$\theta_{T-1}[°]$	$\Delta\theta[°]$	$\theta[°]$	$\Delta\theta[°]$	$\theta_{T+1}[°]$	$\theta_{T-1}[°]$	$\Delta\theta[°]$	$\theta[°]$	$\Delta\theta[°]$	$\theta_{T+1}[°]$
359.014	0.986	0	1.356	1.356	359.054	0.946	0	1.263	1.263
44.013	0.988	45	1.117	46.117	44.114	0.886	45	0.886	45.886
88.521	1.479	90	1.723	91.723	88.92	1.08	90	0.984	90.984
128.22	1.78	130	6.046	136.046	128.972	1.028	130	1.229	131.229
/	/	/	/	/	178.782	1.148	180	0.82	180.82
234.298	0.702	235	1.117	236.117	233.718	1.282	235	1.161	236.161
269.348	0.652	270	1.294	271.294	269.014	0.986	270	0.445	270.445
303.828	1.172	305	1.696	306.696	304.41	0.59	305	1.368	306.368

4.4 Uncertainty in PIV data processing

Cross-correlation is a source of uncertainties in the data processing. The interrogation window size, overlap ratio, etc. are important processing parameters that have a strong influence on the uncertainties. In the pre- and post-processing phase a lot of external modifications (masked velocities, interpolated regions, etc.) have a big influence on these uncertainties (see also section 4.5).

At the present measurement scales the cross correlation uncertainty had a lower impact than other sources of uncertainties. Typical values for such an error had been reported less than 0.1 pixel for a range of window sizes down to 32x32 pixels [33]. Transforming to the velocity scale, this is equivalent to a displacement uncertainties of 0.01 mm in the horizontal measurements and 0.008 mm in the vertical measurements.

4.5 Uncertainty associated with load calculation method

A robustness check was done for the Noca method [28], the velocity fields are retrieved from the inviscid panel model developed by Simão Ferreira [43]. This simulation was modelled for a TSR of 4.5 with a solidity of 0.095, to compensate for the inviscous flow of the numerical model. The forces extracted from the inviscid panel model are presented by the blue line in Figures 4.5 & C.2, and by the cyan line in Figure 4.7. Those are used as a reference for the robustness check of the Noca method.

There are five mean different possibilities for uncertainties to occur when using the method:

- The choice of the contour.
- The averaging of the velocity fields could lead toerrors.
- The interpolation over the masked regions is done incorrectly.
- A window shift during stitching gives bad results.
- The time-term loads in the Noca method gives errors.

All of the following sources will be elaborated on in this section.

4.5.1 Different contours

Due to imperfections and unregularities in the flow field, it is possible that different contours will give different load results. Although in theory all the different contours should give the same result (as long as the blade is entirely in the contour), the reality is different. To compensate, multiple contours are evaluated on each velocity field. The mean and deviation are calculated with the results, and presented in the graphs in Chapter 5 by a circle and a line accordingly.

To get an idea of the contours, the contours for the azimuthal angle ($\theta = 0°$) are plotted in Figure 4.5, with a close-up of the contours in Figure 4.6. Here the different contours are

taken on the velocity fields from the panel code. The contours are calculated with Equation 4.6, where $k = 1, 2, ...12$ for the contours, and X_{circ}, Y_{circ} are the non-dimensionless coordinates of a circle. The coordinate system is rotated to be the same as the coordinate system of the experiment: $\theta_{rot} = (90 + \theta) \cdot \pi/180;$. The contours are visualised in Figure 4.4.

$$\begin{aligned} X_{Elps} &= \cos(X_{circ}) \cdot 0.0905 \cdot ((k \cdot 0.01) + 1) + R; \\ Y_{Elps} &= \sin(Y_{circ}) \cdot 0.1524 \cdot ((k \cdot 0.01) + 1) - 0.019; \\ X_{Cont} &= cos(\theta_{rot}) \cdot X_{Elps} - sin(\theta_{rot}) \cdot Y_{Elps}; \\ Y_{Cont} &= sin(\theta_{rot}) \cdot X_{Elps} + cos(\theta_{rot}) \cdot Y_{Elps}; \end{aligned} \tag{4.6}$$

In Figure 4.5 (green colour) two contours have forces much larger than the actual force on the blade. This is probably because the contours are crossing a vortex blob, and will give extreme loads. If these out-layers would be removed, it can be said that in average the contours are predicting the actual load accurately.

4.5.2 Averaging of the velocity fields

PIV will provide a static image of the velocity field that is in reality fluctuating over time. However, one speaks of a fluctuation around a given field instead. By averaging, these fields can be obtained. Since in this case the panel code gave us the absolute velocity fields, it was modified in order to get the same averaged flow field as for the experiments. From an original inviscid panel model flow field, 200 fields with a random X and Y offset between -1 and 1% chord length were created. These fields were averaged, and the top right figure in Figure 4.4 was created. As seen, the vortex blobs that were obvious in the original image, are now somewhat vanished. Also, directly at the blade the maximum velocities have become lower. These are typical results that could have been expected due to averaging.

Interesting to investigate, is what the Noca method will output for the loads. In Figure 4.5 (red line) the results are shown, still taking into account different contours to compensate for any local imperfections. It can be seen that due to the averaging, an offset of the actual force is created. Also, in this case the peaks that were in the original image for contours 2 and 3 have now vanished due to the averaged flow field.

It can be said that averaging creates an offset from the actual load, and that it will mask interesting physical activities in the single images. The offset created with the averaging however is small, and can be neglected for our purposes.

From this point forward, all the possible uncertainties that might occur in the velocity fields will be also tested on the averaged field.

4.5.3 Interpolation over masked areas

When choosing a contour for the evaluation of the forces according to Noca et al. [28], it could be that due to impurities in the velocity field (shadow, blind spot, bad processing)

there is a blind area in the velocity field. These areas are presented in Figures D.1 to D.15 by white areas. Over these areas, the velocities are interpolated. This interpolation can add an uncertainty in the force calculation.

To be sure this interpolation works correctly, the areas that were masked due to reflections and shadows in the experiment, are also masked in the original panel code field as well as in the created averaged fields, seen in Figure 4.4 middle left and right figures respectively.

The results are shown in Figure 4.5 (cyan line on original field, purple line on averaged field). The interpolation line follows the contour line nicely, which shows the linear interpolation scheme is working, and gives similar results. The purple line in Figure 4.5 represents the interpolation technique on the averaged fields, and this will be the method that is closest to the actual experiment. The results are very close to the results from the averaged results, again proving the interpolation is working well. The offset that was present for the averaged flow fields can still be seen in this case, although the offset is still relatively small.

4.5.4 Window shift simulating bad stitching

In Figure 4.5 (yellow line on original field, black line on averaged field) the loads can be seen for the difference when half of the velocity was shifted 1% chord length upwards in Y-direction. The shift is relatively small, and since all stitching is manually checked and corrected, the error in this shift can indeed be considered small.

Again the change in force is neglectable, and the average of all the contours is around the true value of the force. It is concluded that the load calculation model is robust against a small misalignment in stitching.

4.5.5 Uncertainty analysis on other azimuth angle

The same robustness checks were done for the 90° azimuth position, and can be seen in Appendix C. The same behaviour can be seen in this position, and the load calculation method by Noca et al [28] with a linear interpolation over the masked areas is proven valid for load determination on the experiment.

For this position, also the normal force (F_N) and the tangential force (F_T) are presented in Figure C.3. What can be seen from this figure, is that the order of magnitude in the difference between the reference force and the measured force by the method, is both in the order of ± 0.2[-]. Since the force in tangential direction is a lot lower than in normal direction, the sensitivity in the tangential direction will be a lot higher than in normal direction, and the challenge for capturing reliable experimental results for the tangential force will be difficult.

For further validation, the contours are also made larger on this field. In Figure C.5 the results can be seen. Comparing this to Figure C.3, not much difference can be observed, except for one value in the shifted field (cyan line). This is attributed to a possible vortex blob that is encountered, since the averaged field does not show the same trend.

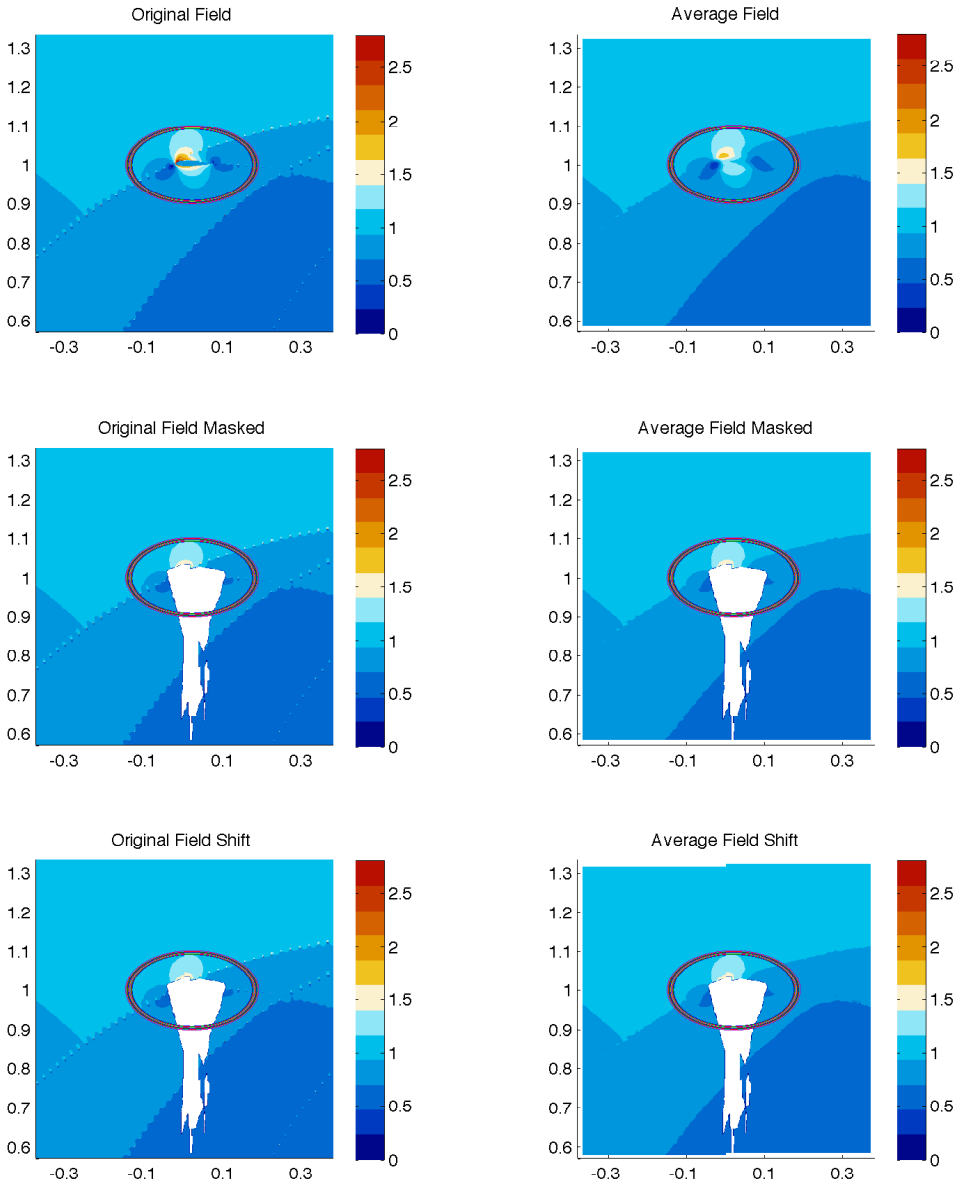

Figure 4.4: *Robustness check of the load calculation method at 0° azimuth position.*

4.5.6 Different reference systems

In order to check the errors in the time term of the load calculation method by Noca et al. [28], a new reference system was proposed. This reference system would move along with the blade direction. This way the time terms would mostly vanish, and only the inviscid terms remain. In order to check this method, both reference systems were tested

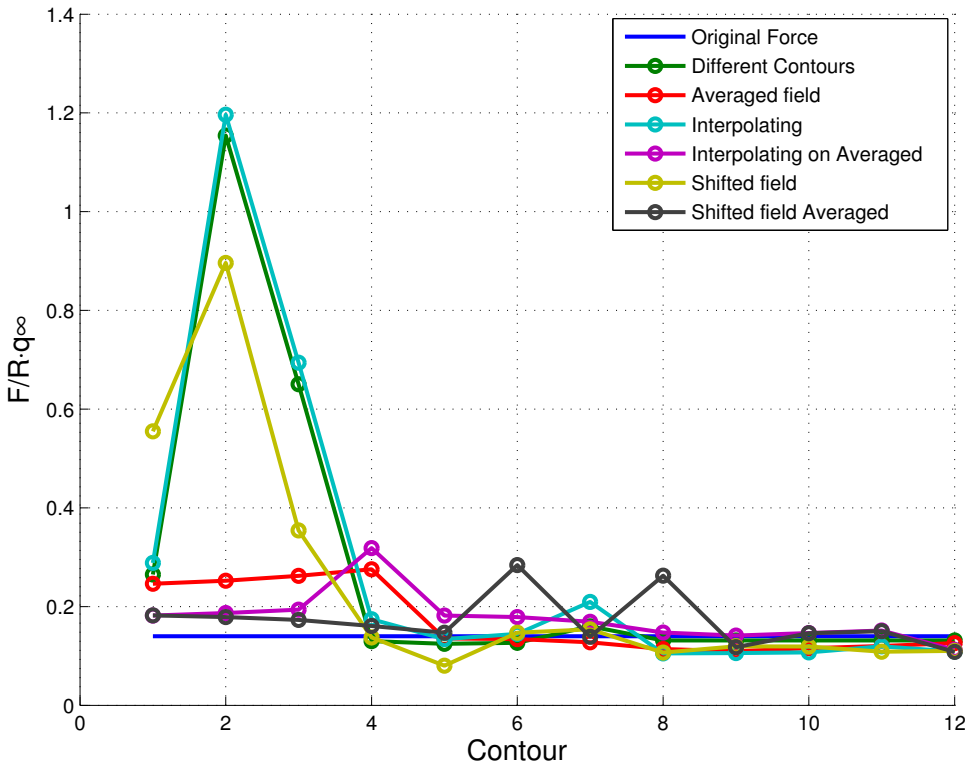

Figure 4.5: *The corresponding loads for the robustness check at 0° azimuth position.*

on the velocity fields gathered from the inviscid panel. The results can be seen in Figure 4.7.

It can be seen that for both reference systems, there is a good accordance with the actual force on the blade. Only at the 0° azimuth position there is a misalignment between the two frames. An explanation for this behaviour is that the loads are hard to be determined in this position because of multiple vortex blobs in the neighbourhood of the blade.

This means the method is higly unsteady on the time term. It is proposed both reference systems will be tested on the experimental data, to know the influence of the time term.

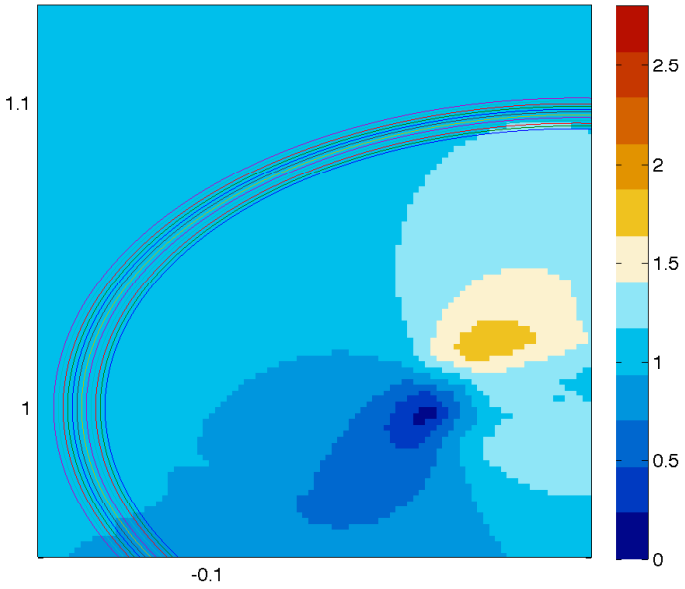

Figure 4.6: *A close-up of the different contours at 0° azimuth position.*

4.6 Preliminary conclusions

Some first conclusions from the uncertainty analysis are drawn. These conclusions will be used when presenting the experimental results.

The model imperfections are relatively high, and the pitch angle (1°) in the TSR 4.5 case must be considered when numerically approximating the experiment. A change in 1 degree can influence the normal forces on the turbine a lot.

The choice of the contour is of great importance when evaluating the loads on the blades. To minimise errors, the contours should cross as little masked fields as possible. Also, different contours will always give different loads. On the experimental data more contours must be evaluated, in order to correct for this trend, and to augment the certainty of the load.

The linear interpolation is working well over the masked areas. This interpolation scheme can be used on the experiments, but as mentioned before, these masked areas should be kept to a minimum to reduce the interpolation error.

The stitching error was observed to be very low, and can be neglected for this purpose. Although this can not be said for the reference systems. The loads at most azimuthal positions matched with both reference frames, it is still advised to verify both reference frames on the experiment.

The largest error occurs in the time term described in the method by Noca et al. [28]. This term is very sensitive to errors in the shift in position (dT). This number is influenced by the uncertainty in azimuthal position of the turbine. When the rotational velocity is fluctuating a lot, the azimuthal position becomes uncertain, and larger load variations in

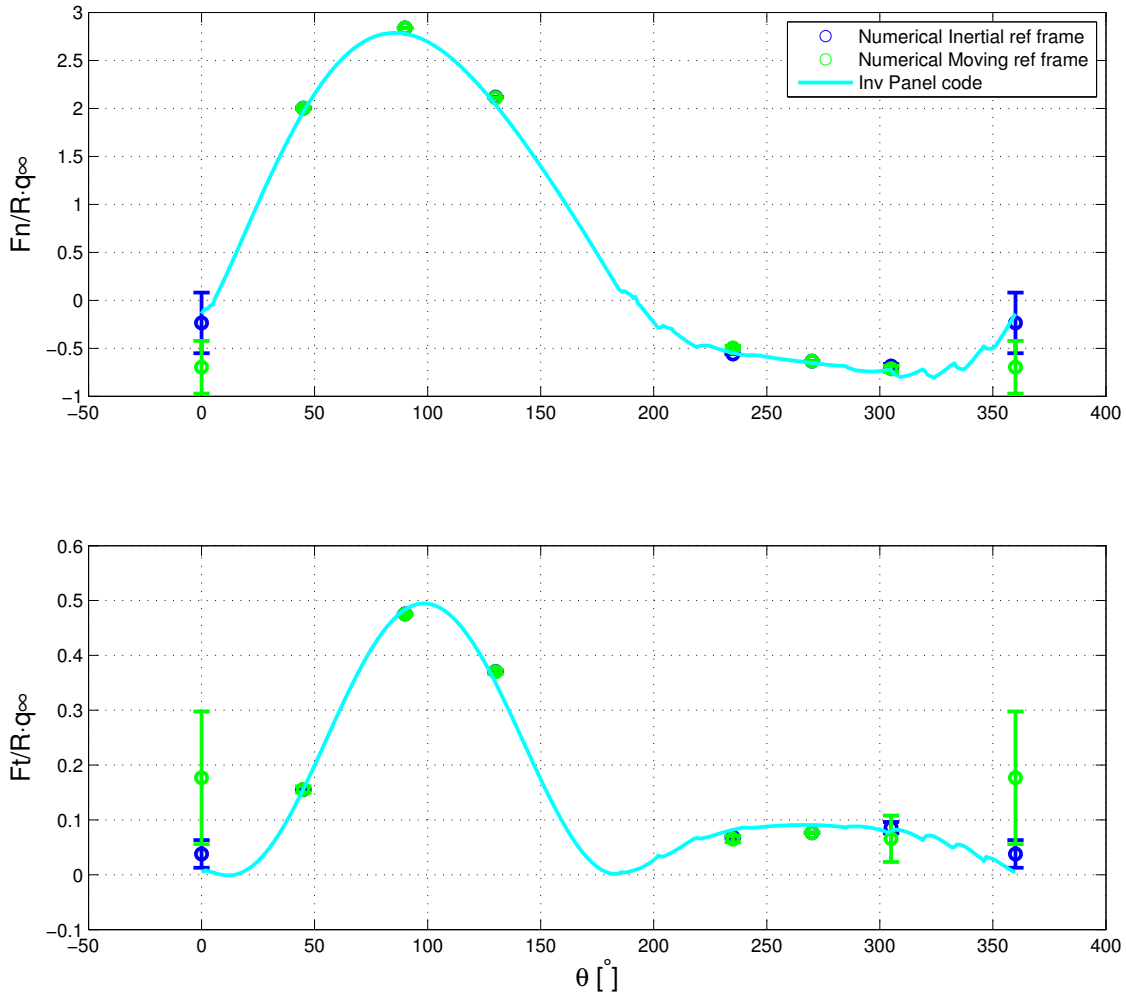

Figure 4.7: *Loads for the method calculated on different reference frames.*

the Noca method occur. Due to the instability of the rotational velocity, especially in TSR 4.5 case, tangential forces will be very hard to capture during this experiment. The time term, together with the variation in the rotational velocity, will pose the biggest challenge in terms of uncertainty.

CHAPTER 5

RESULTS & DISCUSSION

In this chapter the results are presented. In Section 5.1 the results from the experiment are shown. This includes the velocity fields and the loads according to those fields.

The numerical models elaborated in Section 2.5 are compared to the experimental results in Section 5.2. This gives an insight on how the different models predict the loads on the turbine in TSRs of 4.5 and 2.

This chapter will conclude the last phase of Figure 1.2, the modelling phase (phase 3). This will lead to the opportunity to give some conclusions and recommendations about this work in Chapter 6.

5.1 Experimental results

5.1.1 Velocity fields

In Figure 5.1 and 5.2 the velocity fields of the experiment for TSR 4.5 and 2 respectively, can be seen. In the velocity field figures, the velocities are non-dimensionalised by the free stream velocity ($\frac{V}{V_\infty}$). The coordinates are non-dimensionalised with the radius ($[\frac{X}{|R|}\ \frac{Y}{|R|}]$), and the forces by $q_\infty \cdot R$ ($\frac{F}{\frac{1}{2}\rho V_\infty^2 \cdot R}$) in order to compare different solidities (due to compensation for inviscosity).

For both TSR it can be seen that the turbine is slowing down the stream. The velocities downwind are much lower than the velocities upwind, which proves that energy is extracted from the flow.

In the windward position (close-up in Figure D.1) the wake from the previous blade, as well as from 2 passages before, can be seen in this field. Comparing this to the panel code field the experimental and numerical simulations present a similar wake convection.

A close-up from the most upwind positions for the experiment and the inviscid panel model are also given for TSR 4.5 in Figure D.3. The close-up of this position for TSR 2 is given in Figure D.10 where the blade is clearly in stall.

The downwind positions in Figure D.6 and Figure D.14 clearly show the wake interaction from the mast with the blade, whereas for the inviscid panel model in Figure D.6 this is not seen, since the mast is not modelled.

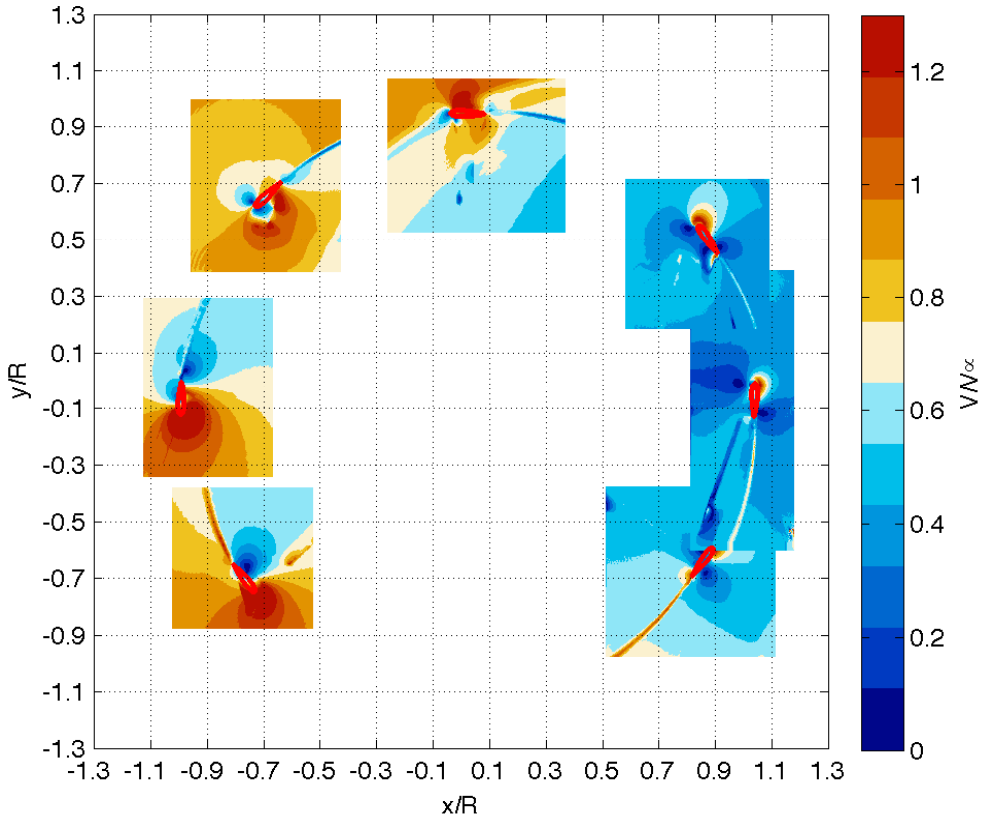

Figure 5.1: *Experimental velocity fields for TSR 4.5.*

5.1.2 Forces

The forces resulting from the experiment are seen by the black and red dots in Figures 5.3 & 5.4, black being the fixed and red the moving reference frame respectively. The dots represent the average from the 12 integration contours that were taken around the blade. The line is the deviation from this averaged value.

TSR 4.5 (Figure 5.3):

As was explained in Section 4.3, the error on the rotational velocity for this TSR of 4.5 was quite high. The time term in the Noca et al. integration approach was very sensitive to this error, and resulted in a fluctuating force along different contours. In Figure 5.3 the forces can be seen for the TSR 4.5. In Appendix E a table with the data is also provided.

A good comparison between the two reference frames can be seen in the normal force direction, except for the 130° azimuth position. Here the blade was moving a lot during the experiment, and no good load extraction was possible for this position.

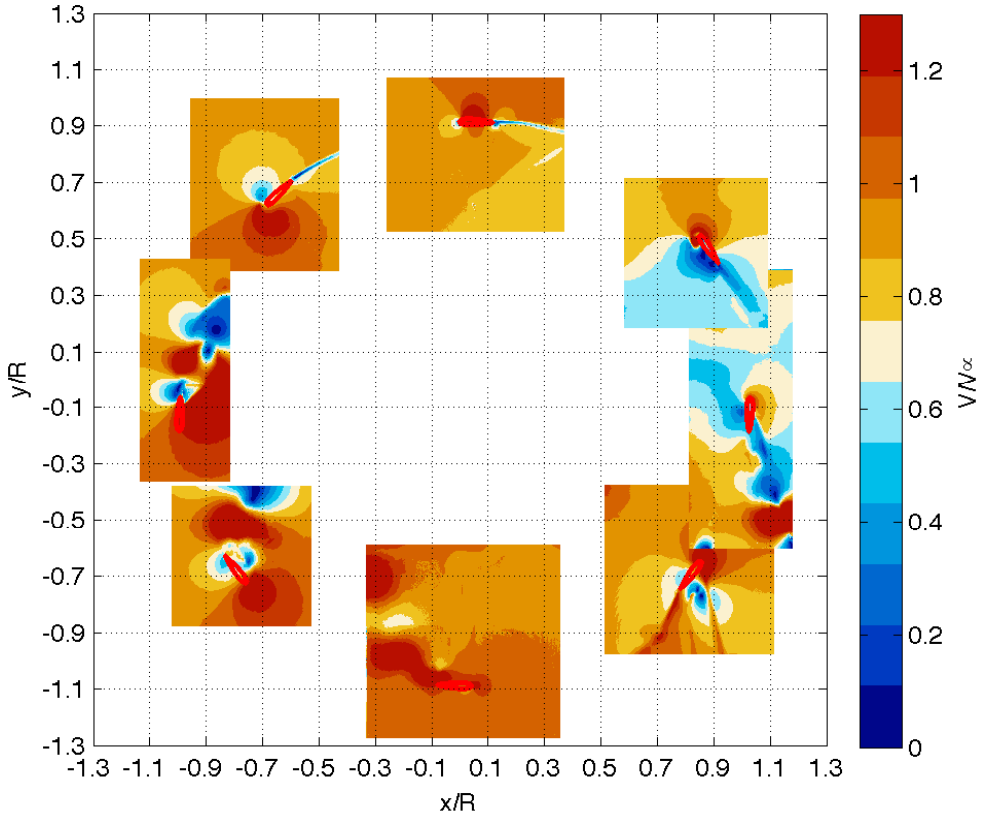

Figure 5.2: *Experimental velocity fields TSR 2.*

The tangential forces are most sensitive in terms of fluctuation in force due to the error. The reason is that these forces are relatively small compared to the total force acting on the blade. Due to all the perturbation (see Section 4.3), these forces can not be considered valid for any comparison, as can also be seen from the difference in force between the two reference frames.

Overall, the uncertainty can be said to be low for the normal force, and the normal force can be used for comparisons (except the 130° azimuth position). Due to the perturbations in rotational speed, the tangential force is to uncertain and cannot be used for any comparisons.

TSR 2 (Figure 5.4):

The experiment and the rotational velocity were steady during the measurements of the TSR 2. This makes the confidence level of the results higher. On the other hand, when the blade is in deep stall and the vorticity in the field is high, the uncertainty of the load calculation method will increase. The flow fields are varying a lot in these positions, and large fluctuations in force can be noticed.

In Figure 5.4 the forces can be seen for TSR 2. In Appendix E a table with the data is again provided. In the normal force direction, the different reference frames are showing

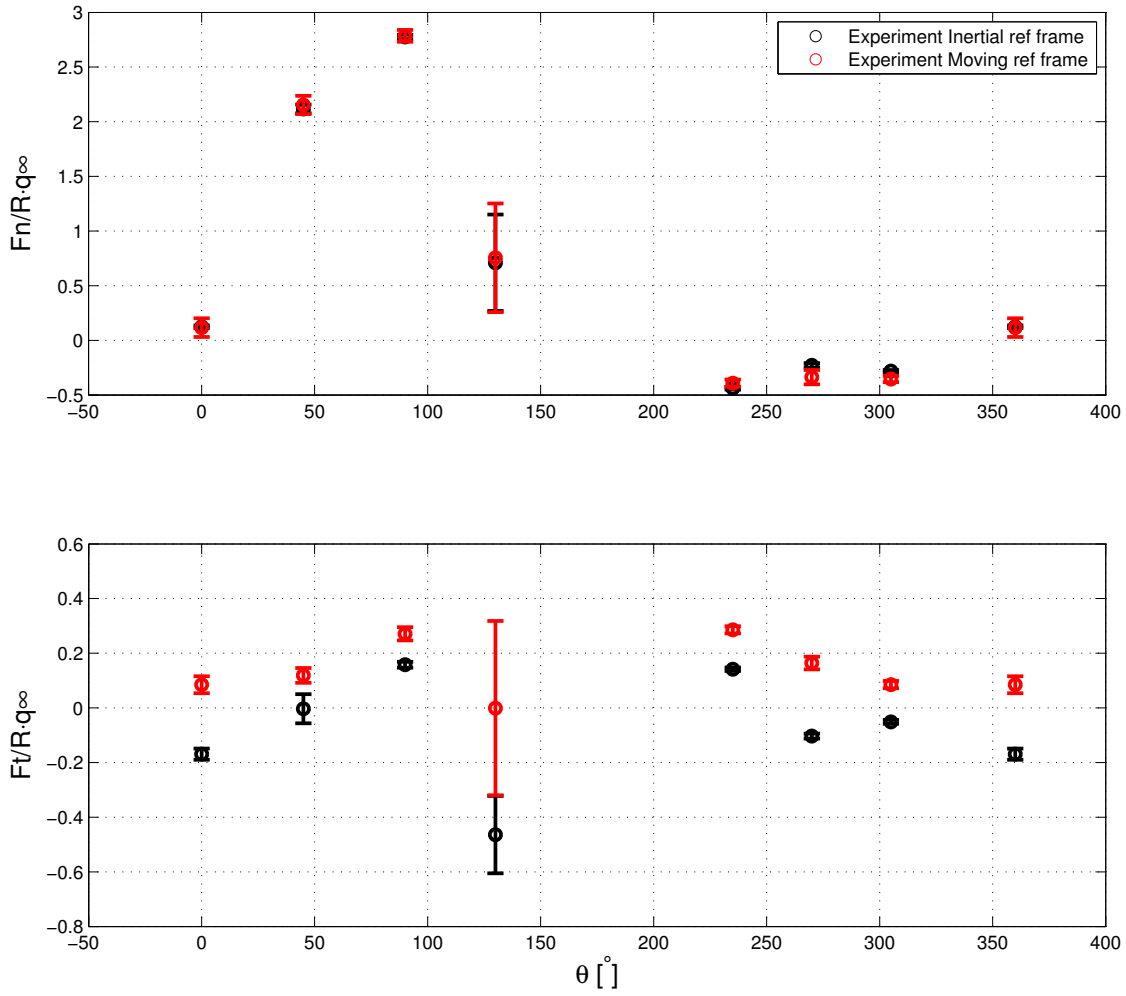

Figure 5.3: *The difference between the forces on all the azimuthal positions for TSR 4.5.*

comparable results. Only for the 90° position the loads of the tangential force are uncertain. The blade is fully in stall at this position, and the method is not able to predict this load correctly. All loads are comparable, except in the 90° azimuth position tangential force, which will be discarded for comparisons.

5.2 Comparisons experiment with numerical models

With the experimental results from both TSRs, a comparison is made with different numerical models in this section.

5.2.1 TSR 4.5

In Figure 5.5 the comparisons for TSR 4.5 can be seen. In the normal direction, the inviscid panel model and the double wake panel model are comparing best to the experimental results. The lifting line model is also following the trend of the force, but has an offset

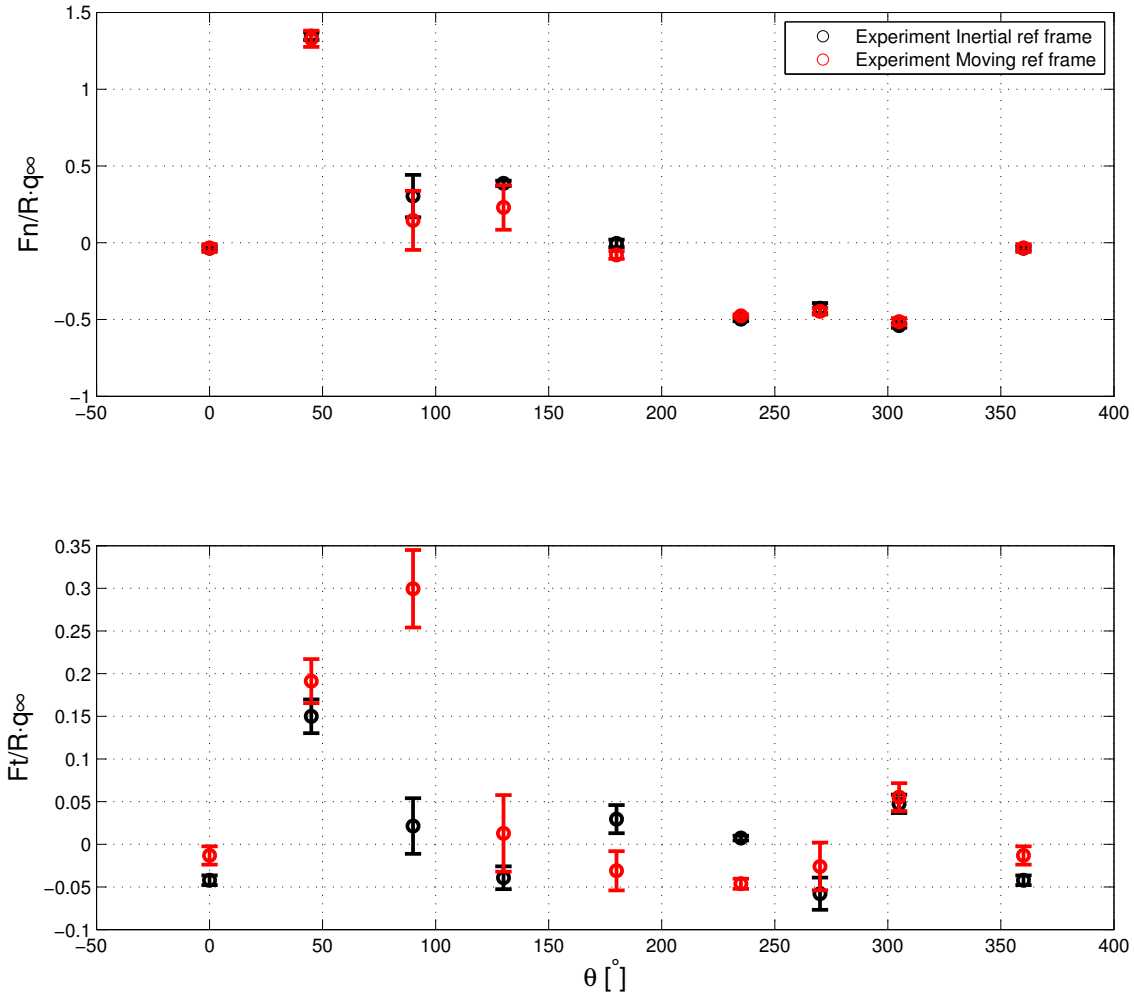

Figure 5.4: *The difference between the forces on all the azimuthal positions for TSR 2.*

with reference to the experiment. The BEM model is following the trend quite nicely in the upwind region, but is far off in the downwind area. This is because of the poor modelling of the physics in those regions. An overestimation of the AoA in the downwind is the cause of this big difference.

The experimental tangential forces are not comparable to the numerical results, although it can be said that both panel models follow the same trend as can be seen in the experimental results. The lifting line model and the double wake panel model have approximately the same results, whereas the inviscid panel code force is higher in the upwind region. This could be expected because of the inviscosity of the model. The BEM model is predicting to high forces everywhere. It can be said this model poorly estimates the tangential forces for this TSR.

5.2.2 TSR 2

In the TSR 2 case the inviscid panel model is not modelled anymore. The results will be unreliable since dynamic stall is a viscous phenomenon. All other models are able to

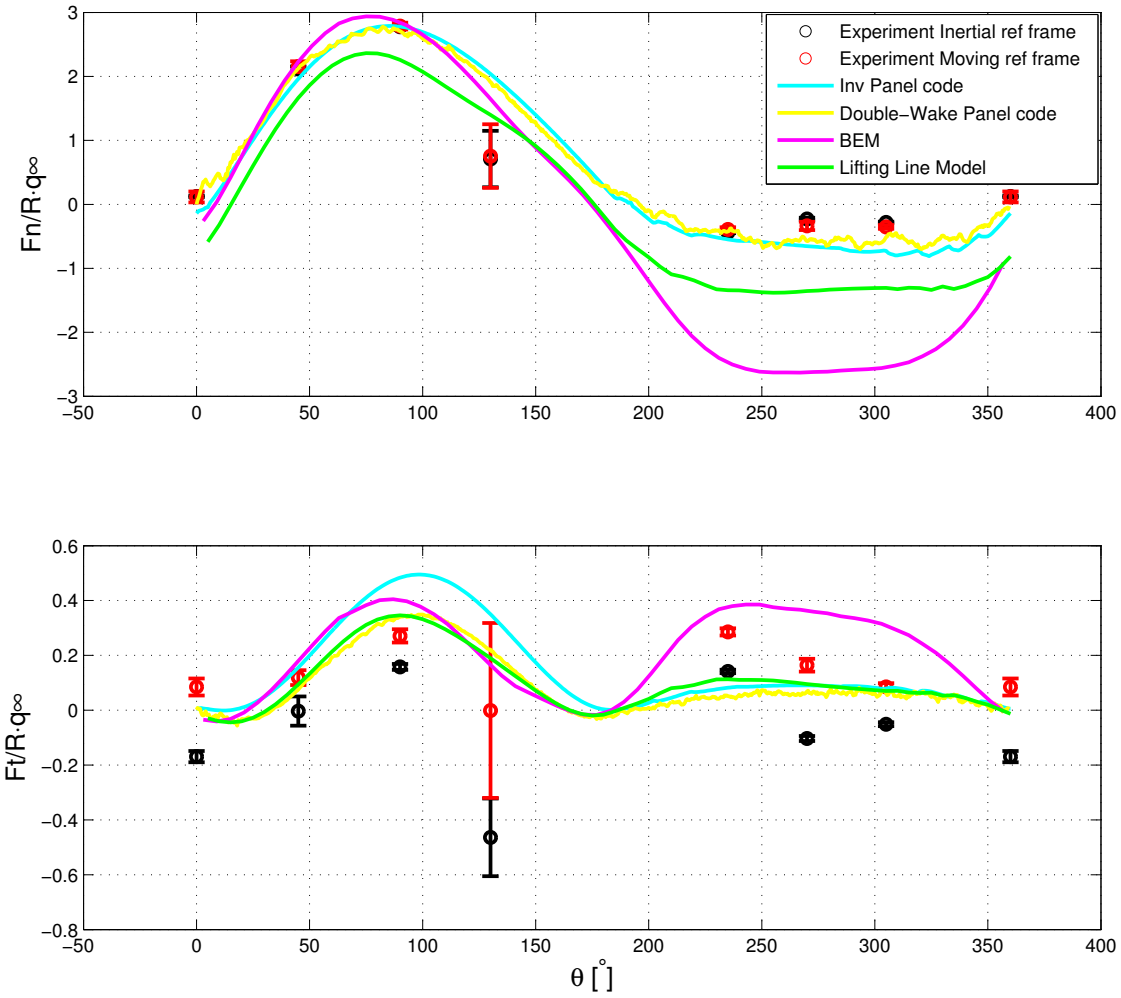

Figure 5.5: *The difference between different models and the experiment for TSR 4.5.*

capture the loads because of their ability to model (dynamic) stall.

In Figure 5.6 the results from all models are compared to the experimental loads. An overall observation is that the loads of the models are very different. Big AoA changes, big force fluctuations, and difficult vortex blade interaction make it hard to model this situation.

From the figure it can be said the double wake panel code is predicting the forces best. A clear drop in normal force around an azimuth $\theta = 90°$ can be seen, where in the velocity fields it was obvious the blade was in full stall. Also in the tangential direction most experimental forces coincide with the prediction of the double wake panel model.

The lifting line model is very conservative in predicting the forces. This is probably because of the Øye dynamic stall model. This model is relatively simple, and can not predict fast and difficult variations. Despite of this, the forces are not that far off compared to the experimental results. It can be said that this model is predicting forces relatively well, seen the simplicity of the model compared to the double wake panel model.

The BEM model is doing a relatively good job in the normal force direction, and in the

upwind region of the tangential forces. The reason for this accordance is the Beddoes Leishman dynamic stall model with which it was modelled. In the downwind region of the tangential force the model shows large fluctuations and is not comparable to the force of the experiment at all. This is believed to be due to the inability of the wake modulation. The BEM will predict to large forces in the downwind region due to this error. It can be said the prediction of the BEM model is unsatisfactory in this region.

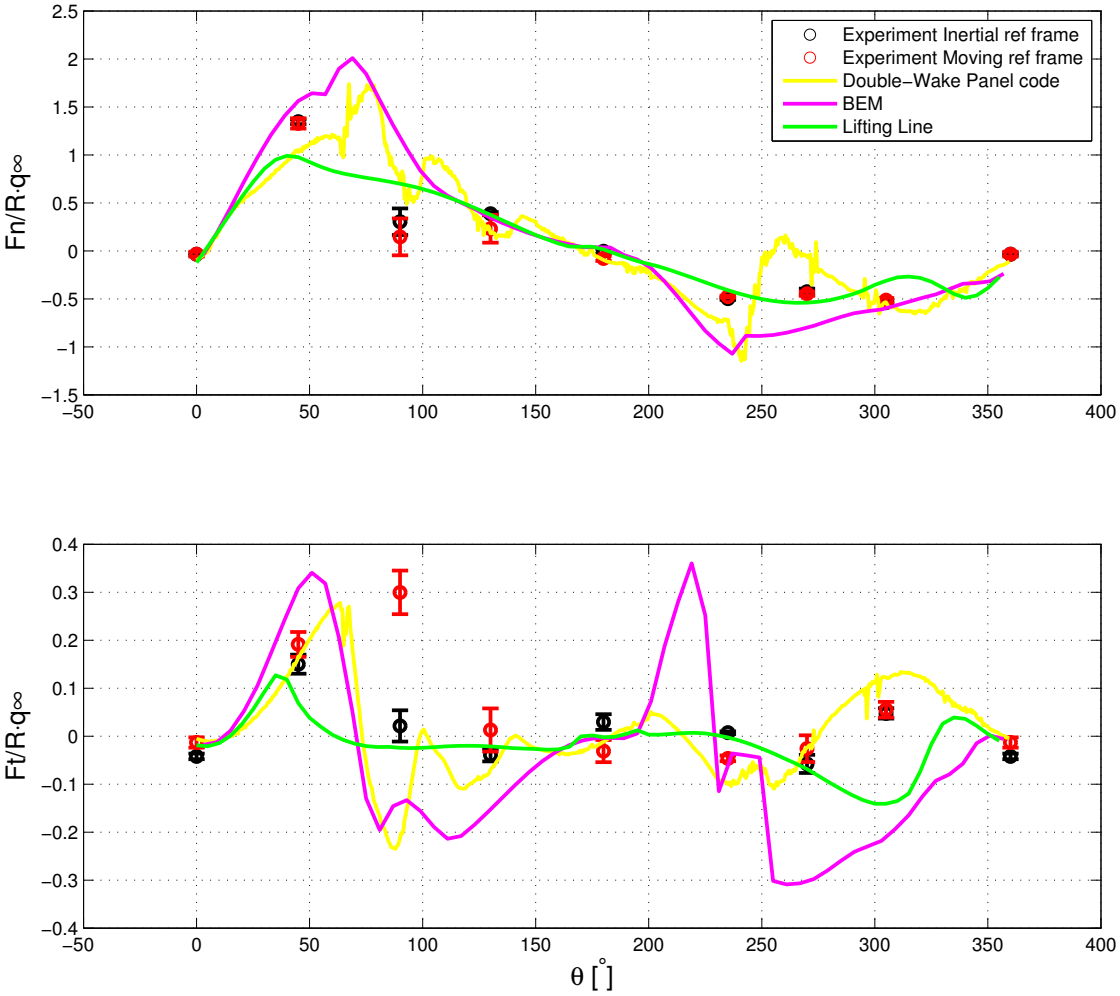

Figure 5.6: *The difference between different models and the experiment for TSR 2.*

CHAPTER 6

CONCLUSIONS & RECOMMENDATIONS

Conclusions

Velocity fields were presented for TSR of 4.5 and 2 at eight azimuthal positions. The normal force on the blades for TSR 4.5, extracted with the method described by Noca et al. [28], are following the trend that is expected from loads on VAWTs. The results for both tip speed ratio are reasonable and the approach followed in this paper is feasible.

The rotational velocity during the experiments of the TSR 4.5, was very unsteady ($\Delta\omega \approx 2\%$). The variation on the rotational velocity has a direct influence on the loads resulting from the time-term in the method described by Noca et al. This resulted in a load fluctuation in the time term, which caused an unsteady measurement in the tangential direction. In the TSR 2 case, the variation in rotational velocity was much lower (approximatly 0.15%). The resulting uncertainty in the loads was therefore only ± 0.1[-], and the tangential forces can still be used for comparisons in this case.

This large fluctuation in the forces resulted in discarding all tangential forces for comparisons of the TSR 4.5 case. The loads were all already relatively low (ranging from-0.2 to 0.4). The uncertainty fluctuation has a too big influence on this force magnitude, and the mean will be too much influenced by the uncertainty. At the azimuth $\theta = 130^\circ$ the uncertainty was so high, even the normal force had to be disregarded for this position.

In the TSR 2 case, both the normal and tangential forces are used for comparisons. At 90° large fluctuations and an offset with the models was observed. The load determination method is unreliable at this position, since the blade is in deep stall. The momentum was not conserved, what creates large variations on the loads for the different contours, resulting in an error on the mean load value. This azimuth position can not be used for comparisons in tangential direction.

For the TSR 4.5 case no dynamic stall was observed, and the inviscid panel code developed by Simão et al. [43] was able to predict the forces in normal direction accurately. The tangential direction could not by compared due to the important role of viscosity in this direction. The BEM model was over predicting forces in this TSR for the entire cycle

in the normal force direction, and for the downwind area in tangential direction. The lifting-line on the other hand was under predicting all the normal forces. This model did not take curvature effects into account. It did predict the tangential loads very accurately, comparable to the tangential forces of the double wake panel model. The double wake panel model was the most accurate model. In normal direction the difference with the experiment is never larger than 1%.

Good comparisons between the lifting line model and the double wake panel model with the experimental results were found, in the TSR 2 case. The lifting line model was predicting low forces, and not giving any fluctuations at all, although it mostly did match the experimental results. The implemented Øye dynamic stall model was unable to predict the difficult fluctuations happening due to dynamic stall. A good accordance between the double wake panel model and the experimental results were found. A drop in normal force at the 90° position shows the capability of the model to predict the loss in load due to dynamic stall. The BEM model performed unsatisfactory in this TSR case.

Recommendations

Future research should focus on developing a VAWT model which is capable of keeping a low uncertainty in rotational velocity at all TSRs. In order to calculate the loads on the blades, it is of great importance that the experiment is conducted with minimal uncertainty, especially in the rotational velocity and the azimuthal position of the blade. Also, a model should be built that has the ability to run at higher RE-numbers; more test in different domains will be able to be experimentally tested.

This experiment should be repeated with an asymmetric blade profile. No experimental data is yet available on VAWTs with an asymmetric profile in dynamic stall.

During experiments more pictures of the set-up and the experimental process should be taken for later reference. Those pictures can be useful in reporting afterwards, or for a double check at a later time.

More research should be done on the blockage effect of the rotor in the OJF. Although the uncertainty and the blockage is assumed negligible, there is no solid research to prove this statement in the OJF.

Random errors should be added to the (numerical) flow fields in order to check the robustness of the load calculation method to these fluctuations. This should make the certainty of the approach even higher, and will give the certainty of this method being used for future research without any doubts.

A comparison with a CFD analysis should be done in order to compare all experimental data and all models with these results. More insight in the difference between all models can be gained.

REFERENCES

[1] Anderson, J.D., Jr. *Fundamentals of Aerodynamics*, volume Fourth Edition. Mc. Fraw Hill, 2007.

[2] Battisti, L., Zanne, L., Dell'Anna, S., Dossena, V., Persico, G., Paradiso, B. Aerodynamic measurementson a vertical axis wind turbinein a large scale wind tunnel. *Journal of Energy resources Technology*, 133, 2011. doi: DOI:10.1115/1.4004360.

[3] Beddoes, T. S. A third generation model for unsteady aerodynamics and dynamics stall. *Westland Helicopter Limited*, RP-908, 1993.

[4] Berdowski, T. Investigation of dynamic stall and performance models with emphasis on vawt-design. Master's thesis, DTU, 2014.

[5] Brochier,G., Fraunie, P., Beguier, C. and Paraschivoiu, I. Water channel experiments of dynamic stall on darrieus wind turbine blades. *ournal of Propulsion*, 1986.

[6] Claessens, M. *The design and testing of airfoils for application in small vertical axis wind turbines.* PhD thesis, TUDelft, 2006.

[7] Crimi, P. Dynamic stall. *AGARDograph*, (172), 1973. ISSN 03652467.

[8] Dantec Dynamics. Safex fog generators. https://www.dantecdynamics.com/safex-fog-generators, March 2014.

[9] Dixon, K. *The near wake structure of a vertical axis wind turbine - including the development of a 3D unsteady free-wake panel method for VAWTs.* PhD thesis, TUDelft, 2008.

[10] Drela, M. Xfoil: An analysis and design system for low reynolds number airfoils. In *Low Reynolds Number Aerodynamics*, 1989.

[11] Fujisawa, N. and Shibuya, S. Observations of dynamic stall on darrieus wind turbine blades. *Journal of Wind Engineering and Industrial Aerodynamics*, 2001.

[12] Fujisawa, N. and Takeuchi, Y. Flow visualization and piv measurement of flow field around a darrieus rotor in dynamic stall. *Journal of Visualization*, 1999.

[13] Glauert, H. Elements of aerofoil and airscrew theory. *Elements of Aerofoil and Airscrew Theory*, (2), 1947.

[14] Heinz, J., Bergami, L. and Gaunaa, M. Indicial lift response function: An empirical relation for finite-thickness airfoils, and effects on aeroelastic simulations. *Wind Energy*, pages –, 2012. ISSN 10954244, 10991824. doi: 10.1002/we.1516.

[15] Islam, M., Ting, D.S.K. and Fartaj, A. Desiderable airfoil features for smaller-capacity straight-bladed vawt.

[16] Jones, R.T. Dynamic stall - simulated as time lag of separation. *Technical Report, Department of Fluid Mechanics, Technical University of Denmark*, 1991.

[17] Kinzel, M., Mulligan, Q. and Dabiri, J.O. Energy exchange in an array of vertical axis wind turbines. *Journal of Turbulence*, pages 13:1–13, 2012.

[18] Laneville, A. and Vittecoq, P. Dynamic stall - the case of the vertical axis wind turbine. *Journal of Solar Energy Engineering*, 1986.

[19] Larsen, J. W., Nielsen, S. R. K. and Krenk, S. Dynamic stall model for wind turbine airfoils. *Journal of Fluids and Structures*, 23(7):959–982, 2007. ISSN 08899746, 10958622. doi: 10.1016/jjfluidstructs.2007.02.005.

[20] LaVision. Piv camera's. http://www.lavision.de/en/products/cameras/piv_cameras.php.

[21] LaVision. Davis, software for intelligent imaging. www.lavision.de/en/products/davis.php, April 2014.

[22] Lignarolo, L.E.M., Ragni, D., Krishnaswami, C., Chen, Q., Simão Ferreira, C.J. and van Bussel, G.J.W. Experimental analysis of the wake of a horizontal-axis wind-turbine model. Technical report, Delft University of Technology, Wind Energy, Delft, 2013.

[23] Mccroskey, W. J. The phenomenon of dynamic stall. *Other Sources*, 1981.

[24] Mulder, A., van Staveren, W.H.J.J., van der Vaart, J.C., de Weerdt, E., in 't Veld, A.C. and Mooij, E. Flight dynamics. Lecture notes, TUDelft, 2011.

[25] Nakano, T., Fujisawa, N., Oguma, Y., Takagi, Y. and Lee, S. Experimental study on flow and noise characteristics of naca0018 airfoil. Technical report, Department of Mechanical Engineering, Niigata University, 2006.

[26] Nenuphar. Nenuphar offshore wind tubrines. http://www.nenuphar-wind.com/en, October 2014.

[27] Noca, F. *On the evaluation of time-dependent fluid-dynamic forces on bluff bodies.* PhD thesis, California Institute of Technology, 1997.

[28] Noca, F. , Shields, D. and Jeon, D. A comparison of methods for evaluating time-dependent fluid dynamic forces on bodies, using only velocity felds and their derivatives. *Journal of Fluids and Structures*, 1999.

[29] Paraschivoiu, I. *Wind turbine design: with emphasis on Darrieus concept.* . Polytechnic International Press, Montreal, 2002.

[30] Paraschivoiu, I. *Wind Turbine Design: With Emphasis on Darrieus Concept*. 2002.

[31] Peace, S. . Another approach to wind. *Mechanical engineering*, pages 126(6):28–31, 2004.

[32] Pereira, R., Schepers, G. and Pavel, M. D. Validation of the beddoes-leishman dynamic stall model for horizontal axis wind turbines using mexico data. 2011.

[33] Raffel, M., Willert, C.E., Wereley, S.T., Kompenhans, J. *Particle Image Velocimetry*. Cambridge Aerospace Series. Springer, Cambridge, 2007. ISBN 0-521-52396-6.

[34] Research Group Aerodynamics. Wind tunnel wall corrections for the Open Jet Facility. http://www.lr.tudelft.nl/en/organisation/departments/aerodynamics-wind-energy-flight-performance-and-propulsion/wind-energy/education/master-projects/proposed-masters-projects/nt5/wind-tunnel-wall-corrections-for-the-open-jet-facility/.

[35] Research Group Aerodynamics. Open Jet Facility. http://www.lr.tudelft.nl/en/organisation/departments/aerodynamics-wind-energy-flight-performance-and-propulsion/wind-tunnel-laboratories/low-speed-tunnels/open-jet-facility/, March 2014.

[36] Research Group Aerodynamics. Open Jet Facility. http://www.lr.tudelft.nl/, March 2014.

[37] Riziotis, V.A., Voutsinas, S.G. Dynamic stall modelling on airfoils based on strong viscous–inviscid interaction coupling. *Journal for numerical methods in fluids*, 2007. doi: 10.1002/fld.1525.

[38] Ross, I. and Altman, A. Wind tunnel blockage corrections: Review and application to savonius vertical-axis wind turbines. Technical report, Mechanical and Aerospace Engineering, University of Dayton, 2011.

[39] Ross, I.J. Wind Tunnel Blockage Corrections: An application to Vertical-Axis Wind Turbines. Msc. Thesis, School of Engineering of the University of Dayton, Dayton, Ohio, 2010.

[40] Sheldahl, R.E. and Klimas, P.C. Aerodynamic Characteristics of Seven Symmetrical Airfoil Sections Through 180-Degree Angle of Attack for Use in Aerodynamic Analysis of Vertical Axis Wind Turbines. Technical report, Sandia National Laboratories, 1981.

[41] Sheng, Galbraith, Coton. A modified dynamic stall model for low mach numbers. *Journal of Solar Energy Engineering*, 130(3):031013–1–10, 2008. ISSN 01996231, 15288986.

[42] Simão Ferreira, C. J. , Barone, M., Zanon, A., Kemp, R. and Giannattasio, P. Airfoil optimization for stall regulated vertical axis wind tubrines. 2015. doi: 10.2514/6.2015-0722.

[43] Simão Ferreira, C.J. *The near wake of the VAWT - 2d and 3d views on the VAWT aerodynamics*. PhD thesis, TUDelft, 2009.

[44] Simão Ferreira, C.J., Bijl, H., van Bussel, G.J.W. and van Kuik, G.A.M. Simulating dynamic stall in a 2d vawt: Modeling strategy, verification and validation with particle image velocimetry data. *Journal of Physics*, 2007.

[45] Simão Ferreira, C.J., van Bussel, G.J.W., van Kuik, G.A.M. and Scarano, F. On the use of velocity data for load estimation of a vawt in dynamic stall. *Journal of Solar Energy Engineering*, 133(1):011006, 2011.

[46] Simão Ferreira, C.J., van Kuik, G.A.M., van Bussel, G.J.W. and Scarano, F. Visualization by piv of dynamic stall on a vertical axis wind turbine. *Exp Fluids*, 2008.

[47] Snel and Schepers. Engineering models for dynamic inflow phenomena. *Journal of Wind Engineering and Industrial Aerodynamics*, 39(1-3):267–281, 1992. ISSN 01676105.

[48] Strickland, J. H. . A vortex model of the darrieus turbine: an analytical and experimental study. *Sandia Report*, SAND79-7058, 1980.

[49] Strickland, J. H. The darrieus turbine: a performance prediction model using multiple streamtube. *Sandia Laboratories Report*, SAND75-0431, 1975.

[50] Tescione, G., Ragni, D., He, C., Simão Ferreira, C.J. and van Bussel, G.J.W. Near Wake Flow Analysis of a Vertical Axis Wind Turbine by Stereoscopic Particle Image Velocimetry. Technical report, TUDelft, the Netherlands, 2013.

[51] Theodorsen, T. General theory of aerodynamic instability and the mechanism of flutter. *NACA Report*, 496, 1935.

[52] Thwaites, B. *Incompressible aerodynamics*. Clarendon Press, 1960.

[53] Timmer, W.A. Two-dimensional low-reynolds number wind tunnel results for airfoil naca 0018. Technical report, Wind Energy Section, Faculty of Aerospace Engineering, Delft University of Technology, 2008.

[54] van Oudheusden, B W. ,Scarano, F., Roosenboom, E. W.M., Casimiri, E.W.F. and Souverein, L. J. A comparison of methods for evaluating time-dependent fluid dynamic forces on bodies, using only velocity felds and their derivatives. Technical report, Graduate Aeronautical Laboratories, California Institute of Technology, 1999.

[55] van Oudheusden, B.W., Scarano, F., Roosenboom, E.W.M., Casimiri, E.W.F. and Souverein, L.J. Evaluation of Integral Forces and Pressure Fields from Planar Velocimetry Data for Incompressible and Compressible Flows. Technical report, TUDelft, the Netherlands, 2006.

[56] Vita, L., Paulsen, U.S. and Pedersen, T.F. A novel floating offshore wind turbine concept: New developments. *European Wind Energy Conference and Exhibition 2010*, pages 5:3952–3962, EWEC 2010.

[57] Wickens, R.H. Wind tunnel investigation of dynamic stall of an naca 0018 airfoil oscillating in pitch. Technical report, National Aeronauical Establishment, 1985.

[58] Zanon, A. *A vortex panel method for VAWT in Dynamic Stall*. PhD thesis, University of Udine, 2011.

[59] Zanon, A. , Giannattasio, P. and Simão Ferreira, C. A vortex panel model for the simulation of the wake flow past a vertical axis wind turbine in dynamic stall. *Wiley Online Library*, 2012. doi: 10.1002/we.1515.

APPENDIX A

TEST MATRIX

In this appendix the test matrix is presented. This test matrix is constructed during the experiments. All tunnel, turbine and PIV outputs are documented for all positions in this matrix.

Tip Speed Ratio = 4.5 _ VAWT_F14_TSR45_OLD

Basic Info				Absolute CoordSys*		Traverse CoordSys		Measurement Parameters				OJF			
No.	Name	Rec. Time	Sample	x	y	x	y	Azimuth	Ref. Time	Sep. Time	Acq. Rate	RPM	Speed	Pressure	Temperature
1	VAWT_F14_T4	2,01402E+11	150	-410	-100	90	-100	90	65,85	110	PL	231	9,12	1003,98	20,2
2	VAWT_F14_T4	2,01402E+11	150	-500	100	0	100	90	65,85	110	PL	231,8	9,13	1004,18	20,4
3	VAWT_F14_T4	2,01402E+11	150	-500	0	0	0	90	65,85	110	PL	231,8	9,15	1004,27	20,4
4	VAWT_F14_T4	2,01402E+11	150	-500	-100	0	-100	90	65,85	110	PL	213,8	9,14	1004,16	20,4
5	VAWT_F14_T4	2,01402E+11	150	-410	100	90	100	90	65,85	110	PL	231,7	9,13	1004,02	20,6

Tip Speed Ratio = 4.5 _ VAWT_F14_TSR45

Basic Info				Absolute CoordSys*		Traverse CoordSys		Measurement Parameters				OJF			
No.	Name	Rec. Time	Sample	x	y	x	y	Azimuth	Ref. Time	Sep. Time	Acq. Rate	RPM	Speed	Pressure	Temperature
1	VAWT_F14_	2,014E+11	150	-410	-100	90	-100	90	28,06	110	PL	231,7	9,09	1000,29	20,5
2	VAWT_F14_	2,014E+11	150	-500	100	0	100	90	28,06	110	PL	231,7	9,1	1000,47	20,5
3	VAWT_F14_	2,014E+11	150	-500	0	0	0	90	28,06	110	PL	231,8	9,12	1001,03	20,3
4	VAWT_F14_	2,014E+11	150	-500	-100	0	-100	90	28,06	110	PL	231,7	9,1	1000,64	20,4
5	VAWT_F14_	2,014E+11	150	-410	100	90	100	90	28,06	110	PL	231,7	9,1	1000,38	20,1
6	VAWT_F14_	2,014E+11	150	-410	-100	90	-100	89	27,85	110	PL	231,7	9,07	1000,2	20,1
7	VAWT_F14_	2,014E+11	150	-410	100	90	100	89	27,85	110	PL	231,7	9,08	1000,13	20,2
8	VAWT_F14_	2,014E+11	150	-500	100	0	100	89	27,85	110	PL	231,7	9,07	1000,01	20,3
9	VAWT_F14_	2,014E+11	150	-500	0	0	0	89	27,85	110	PL	231,7	9,06	999,88	20,3
10	VAWT_F14_	2,014E+11	150	-500	-100	0	-100	89	27,85	110	PL	231,7	9,06	999,88	20,3
11	VAWT_F14_	2,014E+11	150	-500	-100	0	-100	91	28,37	110	PL	232,8	9,1	999,55	20,3
12	VAWT_F14_	2,014E+11	150	-500	0	0	0	91	28,37	110	PL	232,8	9,09	999,5	20
13	VAWT_F14_	2,014E+11	150	-500	100	0	100	91	28,37	110	PL	232,8	9,09	999,36	20,2
14	VAWT_F14_	2,014E+11	150	-410	100	90	100	91	28,37	110	PL	232,8	9,08	999,22	20,3
15	VAWT_F14_	2,014E+11	150	-410	-100	90	-100	91	28,37	110	PL	232,8	9,09	999,13	20,3
16	VAWT_F14_	2,014E+11	150	-327	-353	173	-353	130	36,7	110	PL	232,8	9,08	998,86	19,6
17	VAWT_F14_	2,014E+11	150	-430	-200	70	-200	130	36,7	110	PL	232,8	9,07	998,45	20,1
18	VAWT_F14_	2,014E+11	150	-430	-375	70	-375	130	36,7	110	PL	233,9	9,09	998,17	20,2
19	VAWT_F14_	2,014E+11	150	-430	-375	70	-375	131	36,91	110	PL	235	9,1	996,28	19,7
20	VAWT_F14_	2,014E+11	150	-410	-220	90	-220	131	36,91	110	PL	235	9,08	996,05	19,5
21	VAWT_F14_	2,014E+11	150	-327	-353	173	-353	131	36,91	110	PL	235	9,09	996,02	19,7
22	VAWT_F14_	2,014E+11	150	-327	-353	173	-353	129	36,49	110	PL	235	9,08	995,73	19,8
23	VAWT_F14_	2,014E+11	150	-430	-200	70	-200	129	36,49	110	PL	235	9,08	995,5	19,7
24	VAWT_F14_	2,014E+11	150	-430	-375	70	-375	129	36,49	110	PL	235	9,07	995,33	19,8
25	VAWT_F14_	2,014E+11	150	-333	-220	167	-220	131	36,91	110	PL	234	9,06	992,97	20,4
26	VAWT_F14_	2,014E+11	150	-333	-220	167	-220	130	36,7	110	PL	234	9,06	992,98	20,4
27	VAWT_F14_	2,014E+11	150	-333	-220	167	-220	129	36,49	110	PL	235	9,08	993,16	20
28	VAWT_F14_	2,014E+11	150	-280	470	220	470	45	18,54	110	PL	233,8	9,1	1003,35	20,3
29	VAWT_F14_	2,014E+11	150	-390	470	110	470	45	18,54	110	PL	233,8	9,1	1003,35	20,3
30	VAWT_F14_	2,014E+11	150	-390	250	110	250	45	18,54	110	PL	233,8	9,1	1003,62	20,2
31	VAWT_F14_	2,014E+11	150	-260	320	240	320	45	18,54	110	PL	233,8	9,08	1003,65	20,2
32	VAWT_F14_	2,014E+11	150	-260	320	240	320	44	18,32	110	PL	235	9,08	1001,11	20,2
33	VAWT_F14_	2,014E+11	150	-260	320	240	320	46	18,75	110	PL	235	9,08	1001,99	20,4
34	VAWT_F14_	2,014E+11	150	-390	470	110	470	46	18,75	110	PL	235	9,07	1001,91	20,1
35	VAWT_F14_	2,014E+11	150	-390	470	110	470	44	18,32	110	PL	235	9,06	1001,91	20,5
36	VAWT_F14_	2,014E+11	150	-280	470	220	470	44	18,32	110	PL	236	9,09	1000,66	20,4
37	VAWT_F14_	2,014E+11	150	-280	470	220	470	46	18,75	110	PL	236,1	9,1	1000,5	20,5
38	VAWT_F14_	2,014E+11	150	-390	250	110	250	44	18,32	110	PL	236	9,08	1000,32	20,5
39	VAWT_F14_	2,014E+11	150	-390	250	110	250	46	18,75	110	PL	236	9,08	1000,4	20,1
40	VAWT_F14_	2,014E+11	250	25	489	525	489	0	8,92	110	PL	237	9,1	1000,09	20
41	VAWT_F14_	2,014E+11	250	25	489	525	489	1	9,14	110	PL	237	9,09	999,9	20,3
42	VAWT_F14_	2,014E+11	250	25	489	525	489	359	8,7	110	PL	237	9,07	999,67	20,2
43	VAWT_F14_	2,014E+11	250	-60	370	440	370	359	8,7	110	PL	237	9,07	999,38	20,1
44	VAWT_F14_	2,014E+11	250	-60	370	440	370	0	8,92	110	PL	237	9,07	999,11	20,2

Tip Speed Ratio = 4.5 _ VAWT_F14_TSR45_2

Basic Info				Absolute CoordSys*		Traverse CoordSys		Measurement Parameters				OJF			
No.	Name	Rec. Time	Sample	x	y	x	y	Azimuth	Ref. Time	Sep. Time	Acq. Rate	RPM	Speed	Pressure	Temperature
1	VAWT_F14_	2,014E+11	250	-60	370	440	370	1	9,14	110	PL	237	9,05	998,58	20,1
2	VAWT_F14_	2,014E+11	250	-60	489	440	489	1	9,14	110	PL	238	9,09	998,17	20
3	VAWT_F14_	2,014E+11	250	-60	489	440	489	0	8,92	110	PL	238	9,08	997,75	20,2
4	VAWT_F14_	2,014E+11	250	-60	489	440	489	359	8,7	110	PL	238	9,09	998,17	20
5	VAWT_F14_	2,014E+11	250	110	489	610	489	359	8,7	110	PL	238	9,07	997,29	20,2
6	VAWT_F14_	2,014E+11	250	110	489	610	489	0	8,92	110	PL	238	9,1	997,01	20,1
7	VAWT_F14_	2,014E+11	250	110	489	610	489	1	9,14	110	PL	238	9,1	996,81	20,1
8	VAWT_F14_	2,014E+11	250	100	370	600	370	1	9,14	110	PL	238	9,1	996,66	20,2
9	VAWT_F14_	2,014E+11	250	100	370	600	370	0	8,92	110	PL	239	9,09	996,55	20,2
10	VAWT_F14_	2,014E+11	250	100	370	600	370	359	8,7	110	PL	239	9,08	996,51	20,2
11	VAWT_F14_	2,014E+11	150	480	200	980	200	305	74,09	110	PL	240	9,11	995,09	19,9
12	VAWT_F14_	2,014E+11	150	480	200	980	200	304	73,88	110	PL	240	9,11	995,05	19,9
13	VAWT_F14_	2,014E+11	150	480	200	980	200	306	74,31	110	PL	240	9,11	994,94	19,9
14	VAWT_F14_	2,014E+11	150	360	200	860	200	306	74,31	110	PL	240	9,1	994,79	20
15	VAWT_F14_	2,014E+11	150	360	200	860	200	305	74,09	110	PL	240	9,1	994,79	19,9
16	VAWT_F14_	2,014E+11	150	360	200	860	200	304	73,88	110	PL	240	9,1	994,45	20
17	VAWT_F14_	2,014E+11	150	360	370	860	370	304	73,88	110	PL	240	9,09	994,45	20
18	VAWT_F14_	2,014E+11	150	360	370	860	370	305	74,09	110	PL	240	9,09	994,31	20
19	VAWT_F14_	2,014E+11	150	360	370	860	370	306	74,31	110	PL	240	9,08	994,08	20
20	VAWT_F14_	2,014E+11	150	480	370	980	370	306	74,31	110	PL	240	9,09	994,08	19,5
21	VAWT_F14_	2,014E+11	150	480	370	980	370	305	74,09	110	PL	240	9,09	994,08	19,5
22	VAWT_F14_	2,014E+11	150	480	370	980	370	304	73,88	110	PL	240	9,08	993,95	19,7
23	VAWT_F14_	2,014E+11	150	510	100	1010	100	269	66,4	110	PL	240	9,08	993,95	19,8
24	VAWT_F14_	2,014E+11	150	510	100	1010	100	270	66,62	110	PL	240	9,08	993,86	19,9
25	VAWT_F14_	2,014E+11	150	510	100	1010	100	271	66,83	110	PL	240	9,07	993,75	19,8
26	VAWT_F14_	2,014E+11	150	510	-110	1010	-110	271	66,83	110	PL	240	9,04	993,5	19,8
27	VAWT_F14_	2,014E+11	150	510	-110	1010	-110	270	66,62	110	PL	241,5	9,11	993,38	19,9
28	VAWT_F14_	2,014E+11	150	510	-110	1010	-110	269	66,4	110	PL	240	9,11	993,34	19,9
29	VAWT_F14_	2,014E+11	150	480	-200	980	-200	234	58,92	110	PL	241,5	9,1	993,22	19,5
30	VAWT_F14_	2,014E+11	150	480	-200	980	-200	235	59,14	110	PL	241,5	9,1	991,04	19,6
31	VAWT_F14_	2,014E+11	150	480	-200	980	-200	236	59,35	110	PL	241,5	9,1	992,92	19,7
32	VAWT_F14_	2,014E+11	150	360	-200	860	-200	236	59,35	110	PL	241,5	9,1	992,85	19,7
33	VAWT_F14_	2,014E+11	150	360	-200	860	-200	235	59,14	110	PL	241,5	9,1	992,8	19,8
34	VAWT_F14_	2,014E+11	150	360	-200	860	-200	234	58,92	110	PL	241,5	9,1	992,65	19,8

35	VAWT_F14_	2,014E+11	150	360	-370	860	-370	234	58,92	110 PL	236	9,1	1010,94	19,9
36	VAWT_F14_	2,014E+11	150	360	-370	860	-370	235	59,14	110 PL	236	9,11	1010,96	20
37	VAWT_F14_	2,014E+11	150	360	-370	860	-370	236	59,35	110 PL	236	9,1	1010,99	20,2
38	VAWT_F14_	2,014E+11	150	480	-370	980	-370	236	59,35	110 PL	236	9,09	1011,05	20,1
39	VAWT_F14_	2,014E+11	150	480	-370	980	-370	235	59,14	110 PL	236	9,09	1011,11	19,9
40	VAWT_F14_	2,014E+11	150	480	-370	980	-370	234	58,92	110 PL	222	9,11	992,86	19,5

Tip Speed Ratio = 2 _ VAWT_F14_TSR20

Basic Info				Absolute CoordSys*		Traverse CoordSys		Measurement Parameters				OJF			
No.	Name	Rec. Time	Sample	x	y	x	y	Azimuth	Ref. Time	Sep. Time	Acq. Rate	RPM	Speed	Pressure	Temperature
1	VAWT_F14_	2,014E+11	250	-475	140	25	140	90	80,38	80 PL		262,7	10,26	1011,74	20,2
2	VAWT_F14_	2,014E+11	250	-475	140	25	140	89	79,96	80 PL		262,8	10,25	1011,86	20,3
3	VAWT_F14_	2,014E+11	250	-475	140	25	140	91	80,8	80 PL		262,7	10,23	1011,98	20,3
4	VAWT_F14_	2,014E+11	250	-475	-100	25	-100	91	80,8	80 PL		262,7	10,24	1012,02	20,3
5	VAWT_F14_	2,014E+11	250	-475	-100	25	-100	90	80,38	80 PL		262,7	10,24	1012,1	20,3
6	VAWT_F14_	2,014E+11	250	-475	-100	25	-100	89	79,96	80 PL		262,8	10,22	1012,12	19,9
7	VAWT_F14_	2,014E+11	250	-327	-353	173	-353	130	97,22	80 PL		262,8	10,22	1012,14	20,1
8	VAWT_F14_	2,014E+11	250	-327	-353	173	-353	131	97,64	80 PL		262,7	10,21	1012,18	20,1
9	VAWT_F14_	2,014E+11	250	-327	-353	173	-353	129	96,8	80 PL		262,7	10,21	1012,17	20,6
10	VAWT_F14_	2,014E+11	250	-430	-200	70	-200	129	96,8	80 PL		262,8	10,25	1012,17	20,4
11	VAWT_F14_	2,014E+11	250	-430	-200	70	-200	130	97,22	80 PL		262,9	10,24	1012,21	20,1
12	VAWT_F14_	2,014E+11	250	-430	-200	70	-200	131	97,64	80 PL		262,8	10,23	1012,29	20,3
13	VAWT_F14_	2,014E+11	250	-430	-375	70	-375	131	97,64	80 PL		262,6	10,24	1012,32	20
14	VAWT_F14_	2,014E+11	250	-430	-375	70	-375	130	97,22	80 PL		262,8	10,23	1012,33	20,2
15	VAWT_F14_	2,014E+11	250	-430	-375	70	-375	129	96,8	80 PL		262,7	10,23	1012,31	20,1
16	VAWT_F14_	2,014E+11	250	-333	-220	167	-220	129	96,8	80 PL		262,8	10,23	1012,27	19,8
17	VAWT_F14_	2,014E+11	250	-333	-220	167	-220	130	97,22	80 PL		262,8	10,21	1012,25	19,6
18	VAWT_F14_	2,014E+11	250	-333	-220	167	-220	131	97,64	80 PL		262,8	10,21	1012,23	20,5
19	VAWT_F14_	2,014E+11	250	-280	470	220	470	45	61,44	80 PL		262,9	10,21	1012,18	20,5
20	VAWT_F14_	2,014E+11	250	-280	470	220	470	44	61,02	80 PL		262,8	10,21	1012,17	20,2
21	VAWT_F14_	2,014E+11	150	-280	470	220	470	46	61,86	80 PL		262,7	10,2	1012,15	19,9
22	VAWT_F14_	2,014E+11	150	-390	470	110	470	46	61,86	90 PL		262,8	10,2	1012,16	20,2
23	VAWT_F14_	2,014E+11	150	-390	470	110	470	45	61,44	90 PL		263,8	10,24	1012,12	19,8
24	VAWT_F14_	2,014E+11	150	-390	470	110	470	44	61,02	90 PL		263,8	10,24	1012,09	20
25	VAWT_F14_	2,014E+11	150	-390	250	110	250	44	61,02	90 PL		263,8	10,24	1012,01	19,9
26	VAWT_F14_	2,014E+11	150	-390	250	110	250	45	61,44	90 PL		263,8	10,25	1012,03	20,2
27	VAWT_F14_	2,014E+11	150	-390	250	110	250	46	61,86	90 PL		263,8	10,24	1012,05	20,2
28	VAWT_F14_	2,014E+11	150	-260	320	240	320	46	61,86	90 PL		263,8	10,23	1012,09	20,2
29	VAWT_F14_	2,014E+11	150	-260	320	240	320	45	61,44	90 PL		263,8	10,23	1012,11	20,2
30	VAWT_F14_	2,014E+11	150	-260	320	240	320	44	61,02	90 PL		263,8	10,24	1012,14	20,2
31	VAWT_F14_	2,014E+11	250	-40	370	460	370	359	42,08	90 PL		263,8	10,23	1012,21	20,3
32	VAWT_F14_	2,014E+11	250	-40	370	460	370	0	42,5	90 PL		263,8	10,23	1012,26	20,2
33	VAWT_F14_	2,014E+11	250	-40	370	460	370	1	42,93	90 PL		263,9	10,23	1012,27	20,3
34	VAWT_F14_	2,014E+11	250	-40	489	460	489	1	42,93	90 PL		263,8	10,22	1012,26	20,1
35	VAWT_F14_	2,014E+11	250	-40	489	460	489	0	42,5	90 PL		263,8	10,21	1012,26	20,2
36	VAWT_F14_	2,014E+11	250	-40	489	460	489	359	42,08	90 PL		264	10,21	1012,31	20,2
37	VAWT_F14_	2,014E+11	250	110	489	610	489	359	42,08	90 PL		263,8	10,2	1012,19	20,3
38	VAWT_F14_	2,014E+11	250	110	489	610	489	0	42,5	90 PL		263,8	10,2	1012,15	20
39	VAWT_F14_	2,014E+11	250	110	489	610	489	1	42,93	90 PL		263,8	10,2	1012,17	20,2
40	VAWT_F14_	2,014E+11	250	100	370	600	370	1	42,93	90 PL		265	10,24	1012,26	19,9
41	VAWT_F14_	2,014E+11	250	100	370	600	370	0	42,5	90 PL		265	10,23	1012,31	20,1
42	VAWT_F14_	2,014E+11	250	100	370	600	370	359	42,08	90 PL		265	10,23	1012,28	20,2
43	VAWT_F14_	2,014E+11	250	360	370	860	370	304	170,45	90 PL		265	10,23	1012,27	20,1
44	VAWT_F14_	2,014E+11	250	360	370	860	370	305	170,87	90 PL		265	10,22	1012,21	20,1
45	VAWT_F14_	2,014E+11	250	360	370	860	370	306	171,29	90 PL		265	10,22	1012,29	20
46	VAWT_F14_	2,014E+11	250	360	200	860	200	306	171,29	90 PL		265	10,22	1012,4	20,2
47	VAWT_F14_	2,014E+11	250	360	200	860	200	305	170,87	90 PL		265	10,21	1012,45	20,1
48	VAWT_F14_	2,014E+11	250	360	200	860	200	304	170,45	90 PL		265	10,2	1012,41	20,2
49	VAWT_F14_	2,014E+11	250	480	200	980	200	304	170,45	90 PL		265	10,2	1012,4	20,1
50	VAWT_F14_	2,014E+11	250	480	200	980	200	305	170,87	90 PL		265	10,2	1012,49	20,2
51	VAWT_F14_	2,014E+11	250	480	200	980	200	306	171,29	90 PL		266	10,23	1012,49	20,2
52	VAWT_F14_	2,014E+11	250	480	370	980	370	306	171,29	90 PL		266	10,23	1012,59	20,1
53	VAWT_F14_	2,014E+11	250	480	370	980	370	305	170,87	90 PL		266	10,23	1012,58	19,5
54	VAWT_F14_	2,014E+11	250	480	370	980	370	304	170,45	90 PL		266	10,22	1012,56	20,1
55	VAWT_F14_	2,014E+11	250	510	100	1010	100	269	155,72	90 PL		266	10,22	1012,59	19,9
56	VAWT_F14_	2,014E+11	250	510	100	1010	100	270	156,14	90 PL		266	10,21	1012,63	20,2
57	VAWT_F14_	2,014E+11	250	510	100	1010	100	271	156,56	90 PL		266	10,21	1012,64	20,2
58	VAWT_F14_	2,014E+11	250	510	-110	1010	-110	271	156,56	90 PL		266	10,21	1012,66	20,2
59	VAWT_F14_	2,014E+11	250	510	-110	1010	-110	270	156,14	90 PL		266	10,2	1012,68	20,2
60	VAWT_F14_	2,014E+11	250	510	-110	1010	-110	269	155,72	90 PL		266	10,2	1012,75	20,2
61	VAWT_F14_	2,014E+11	250	480	-200	980	-200	234	140,99	90 PL		267	10,23	1012,69	20,2
62	VAWT_F14_	2,014E+11	250	480	-200	980	-200	235	141,41	90 PL		267	10,23	1012,74	20,2
63	VAWT_F14_	2,014E+11	250	480	-200	980	-200	236	141,83	90 PL		267	10,22	1012,77	20,1
64	VAWT_F14_	2,014E+11	250	360	-200	860	-200	236	141,83	90 PL		267	10,22	1012,68	20,2
65	VAWT_F14_	2,014E+11	250	360	-200	860	-200	235	141,41	90 PL		267	10,22	1012,68	20,1

Tip Speed Ratio = 2 _ VAWT_F14_TSR20_2

Basic Info				Absolute CoordSys*		Traverse CoordSys		Measurement Parameters				OJF			
No.	Name	Rec. Time	Sample	x	y	x	y	Azimuth	Ref. Time	Sep. Time	Acq. Rate	RPM	Speed	Pressure	Temperature
66	VAWT_F14_	2,014E+11	250	360	-200	860	-200	234	140,99	90 PL		267	10,21	1012,64	20,2
67	VAWT_F14_	2,014E+11	250	360	-370	860	-370	234	140,99	90 PL		267	10,2	1012,67	20,2
68	VAWT_F14_	2,014E+11	250	360	-370	860	-370	235	141,41	90 PL		268	10,23	1012,66	19,8
69	VAWT_F14_	2,014E+11	250	360	-370	860	-370	236	141,83	90 PL		268	10,23	1012,68	19,9
70	VAWT_F14_	2,014E+11	250	480	-370	980	-370	236	141,83	90 PL		268	10,23	1012,69	20,2
71	VAWT_F14_	2,014E+11	250	480	-370	980	-370	235	141,41	90 PL		268	10,22	1012,85	19,7
72	VAWT_F14_	2,014E+11	250	480	-370	980	-370	234	140,99	90 PL		268	10,22	1012,9	20,1

Tip Speed Ratio = 2 _ VAWT_F14_TSR20_VORTEX_BASTARDS

Basic Info				Absolute CoordSys*		Traverse CoordSys		Measurement Parameters				OJF			
No.	Name	Rec. Time	Sample	x	y	x	y	Azimuth	Ref. Time	Sep. Time	Acq. Rate	RPM	Speed	Pressure	Temperature
1	VAWT_F14_	2,014E+11	300	-400	300	100	300	70	71,97	80 PL		268,2	10,22	1005,13	20,3
2	VAWT_F14_	2,014E+11	300	-420	80	80	80	70	71,97	80 PL		268	10,21	1005,06	20,1
3	VAWT_F14_	2,014E+11	300	-440	220	60	220	80	76,17	80 PL		269,3	20,21	1003,23	19,8
4	VAWT_F14_	2,014E+11	300	-450	0	50	0	80	76,17	80 PL		269	10,2	1003,07	20,1
5	VAWT_F14_	2,014E+11	300	-430	30	70	30	100	84,59	25 PL		270,2	10,24	1002,66	19,8

6	VAWT_F14_'	2,014E+11	300	-430	-150	70	-150	100	84,59	25	PL	270,2	10,23	1002,56	19,9
7	VAWT_F14_'	2,014E+11	300	-430	-90	70	-90	90	80,38	25	PL	270,2	10,21	1002,45	20
8	VAWT_F14_'	2,014E+11	300	-430	140	70	140	90	80,38	25	PL	270,2	10,21	1002,25	20,2
9	VAWT_F14_'	2,014E+11	300	-430	140	70	140	87,5	79,33	25	PL	270,2	10,21	1002,23	20,2
10	VAWT_F14_'	2,014E+11	300	-430	140	70	140	85	78,28	25	PL	270,2	10,21	1002,09	20,1
11	VAWT_F14_'	2,014E+11	300	-410	-260	90	-260	110	88,8	25	PL	270,2	10,21	1001,96	20
12	VAWT_F14_'	2,014E+11	300	-410	-30	90	-30	110	88,8	25	PL	270,2	10,2	1001,89	20
13	VAWT_F14_'	2,014E+11	300	-390	-110	110	-110	120	93,01	25	PL	270,2	10,19	1001,74	20
14	VAWT_F14_'	2,014E+11	150	-390	-350	110	-350	120	93,01	25	PL	271,5	10,22	1001,62	19,9
15	VAWT_F14_'	2,014E+11	300	-430	-70	70	-70	87,5	79,33	25	PL	271,5	10,22	1001,59	19,9
16	VAWT_F14_'	2,014E+11	300	-430	-50	70	-50	85	78,28	25	PL	271,3	10,23	1001,5	20,1
17	VAWT_F14_'	2,014E+11	300	380	-370	880	-370	230	139,31	25	PL	268,3	10,23	1003,12	20,5
18	VAWT_F14_'	2,014E+11	300	400	-370	900	-370	232,5	140,36	25	PL	268,2	10,23	1003,42	20,5
19	VAWT_F14_'	2,014E+11	300	400	-350	900	-350	235	141,41	25	PL	268,1	10,22	1003,57	20,5
20	VAWT_F14_'	2,014E+11	300	430	-300	930	-300	240	143,51	25	PL	268,2	10,21	1003,72	20,4
21	VAWT_F14_'	2,014E+11	300	465	-245	965	-245	250	147,72	25	PL	269,2	10,23	1003,87	20,4
22	VAWT_F14_'	2,014E+11	300	510	-170	1010	-170	260	151,93	25	PL	269,2	10,23	1003,98	20,4
23	VAWT_F14_'	2,014E+11	300	530	-110	1030	-110	270	156,14	25	PL	269,2	10,23	1004,15	20,6
24	VAWT_F14_'	2,014E+11	300	530	-20	1030	-20	280	160,35	25	PL	269,2	10,22	1004,26	20,2
25	VAWT_F14_'	2,014E+11	300	530	60	1030	60	290	164,56	25	PL	269,2	10,22	1004,33	20,2
26	VAWT_F14_'	2,014E+11	300	530	140	1030	140	300	168,77	25	PL	269,2	10,22	1004,37	20,6
27	VAWT_F14_'	2,014E+11	300	480	210	980	210	310	172,98	25	PL	269,2	10,22	1004,44	20,4
28	VAWT_F14_'	2,014E+11	300	410	280	910	280	320	177,18	25	PL	269,2	10,21	1004,5	20,3

VAWT_F14_PITCH_ANGLE

Basic Info				Absolute CoordSys*		Traverse CoordSys		Measurement Parameters				OJF			
No.	Name	Rec. Time	Sample	x	y	x	y	Azimuth	Ref. Time	Sep. Time	Acq. Rate	RPM	Speed	Pressure	Temperature
1	VAWT_F14_I	2,014E+11	10	-490	0	10	0	89	146,367		PL	2	0,47	1004,95	18,1
1	VAWT_F14_I	2,014E+11	10	-490	0	10	0	89,5			PL	2	0,47	1004,95	18,1
2	VAWT_F14_I	2,014E+11	10	-490	0	10	0	90	148,537		PL	2	0,47	1004,95	18,1
3	VAWT_F14_I	2,014E+11	10	-490	0	10	0	90,5	149,622		PL	2	0,47	1004,95	18,1
4	VAWT_F14_I	2,014E+11	10	-490	0	10	0	91	150,708		PL	2	0,47	1004,95	18,1
5	VAWT_F14_I	2,014E+11	10	-490	0	10	0	91,5	151,793		PL	2	0,47	1004,95	18,1
6	VAWT_F14_I	2,014E+11	10	-490	0	10	0	92	152,878		PL	2	0,47	1004,95	18,1
7	VAWT_F14_I	2,014E+11	10	-490	0	10	0	92,5	153,963		PL	2	0,47	1004,95	18,1
8	VAWT_F14_I	2,014E+11	10	-490	0	10	0	269	153,963		PL	2	0,47	1004,95	17,3
9	VAWT_F14_I	2,014E+11	10	-490	0	10	0	269,5	538,077		PL	2	0,47	1004,95	17,3
10	VAWT_F14_I	2,014E+11	10	-490	0	10	0	270	539,162		PL	2	0,47	1004,95	17,3
11	VAWT_F14_I	2,014E+11	10	-490	0	10	0	270,5	540,247		PL	2	0,47	1004,95	17,3
12	VAWT_F14_I	2,014E+11	10	-490	0	10	0	271	541,333		PL	2	0,47	1004,95	17,3
13	VAWT_F14_I	2,014E+11	10	-490	0	10	0	271,5	542,417		PL	2	0,47	1004,95	17,3
14	VAWT_F14_I	2,014E+11	10	-500	0	10	0	272	543,503		PL	2	0,47	1004,95	17,3
15	VAWT_F14_I	2,014E+11	10	-490	0	10	0	272,5	544,588		PL	2	0,47	1004,95	17,3

VAWT_F14_PITCH_ANGLE_BI

Basic Info				Absolute CoordSys*		Traverse CoordSys		Measurement Parameters				OJF			
No.	Name	Rec. Time	Sample	x	y	x	y	Azimuth	Ref. Time	Sep. Time	Acq. Rate	RPM	Speed	Pressure	Temperature
1	VAWT_F14_I	2,014E+11	10	-490	0	10	0	89	146,367		PL	2	0,47	1004,95	18,1
1	VAWT_F14_I	2,014E+11	10	-490	0	10	0	89,5			PL	2	0,47	1004,95	18,1
2	VAWT_F14_I	2,014E+11	10	-490	0	10	0	90	148,537		PL	2	0,47	1004,95	18,1
3	VAWT_F14_I	2,014E+11	10	-490	0	10	0	90,5	149,622		PL	2	0,47	1004,95	18,1
4	VAWT_F14_I	2,014E+11	10	-490	0	10	0	91	150,708		PL	2	0,47	1004,95	18,1
5	VAWT_F14_I	2,014E+11	10	-490	0	10	0	91,5	151,793		PL	2	0,47	1004,95	18,1
6	VAWT_F14_I	2,014E+11	10	-490	0	10	0	92	152,878		PL	2	0,47	1004,95	18,1
7	VAWT_F14_I	2,014E+11	10	-490	0	10	0	92,5	153,963		PL	2	0,47	1004,95	18,1
8	VAWT_F14_I	2,014E+11	10	-490	0	10	0	269	153,963		PL	2	0,47	1004,95	17,3
9	VAWT_F14_I	2,014E+11	10	-490	0	10	0	269,5	538,077		PL	2	0,47	1004,95	17,3
10	VAWT_F14_I	2,014E+11	10	-490	0	10	0	270	539,162		PL	2	0,47	1004,95	17,3
11	VAWT_F14_I	2,014E+11	10	-490	0	10	0	270,5	540,247		PL	2	0,47	1004,95	17,3
12	VAWT_F14_I	2,014E+11	10	-490	0	10	0	271	541,333		PL	2	0,47	1004,95	17,3
13	VAWT_F14_I	2,014E+11	10	-490	0	10	0	271,5	542,417		PL	2	0,47	1004,95	17,3
14	VAWT_F14_I	2,014E+11	10	-500	0	10	0	272	543,503		PL	2	0,47	1004,95	17,3
15	VAWT_F14_I	2,014E+11	10	-490	0	10	0	272,5	544,588		PL	2	0,47	1004,95	17,3

Tip Speed Ratio = 4.5 _ VAWT_F14_TSR45_BI

Basic Info				Absolute CoordSys*		Traverse CoordSys		Measurement Parameters				OJF			
No.	Name	Rec. Time	Sample	x	y	x	y	Azimuth	Ref. Time	Sep. Time	Acq. Rate	RPM	Speed	Pressure	Temperature
1	VAWT_F14_'	2,014E+11	150	-100	390	400	390	179	11,688	80	PL	242,5	9,11	1005,59	19,7
2	VAWT_F14_'	2,014E+11	150	-100	390	400	390	180	11,902	80	PL	245,5	9,11	1005,62	19,7
3	VAWT_F14_'	2,014E+11	150	-100	390	400	390	181	12,115	80	PL	242,5	9,11	1005,62	19,8
4	VAWT_F14_'	2,014E+11	150	100	390	600	390	181	12,115	80	PL	242,5	9,11	1005,63	19,8
5	VAWT_F14_'	2,014E+11	150	100	390	600	390	180	11,902	80	PL	242,5	9,1	1005,69	19,8
6	VAWT_F14_'	2,014E+11	150	100	390	600	390	179	11,688	80	PL	242,5	9,1	1005,7	19,8
7	VAWT_F14_'	2,014E+11	150	80	489	580	489	179	11,688	80	PL	242,5	9,1	1005,71	19,8
8	VAWT_F14_'	2,014E+11	150	100	489	600	489	180	11,902	80	PL	242,5	9,1	1005,71	19,8
9	VAWT_F14_'	2,014E+11	150	100	489	600	489	181	12,115	80	PL	242,5	9,11	1005,76	19,8
10	VAWT_F14_'	2,014E+11	150	-60	489	440	489	181	12,115	80	PL	242,5	9,1	1005,78	19,8
11	VAWT_F14_'	2,014E+11	150	-60	489	440	489	180	11,902	80	PL	242,5	9,1	1005,76	19,7
12	VAWT_F14_'	2,014E+11	150	-60	489	440	489	179	11,688	80	PL				

Tip Speed Ratio = 2 _VAWT_F14_TSR20_BI

Basic Info				Absolute CoordSys*		Traverse CoordSys		Measurement Parameters				OJF			
No.	Name	Rec. Time	Sample	x	y	x	y	Azimuth	Ref. Time	Sep. Time	Acq. Rate	RPM	Speed	Pressure	Temperature
1	VAWT_F14_'	2,014E+11	250	-100	390	400	390	179	52,113	80	PL	269	10,22	1006,04	20
2	VAWT_F14_'	2,014E+11	250	-100	390	400	390	180	52,534	80	PL	269	10,22	1006	20
3	VAWT_F14_'	2,014E+11	250	-100	390	400	390	181	52,955	80	PL	269	10,22	1006,05	20
4	VAWT_F14_'	2,014E+11	250	100	390	600	390	181	52,955	80	PL	269	10,22	1006,01	20
5	VAWT_F14_'	2,014E+11	250	100	390	600	390	180	52,534	80	PL	269	10,21	1006,03	19,9
6	VAWT_F14_'	2,014E+11	250	100	390	600	390	179	52,113	80	PL	269	10,2	1006,1	20
7	VAWT_F14_'	2,014E+11	250	80	489	580	489	179	52,113	80	PL	269	10,2	1006,05	20
8	VAWT_F14_'	2,014E+11	250	100	489	600	489	180	52,534	80	PL	269	10,2	1006,09	20,1
9	VAWT_F14_'	2,014E+11	250	100	489	600	489	181	52,955	80	PL	269	10,2	1006,15	20
10	VAWT_F14_'	2,014E+11	250	-60	489	440	489	181	52,955	80	PL	269	10,19	1006,22	20
11	VAWT_F14_'	2,014E+11	250	-60	489	440	489	180	52,534	80	PL	269	10,19	1006,28	20
12	VAWT_F14_'	2,014E+11	250	-60	489	440	489	179	52,113	80	PL	269	10,19	1006,33	20

Tip Speed Ratio = 2 _ VAWT_F14_TSR20_VORTEX_BASTARDS_BI

Basic Info				Absolute CoordSys*		Traverse CoordSys		Measurement Parameters				OJF			
No.	Name	Rec. Time	Sample	x	y	x	y	Azimuth	Ref. Time	Sep. Time	Acq. Rate	RPM	Speed	Pressure	Temperature
1	VAWT_F14_'	2,014E+11	300	-390	350	110	350	120	103,039	25	PL	266	10,24	1009,88	20,5
2	VAWT_F14_'	2,014E+11	300	-390	120	110	120	120	103,039	25	PL	266	10,23	1009,88	20,4
3	VAWT_F14_'	2,014E+11	300	-335	200	165	200	130	107,248	25	PL	266	10,24	1009,76	20,5
4	VAWT_F14_'	2,014E+11	300	-335	410	165	410	130	107,248	25	PL	266	10,24	1009,54	20,5
5	VAWT_F14_'	2,014E+11	300	-280	480	220	480	140	111,456	25	PL	266	10,23	1009,42	20
6	VAWT_F14_'	2,014E+11	300	-330	270	170	270	140	111,456	25	PL	266	10,23	1009,25	20,2
7	VAWT_F14_'	2,014E+11	300	-260	320	240	320	150	115,665	25	PL	266	10,23	1009,14	20,4
8	VAWT_F14_'	2,014E+11	300	-210	489	290	489	150	115,665	25	PL	266	10,22	1009,08	20,1
9	VAWT_F14_'	2,014E+11	300	-210	360	290	360	160	119,874	25	PL	266	10,22	1009,14	20,2
10	VAWT_F14_'	2,014E+11	150	-90	480	410	480	160	119,874	25	PL	266	10,22	1009,14	20,2
11	VAWT_F14_'	2,014E+11	150	0	489	500	489	170	124,083	25	PL	266	10,2	1009,3	20,4
12	VAWT_F14_'	2,014E+11	300	-140	420	360	420	170	124,083	25	PL	267	10,2	1009,1	20,1
13	VAWT_F14_'	2,014E+11	300	-80	400	420	400	180	128,291	25	PL	267	10,23	1009,1	20,2
14	VAWT_F14_'	2,014E+11	150	80	489	580	489	180	128,291	25	PL	267	10,23	1009,17	20,1
15	VAWT_F14_'	2,014E+11	300	20	390	520	390	190	132,5	25	PL	267	10,23	1009,12	20,3
16	VAWT_F14_'	2,014E+11	300	90	390	590	390	200	136,709	35	PL	267	10,23	1009,06	20,2
17	VAWT_F14_'	2,014E+11	300	170	390	670	390	210	140,948	30	PL	267	10,22	1008,97	20,1
18	VAWT_F14_'	2,014E+11	300	300	430	800	430	210	140,948	30	PL	267	10,22	1008,97	20,1
19	VAWT_F14_'	2,014E+11	300	300	400	800	400	210	145,126	30	PL	267	10,22	1009,01	20,2
20	VAWT_F14_'	2,014E+11	300	-390	120	110	120	120	103,039	25	PL	267	10,21	1009,04	20,4
21	VAWT_F14_'	2,014E+11	250	-390	120	110	120	430	233,51	35	PL	268	10,23	1009,01	20,5
22	VAWT_F14_'	2,014E+11	250	-390	120	110	120	435	235,615	35	PL	268	10,23	1009,01	20,2
22	VAWT_F14_'	2,014E+11	250	-390	120	110	120	440	237,719	35	PL	268	10,23	1008,97	20,1

OJF_Calibration _ OJF_Calibration

Basic Info				Absolute CoordSys*		Traverse CoordSys		Measurement Parameters				OJF			
No.	Name	Rec. Time	Sample	x	y	x	y	Azimuth	Ref. Time	Sep. Time	Acq. Rate	RPM	Speed	Pressure	Temperature
1	OJF_CALIB_	2,014E+11	200	-500	0	0	0	/	/	400	0,8	135,5	4,79	1009,29	19,6
2	OJF_CALIB_	2,014E+11	50	-500	0	0	0	/	/	400	0,8	?	4,1	1009,37	19,7
3	OJF_CALIB_	2,014E+11	50	-500	0	0	0	/	/	400	0,8	161,1	5,87	1009,35	19,7
4	OJF_CALIB_	2,014E+11	200	-500	0	0	0	/	/	200	0,8	241,4	9,13	1009,53	20,1
5	OJF_CALIB_	2,014E+11	200	-500	250	0	250	/	/	200	0,8	241,5	9,13	1009,51	20,2
6	OJF_CALIB_	2,014E+11	200	-500	500	0	500	/	/	200	0,8	241,5	9,13	1009,51	20,2
7	OJF_CALIB_	2,014E+11	200	-500	500	0	500	/	/	200	0,8	267	10,18	1009,55	20
8	OJF_CALIB_	2,014E+11	200	-500	250	0	250	/	/	200	0,8	267	10,19	1009,59	20,3
9	OJF_CALIB_	2,014E+11	200	-500	0	0	0	/	/	200	0,8	267	10,19	1009,68	20,4

Drag Calculations

Basic Info				Absolute CoordSys*		Traverse CoordSys		Measurement Parameters				OJF			
No.	Name	Rec. Time	Sample	x	y	x	y	Azimuth	Ref. Time	Sep. Time	Acq. Rate	RPM	Speed	Pressure	Temperature
1	RPM0_V91	2,014E+11	/	#VALUE!	/	/	/	/	/	/	/	240,3	9,11	1005,04	19,9
2	RPM0_V102	2,014E+11	/	#VALUE!	/	/	/	/	/	/	/	266	10,2	1005,14	20,2
1	RPM13_V91	2,014E+11	/	#VALUE!	/	/	/	/	/	/	/	241,4	9,12	1005,29	20,2
2	RPM661_V1	2,014E+11	/	#VALUE!	/	/	/	/	/	/	/	265	10,15	1005,33	20,1

APPENDIX B

CLASSICAL SEMI-EMPIRICAL MODELS

Originally, semi-empirical dynamic stall models were developed for helicopter applications. In this section these models are described. During the nineties, while wind energy applications were rising in interest, these models were modified for wind energy applications, this will be described in Section 2.6 .

Beddoes-Leishman model (1976-1993)

The Beddoes-Leishman (BL) model is one of the most important dynamic stall models. In Westland (UK), Beddoes worked for a helicopter manufacturer called Westland, and developed a dynamic stall model for helicopter applications. Around 1970, Beddoes included several airfoil dependent non-dimensional time-delay constants in his first generation semi-empirical time-delay dynamic stall model. Many years and revisions later, he managed to deliver the third and final generation model in 1993 [3], with the help of Leishman. The model covers several unsteady effects, and is capable of describing the dynamic variation of not only lift, but also of moment and drag forces. The BL model is capable of predicting a range of unsteady phenomena, and it is a first category semi-empirical model. Note: the modified AoA approach is also used by most models of the third category.

Unsteady attached flow

In fully attached conditions the dynamic lift $C_{L0,d}$ is calculated with four time delay constants in indicial functions; two for the delayed lift, and two for the impulsive contributions due to shockwave propagations as in Equations B.1−B.3. In fully attached conditions, the static lift c_{L0} is defined as a linear curve, shown in Equation B.4. In this equation a flat plate is assumed, where $\partial C_L/\partial\alpha = 2\pi$.

$$C_{L0,d}(t) = C_{L0}(\alpha) - c_1(t) - c_2(t) + c_3(t) + c_4(t) \tag{B.1}$$

$$c_1(t) + \omega_1 c_1(t) = A_1 \dot{c}_{L0}(t), \qquad c_2(t) + \omega_2 c_2(t) = A_2 \dot{C}_{L0}(t) \tag{B.2}$$

$$c_3(t) + \omega_5 c_3(t) = \frac{4}{M} A_3 \dot{\alpha}, \qquad c_4(t) + \omega_6 c_4(t) = \frac{1}{M} A_4 \frac{c}{V} \ddot{\alpha} \tag{B.3}$$

$$C_{L0} = \left. \frac{\partial C_L}{\partial \alpha} \right|_{\alpha_0} (\alpha - \alpha_0) \tag{B.4}$$

Unsteady separated flow

When an airfoil is in separated flow conditions, the Kirchhoff flow theory is applied in order to calculate the lift coefficient. First, the static separation can be described in a linear fashion by the parameter f, with $f = 0$ being fully attached and $f = 1$ being separated flow. Singularities occur when approaching the fully separated flow. To avoid these singularities, f will be described in the complex plane (with the transformation into the separation angle θ by $2f = 1 + \cos\theta$). The approximation for the separation parameter is given by the Kirchhoff-Helmholtz theory [52] and can be seen in Equation B.5. The dynamic separation parameters (f_d, θ_d) are described by an indicial response function, shown in Equation B.6. The dynamic lift is described by the Kirchhoff-Helmholtz model in both the real or the complex plane seen in Equation B.7.

$$f \approx 2\sqrt{\frac{C_L}{C_{L0}}} - 1, \qquad \theta \approx 4\cos^{-1}\left(\left[\frac{C_L}{C_{L0}} \right]^{1/4} \right) \tag{B.5}$$

$$\dot{f}_d(t) = -\omega_3 (f_d(t) - f(\alpha)), \qquad \dot{\theta}_d(t) = -\omega_3 (\theta_d(t) - \theta(\alpha)) \tag{B.6}$$

$$C_{L,d} = \left(\frac{1 + \sqrt{f_d}}{2} \right)^2 C_{L0,d}, \qquad C_{L,d} = \cos^4(\frac{1}{4}\theta_d) C_{L0,d} \tag{B.7}$$

In the BL model, a dynamic AoA α_f for determining the static separation parameter f or θ. These parameters are needed to calculate Equation B.6. A retarded lift coefficient $C'_{L0,d}(t)$ is used. The unsteady unseparated lift coefficient is delayed due to the offset between the pressure coefficient and the dynamic lift during pitching. The corresponding differential equation is shown in Equation B.8. The effective AoA calculated in Equation B.9 is used in Equation B.5 by replacing α with α_f.

$$\dot{C}'_{L0,d}(t) = -\omega_7 (C'_{L0,d}(t) - C_{L0,d}(t)) \tag{B.8}$$

$$\alpha_f = \frac{C'_{L0,d}(t)}{\partial C_L / \partial \alpha|_{\alpha_0}} + \alpha_0 \tag{B.9}$$

Leading-edge separation

In the dynamic stall process, a leading edge vortex is formed. The lift will keep on increasing linearly beyond the separation point of the steady case. At a given point, the vortex detaches, and starts travelling downstream on the airfoil towards the trailing edge, with a speed that is approximately $\frac{V}{3}$. While the leading edge vortex is apparent, a trailing edge vortex is formed to diminish the leading edge vortex strength. As long as the leading edge vortex is travelling over the surface of the airfoil, the lift keeps on increasing in strength. The extra lift contribution of both vortices is denoted by $C_{L,v}$, which is presented in the differential Equation is given in B.10. When the pitching motion is negative again, the building up of the vortex strength stops. The Heaviside function H is used to regulate the equation for the case of a negative pitching motion and the vortex traveling time. To locate the vortex in time on the airfoil, a dimensionless parameter τ is used. For $\tau = 0$ the vortex is still at the leading edge, for $\tau = 1$ at the trailing edge. τ is calculated by Equation B.12 in the BL model, where the vortex detaches and starts traveling when the retarded lift coefficient $c'_{L0,d}(t)$ exceeds a specific airfoil dependent parameter $c'_{L0,v}(t)$.

$$\dot{C}_{L,v}(t) + \omega_4 C_{L,v}(t) = \Delta\dot{C}_L(t) H(1-\tau) H(\dot{\alpha}) \tag{B.10}$$

$$\Delta\dot{C}_L(t) = \dot{C}_{L0,d}(t) - \dot{C}_{L,d}(t) \tag{B.11}$$

$$\dot{\tau} = \frac{V}{3c} H(C'_{L0,d} - C'_{L0,v}) \tag{B.12}$$

State-space representation

The differential Equations B.2, B.3, B.6, B.8, and B.10, are grouped together in a state-space in order to define the seven state variables c_1, c_2, c_3, c_4, $c'_{L0,d}$, f_d, and $c_{L,v}$. It is put in a matrix, presented in B.13 and B.14. $\omega_1 - \omega_7$, $A_1 - A_4$, and $c'_{L0,v}$ are profile dependent parameters that will have to be acquired from test data, together with the static lift curve $c_L(\alpha)$. The lift is finally calculated by adding the delayed lift contributions with the extra lift due to the leading edge vortex, shown in Equation B.15.

$$\dot{\mathbf{z}}(t) = \mathbf{A}\mathbf{z}(t) + \mathbf{b}_0(\alpha, \dot{\alpha}, \ddot{\alpha}) + \mathbf{b}_1 \dot{c}_{L0}(t) \tag{B.13}$$

$$\mathbf{z}(t) = \begin{bmatrix} c_1(t) \\ c_2(t) \\ c_3(t) \\ c_4(t) \\ c'_{L0,d}(t) \\ f_d(t) \\ c_{L,v}(t) \end{bmatrix}, \quad \mathbf{A} = \begin{bmatrix} -\omega_1 & 0 & 0 & 0 & 0 & 0 & 0 \\ 0 & -\omega_2 & 0 & 0 & 0 & 0 & 0 \\ 0 & 0 & -\omega_5 & 0 & 0 & 0 & 0 \\ 0 & 0 & 0 & -\omega_6 & 0 & 0 & 0 \\ -\omega_7 & -\omega_7 & -\omega_7 & -\omega_7 & -\omega_7 & 0 & 0 \\ 0 & 0 & 0 & 0 & 0 & -\omega_3 & 0 \\ 0 & 0 & 0 & 0 & 0 & 0 & -\omega_4 \end{bmatrix},$$

$$\mathbf{b}_0 = \begin{bmatrix} 0 \\ 0 \\ \frac{4}{M} A_3 \dot{\alpha} \\ \frac{1}{M} A_4 \frac{c}{V} \ddot{\alpha} \\ \omega_7 c_{L0}(\alpha) \\ \omega_3 f(\alpha_f) \\ \Delta \dot{c}_L(t) H(1-\tau) H(\dot{\alpha}) \end{bmatrix}, \quad \mathbf{b}_1 = \begin{bmatrix} A_1 \\ A_2 \\ 0 \\ 0 \\ 0 \\ 0 \\ 0 \end{bmatrix} \tag{B.14}$$

$$c_L(t) = c_{L,d}(t) + c_{L,v}(t) \tag{B.15}$$

APPENDIX C

UNCERTAINTIES LOAD CALCULATION METHOD

In this appendix the second azimuthal position is presented for the in Section 4.5 referenced figures.

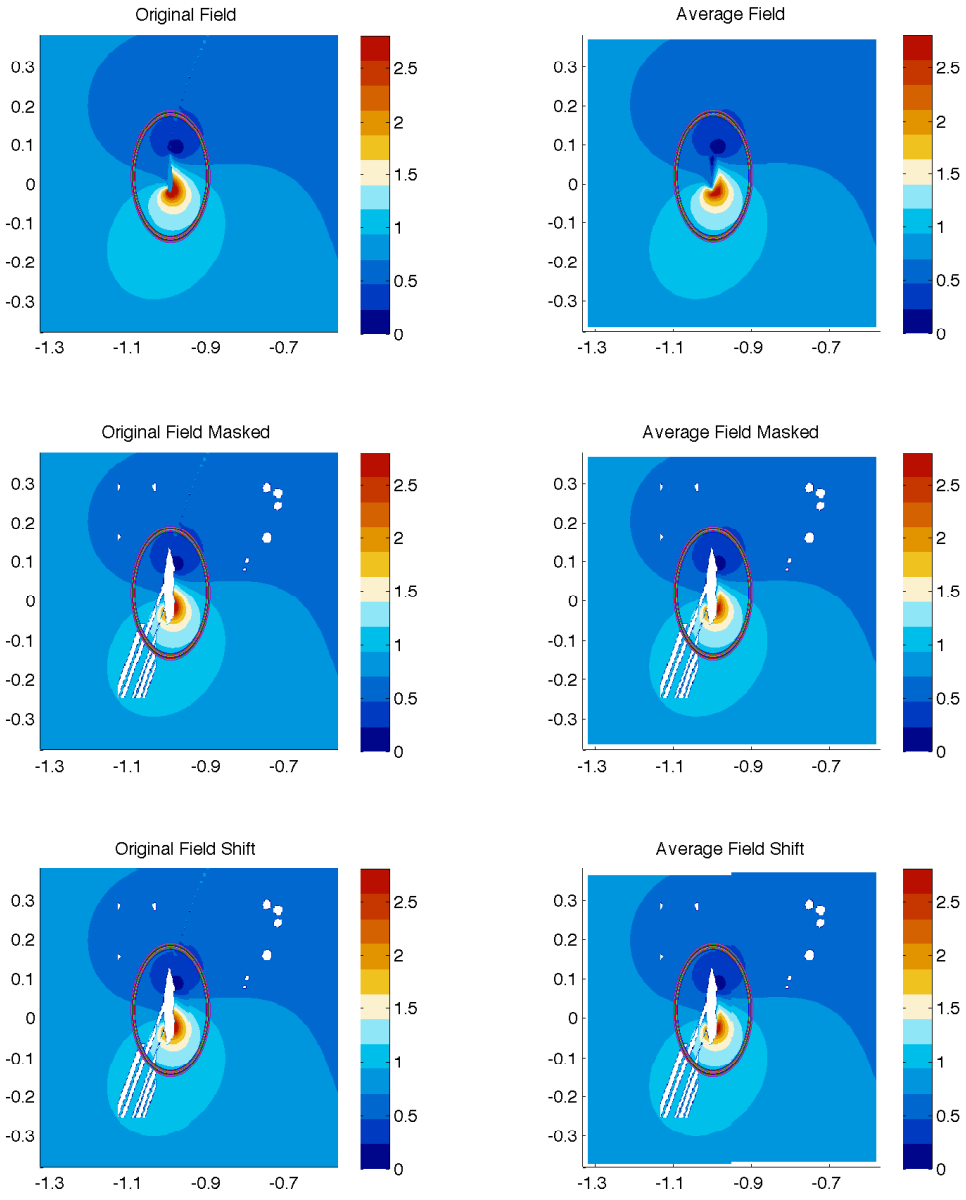

Figure C.1: *Robustness check of the load calculation method at 90° azimuth position.*

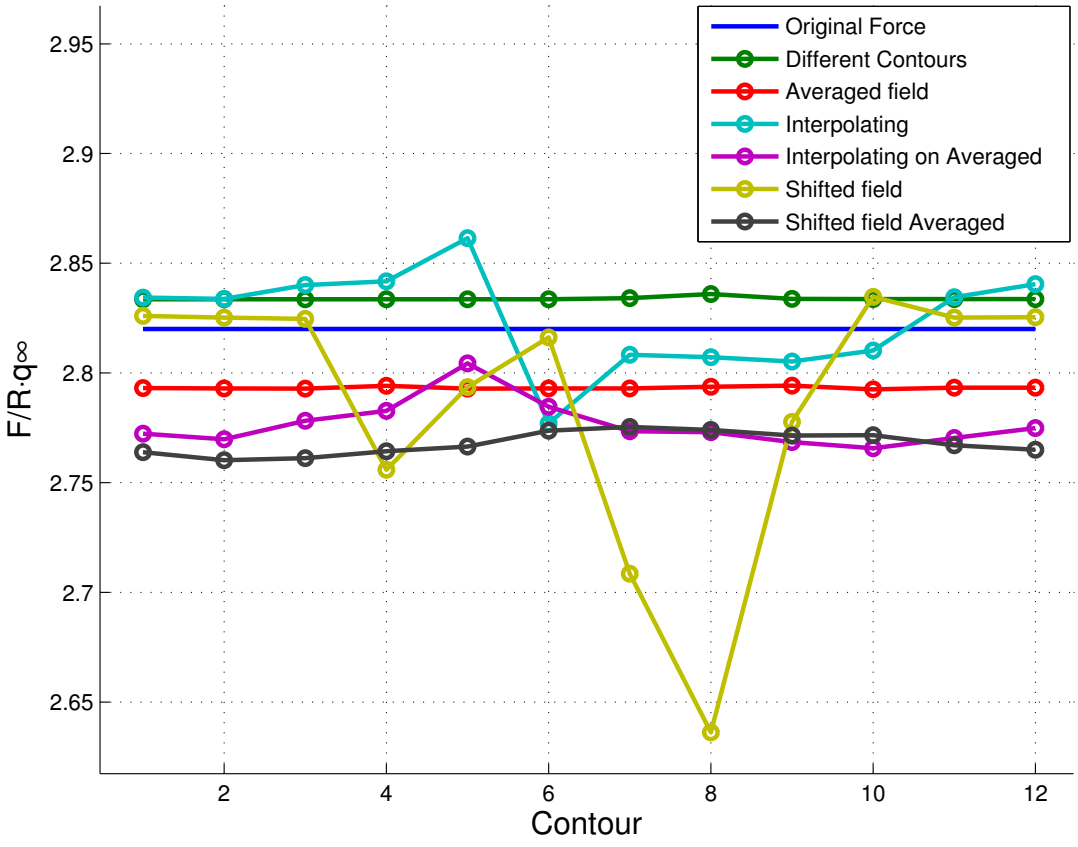

Figure C.2: *The corresponding loads for the robustness check at 90° azimuth position.*

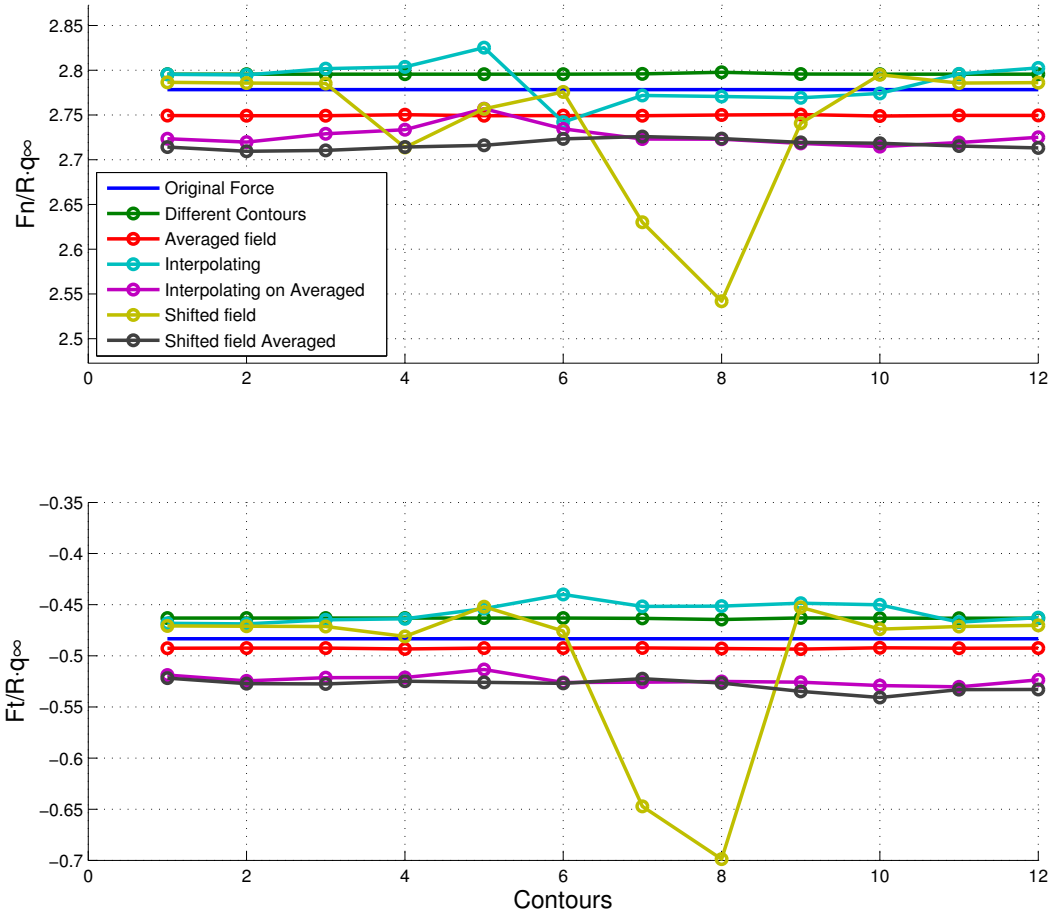

Figure C.3: *The corresponding F_N & F_T loads for the robustness check at 90° azimuth position.*

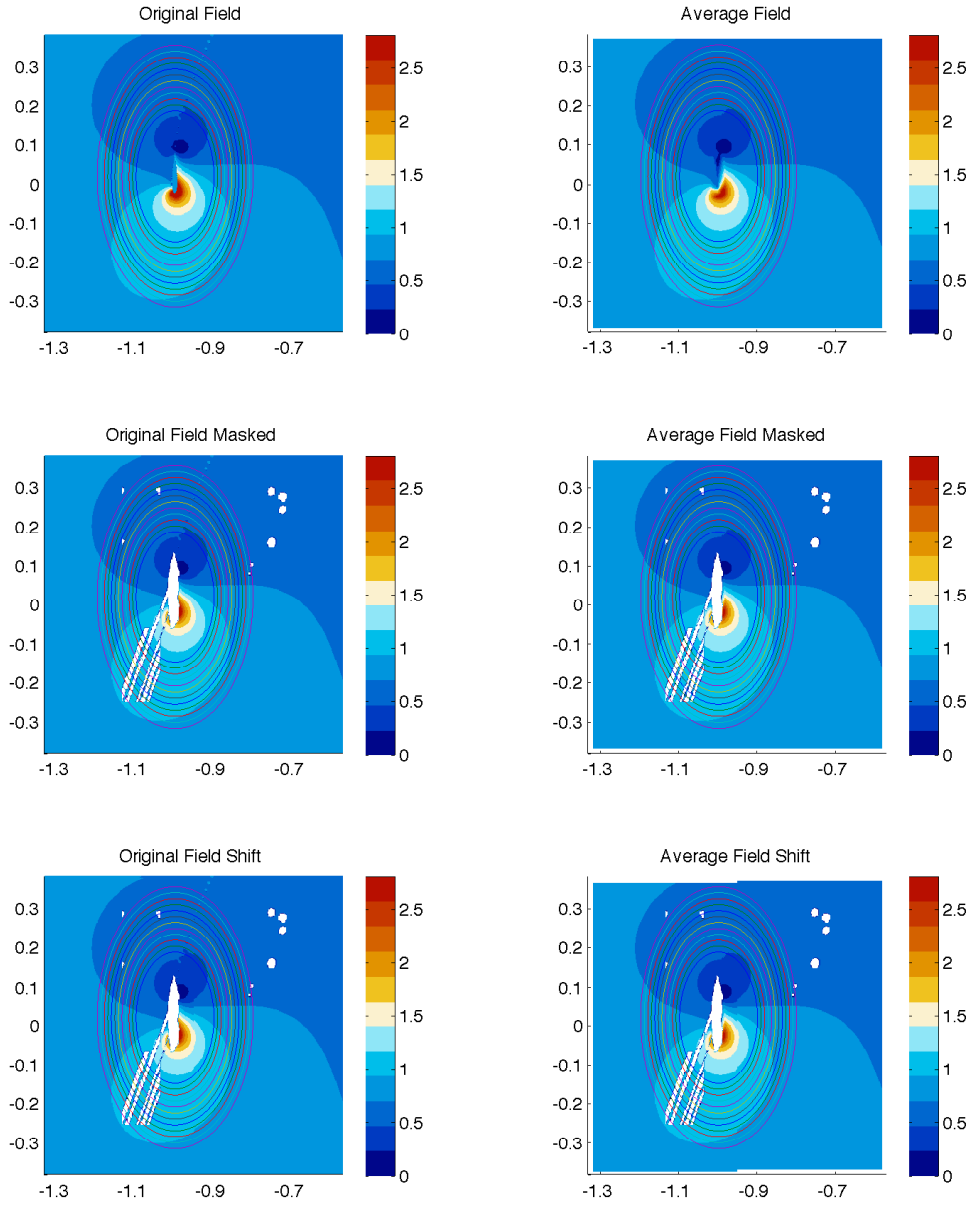

Figure C.4: *Robustness check of the load calculation method at 90° azimuth position.*

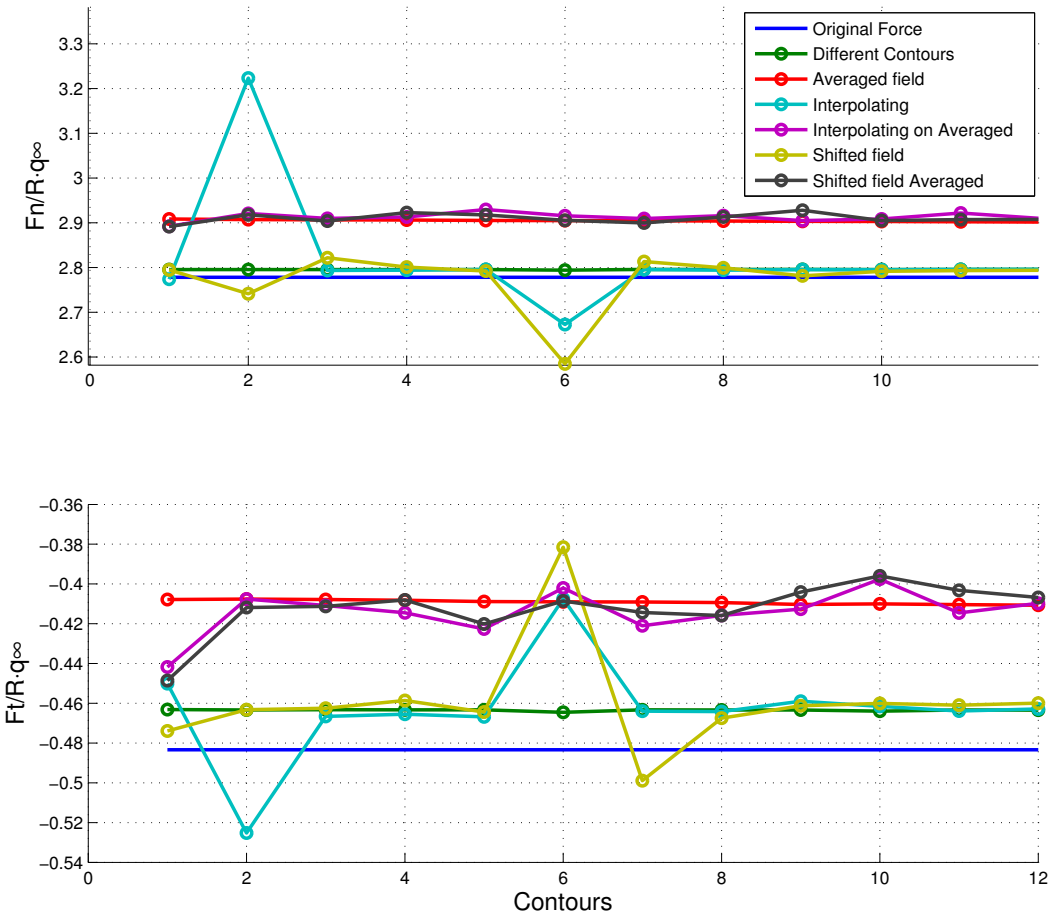

Figure C.5: *The corresponding loads for the robustness check at 90° azimuth position.*

APPENDIX D

CLOSE-UP VELOCITY FIELDS

In this appendix the velocity fields for all azimuthal positions for both TSR cases are presented. In all figures θ_{T-1} and θ_{T+1}, as explained in Section 2.4, are accordingly θ_{T-1} top, θ_T middle and θ_{T+1} down.

The numerical inviscid panel model velocity fields that were used are also presented. These are at the right side in Figure D.1 to D.7.

The different contours that were used, explained in Section 2.4, are also presented in all fields. Due to the compression of the fields the difference between the contours is really small, and is hard to observe. In section 4.5.1 the data can be found to plot these contours.

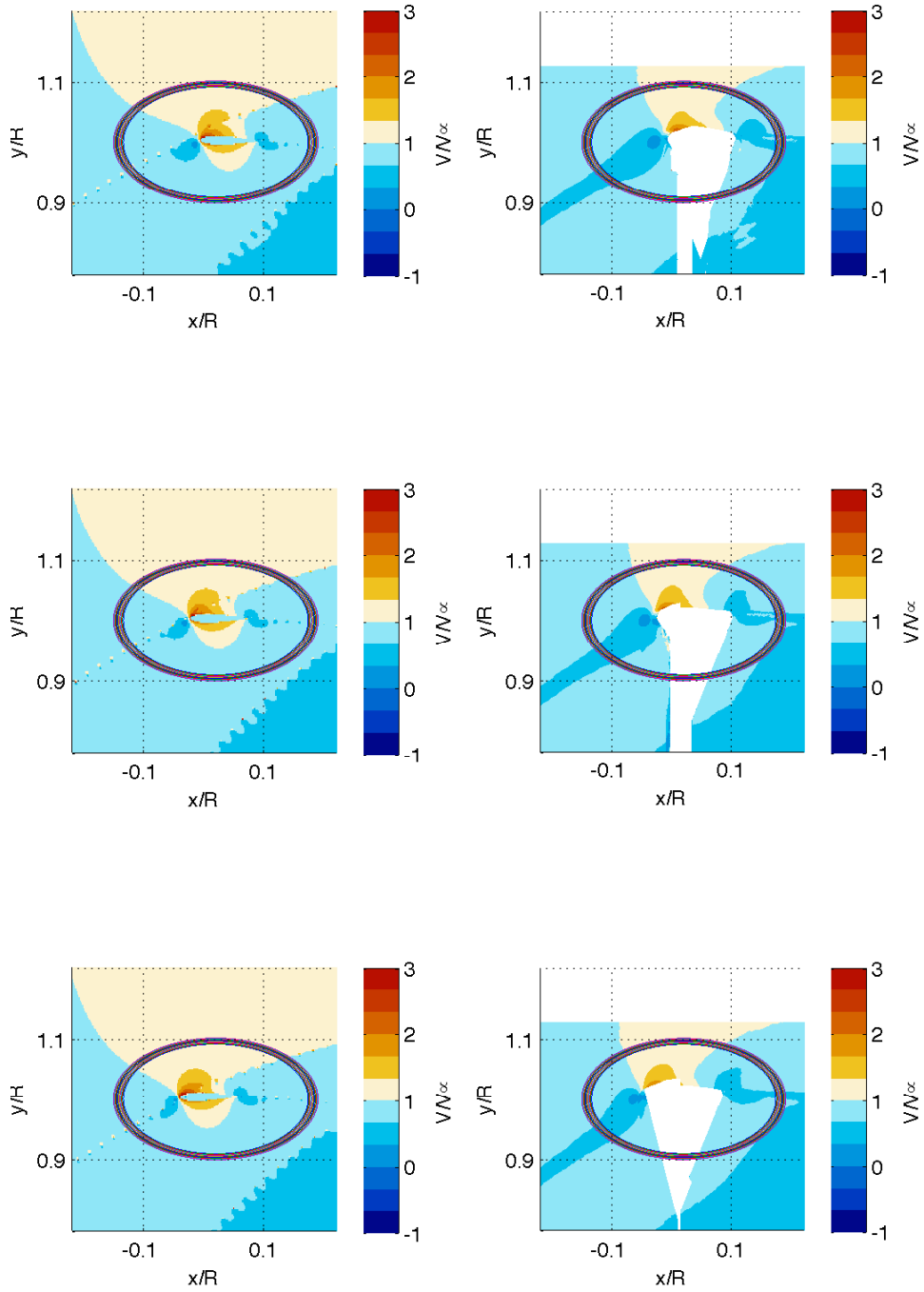

Figure D.1: *The numerical flow fields (left) and the experimental flow field (right) for TSR 4.5 at* $\theta = 0°$.

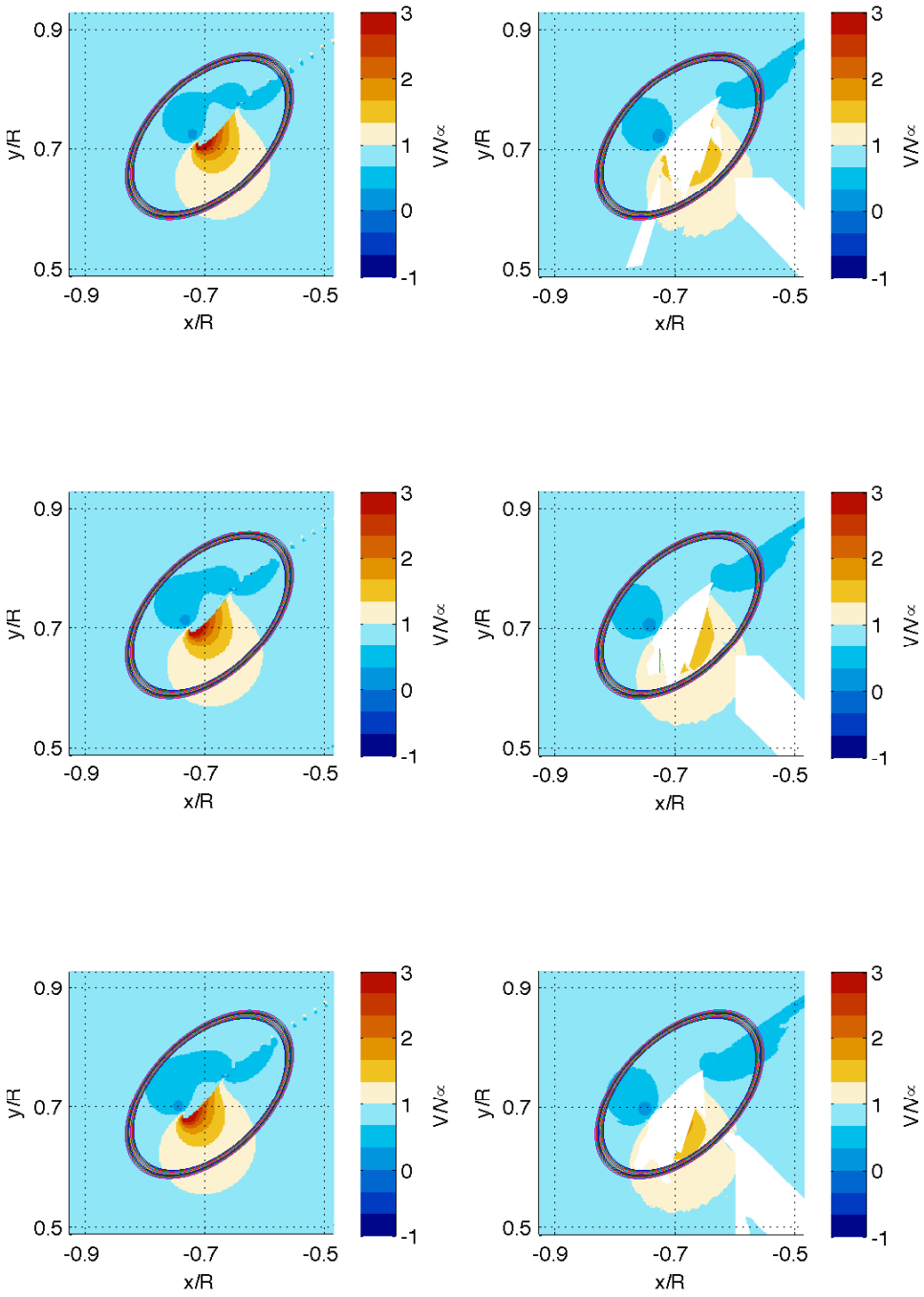

Figure D.2: *The numerical flow fields (left) and the experimental flow field (right) for TSR 4.5 at* $\theta = 45°$.

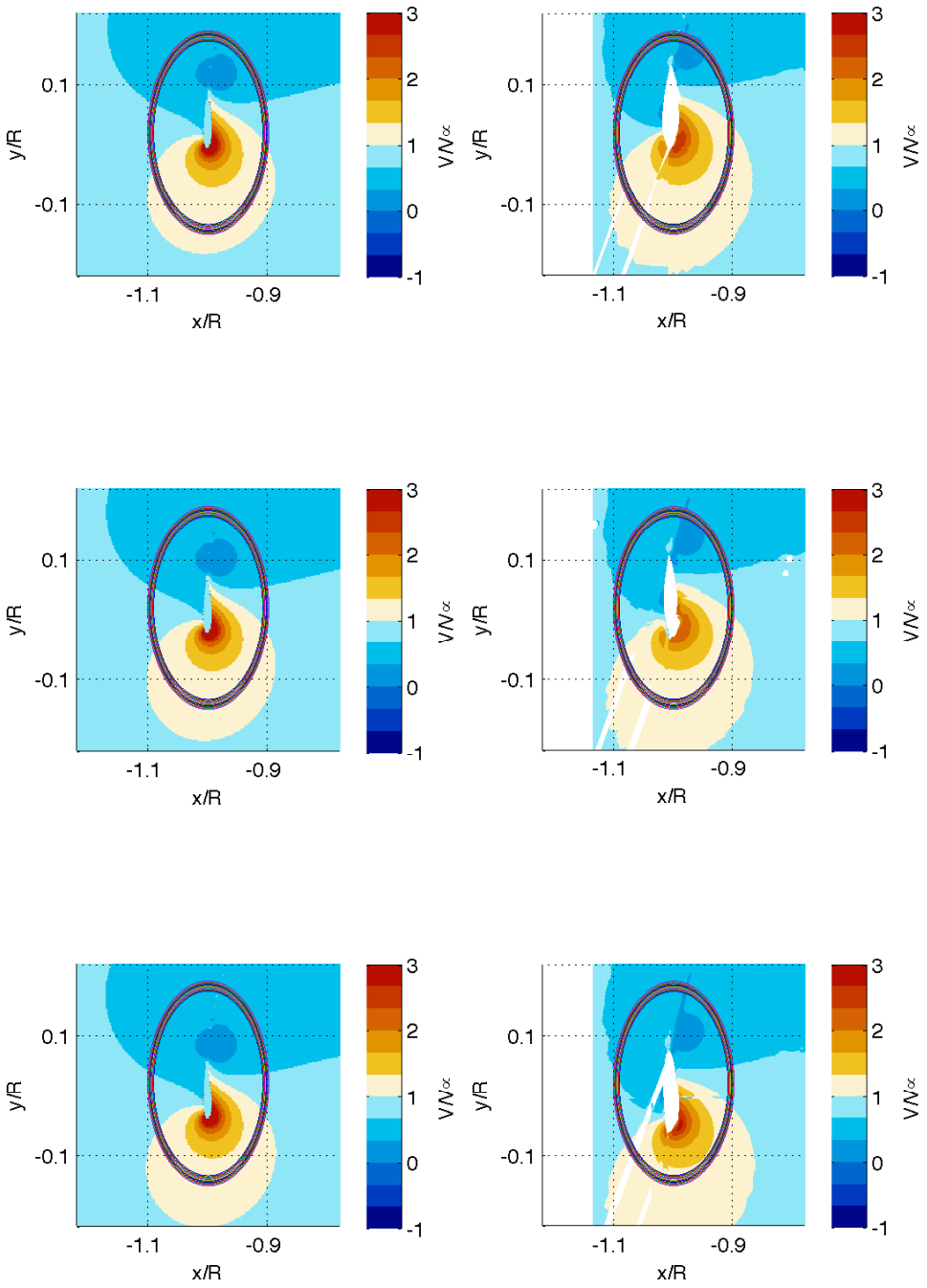

Figure D.3: *The numerical flow fields (left) and the experimental flow field (right) for TSR 4.5 at* $\theta = 90°$.

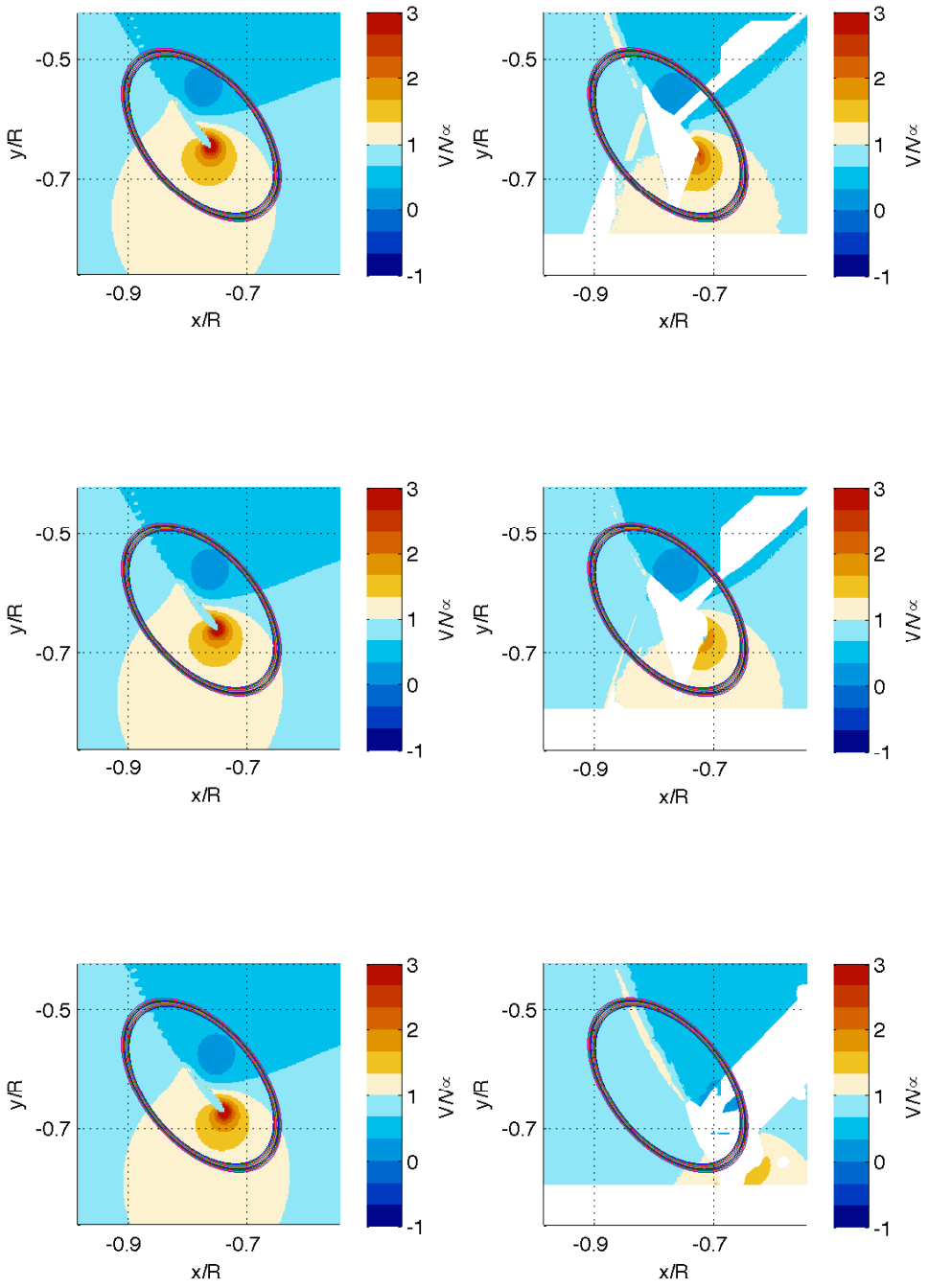

Figure D.4: *The numerical flow fields (left) and the experimental flow field (right) for TSR 4.5 at* $\theta = 130°$.

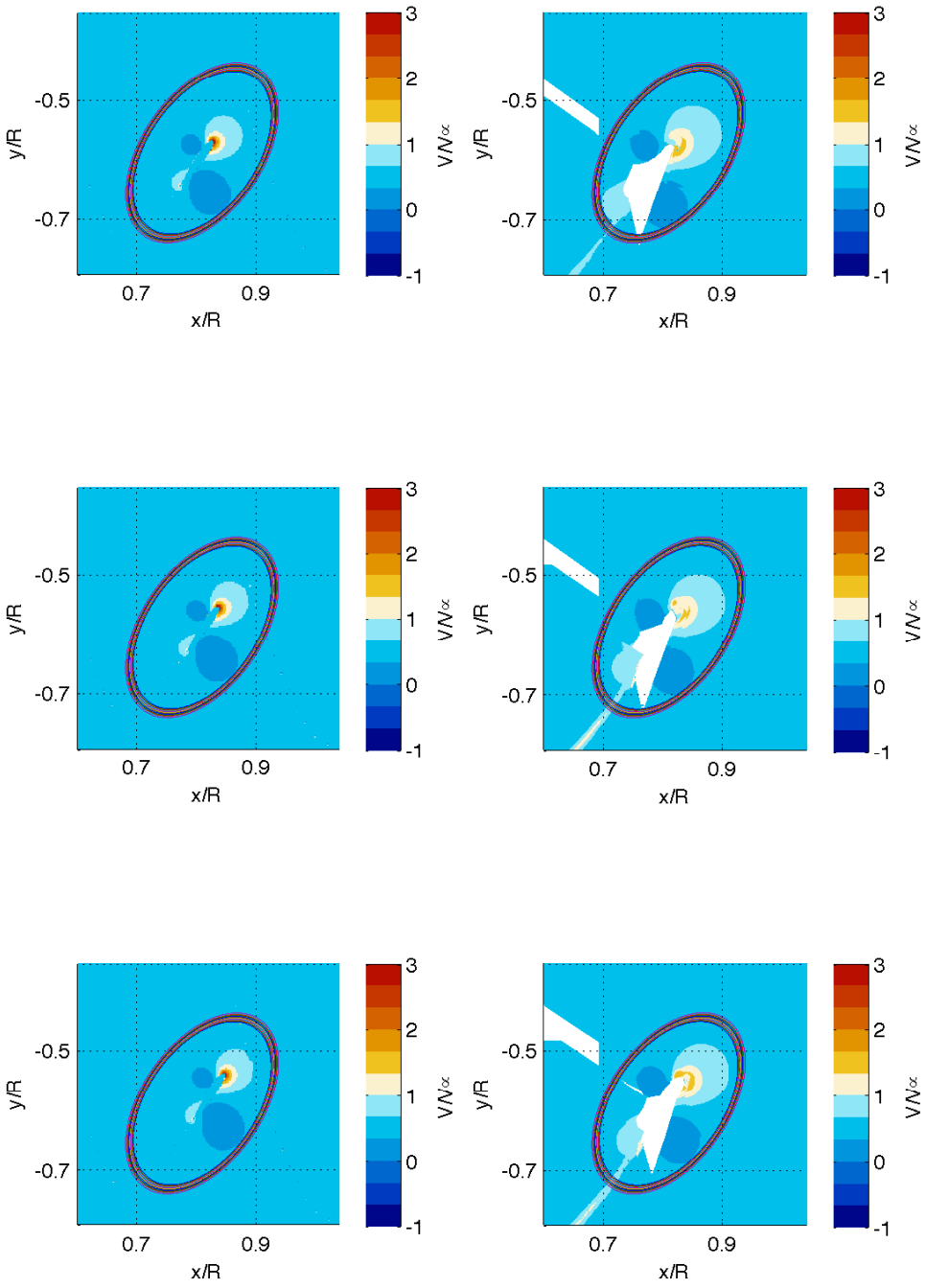

Figure D.5: *The numerical flow fields (left) and the experimental flow field (right) for TSR 4.5 at* $\theta = 235°$.

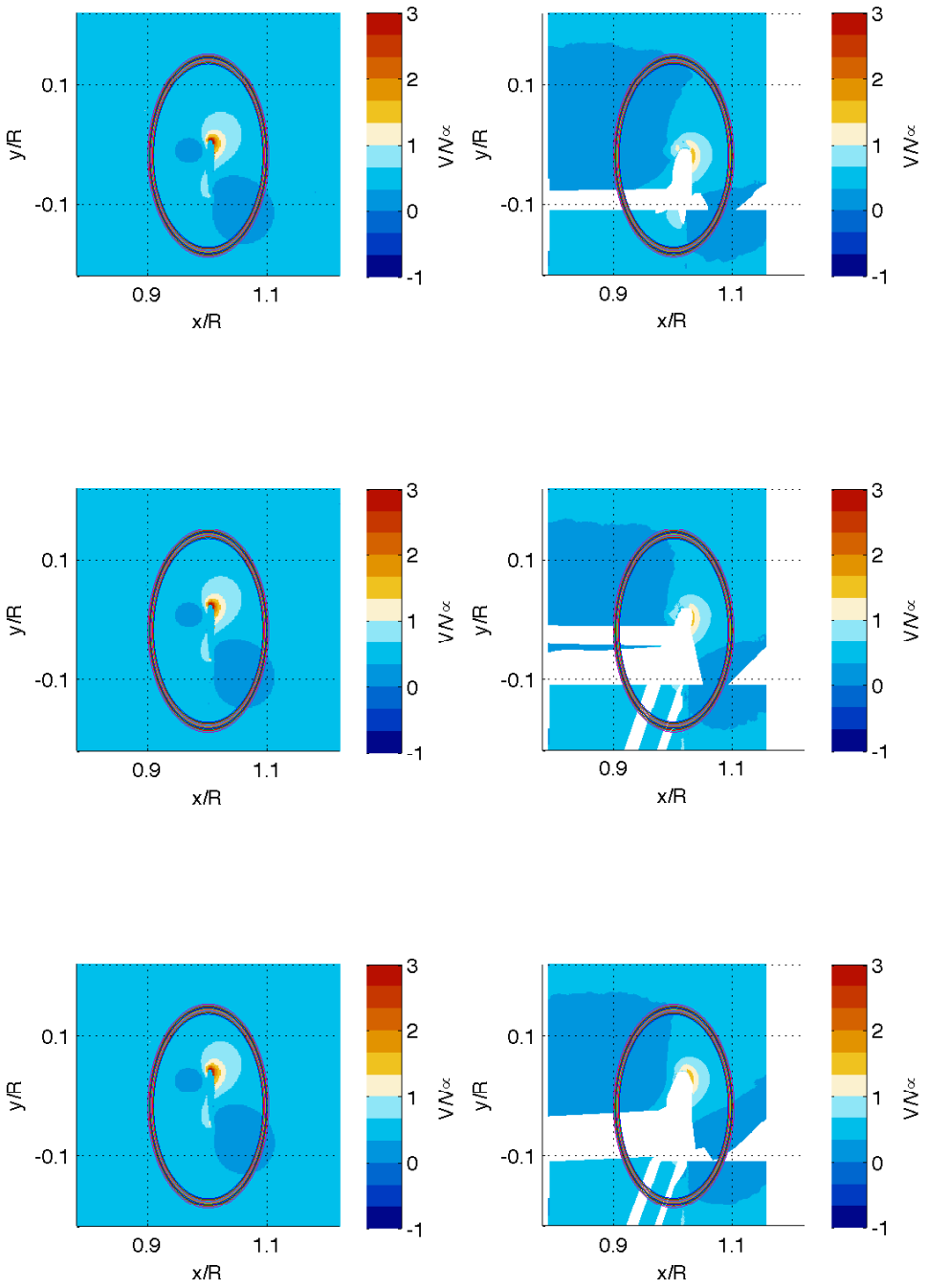

Figure D.6: *The numerical flow fields (left) and the experimental flow field (right) for TSR 4.5 at* $\theta = 270°$.

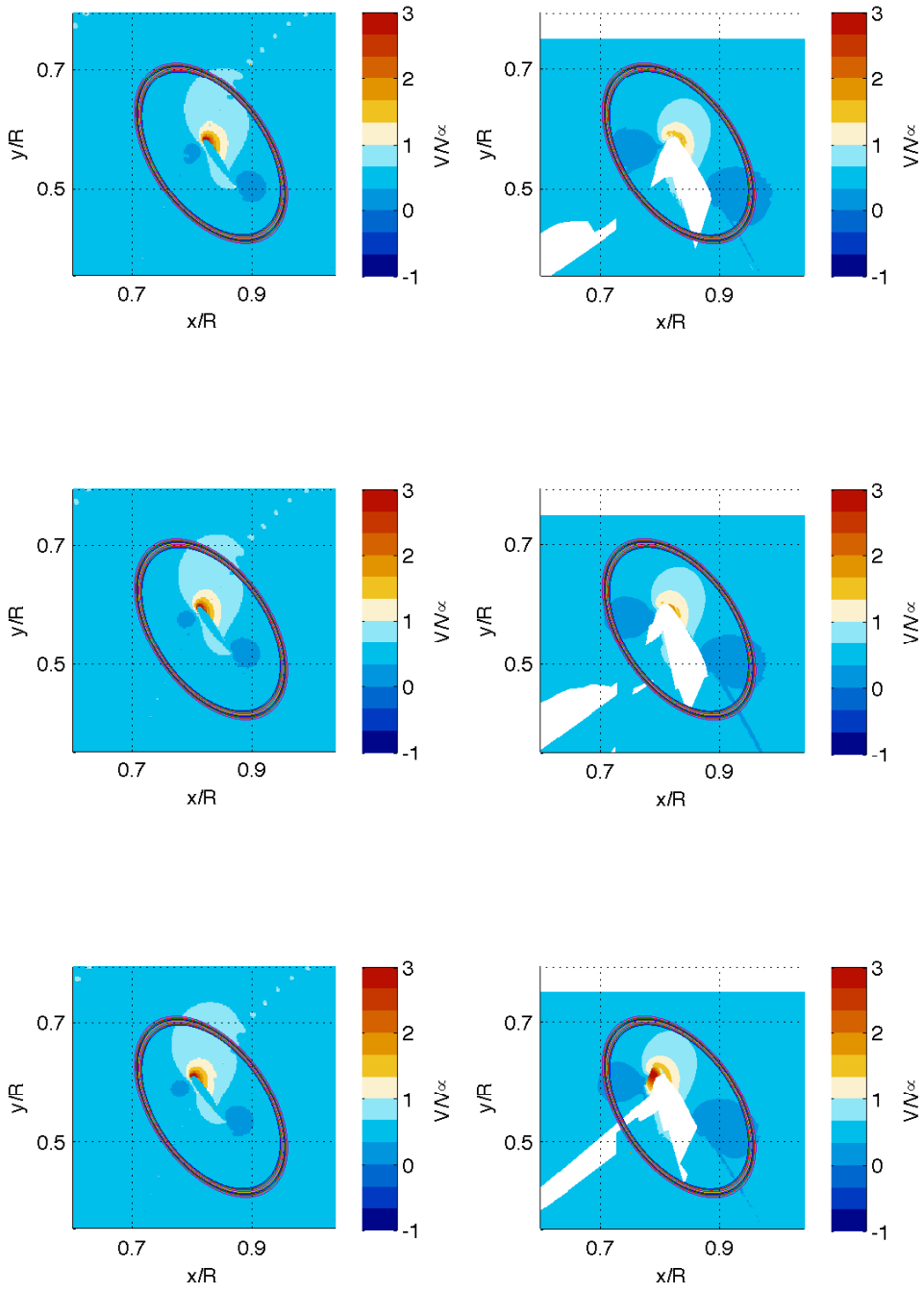

Figure D.7: *The numerical flow fields (left) and the experimental flow field (right) for TSR 4.5 at* $\theta = 305°$.

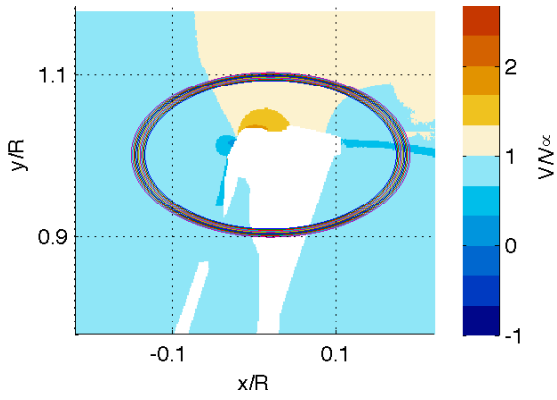

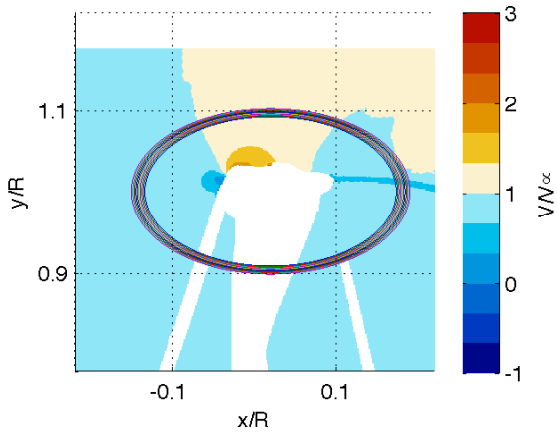

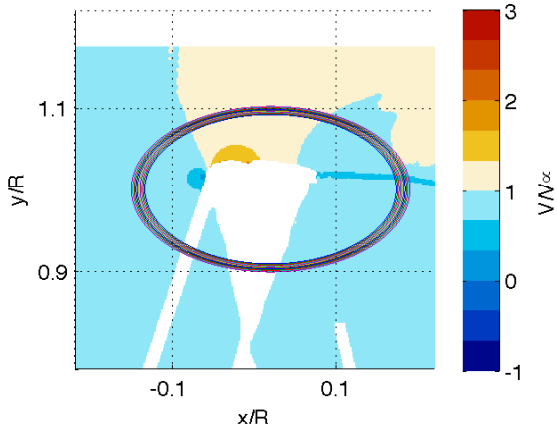

Figure D.8: *The experimental flow field for TSR 2 at $\theta = 0°$.*

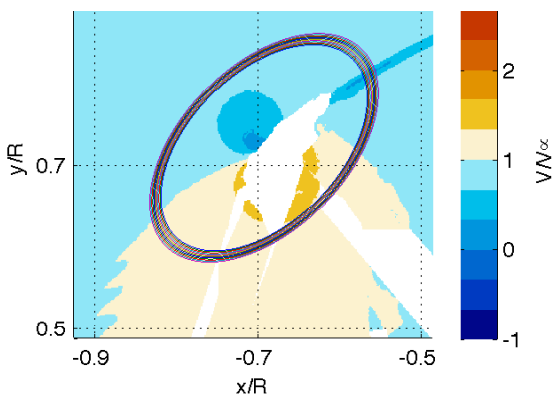

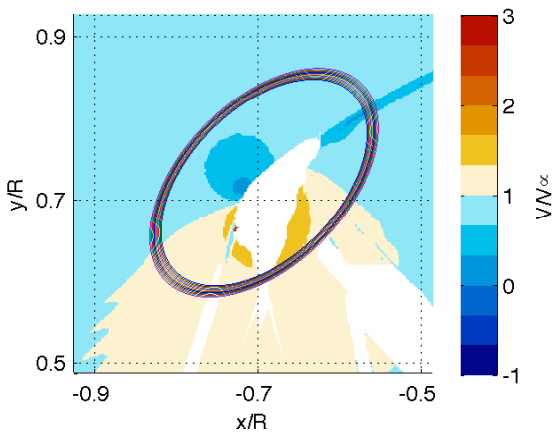

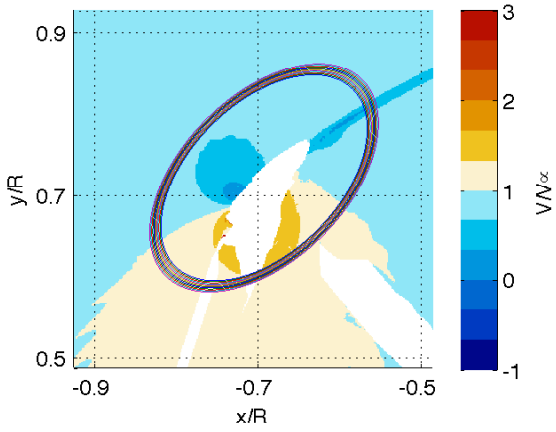

Figure D.9: *The experimental flow field for TSR 2 at $\theta = 45°$.*

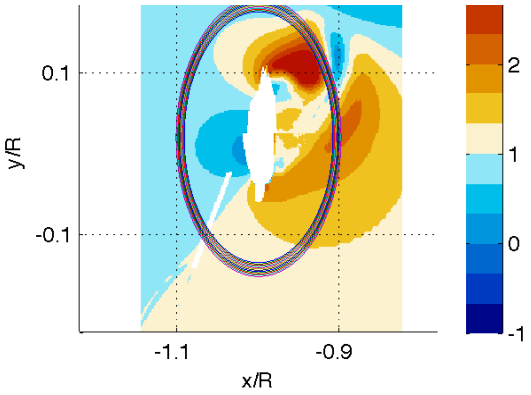

Figure D.10: *The experimental flow field for TSR 2 at $\theta = 90°$.*

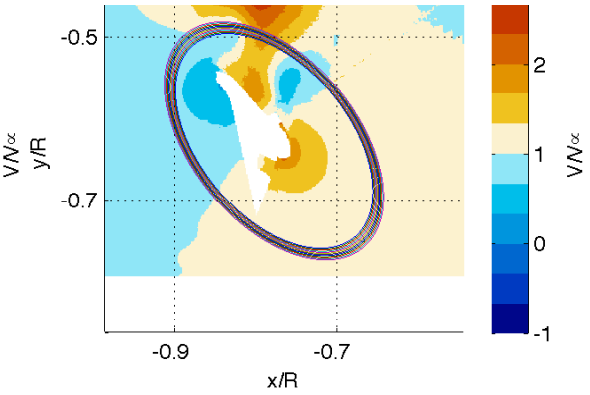

Figure D.11: *The experimental flow field for TSR 2 at $\theta = 130°$.*

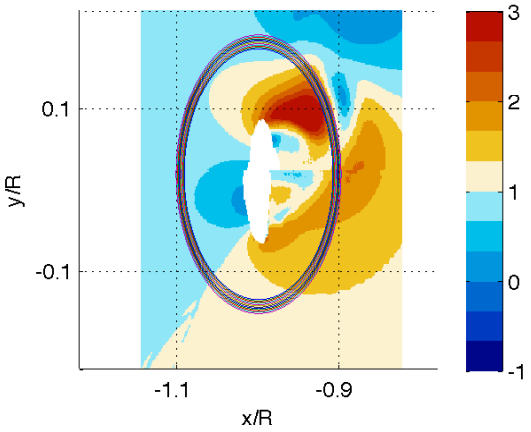

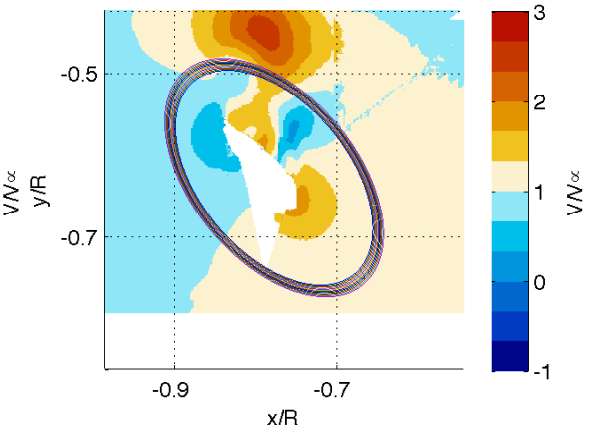

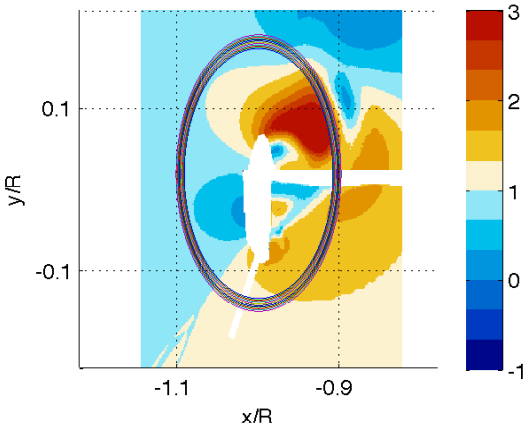

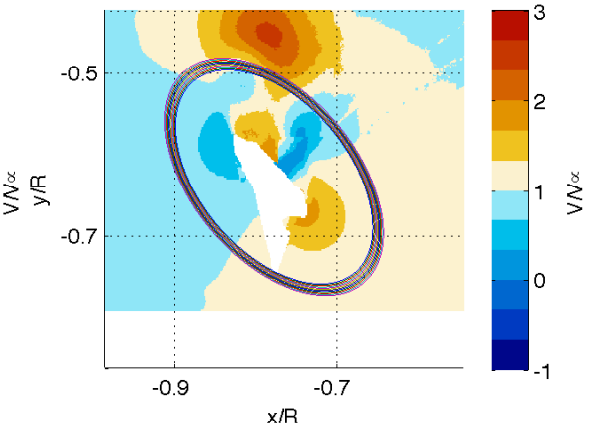

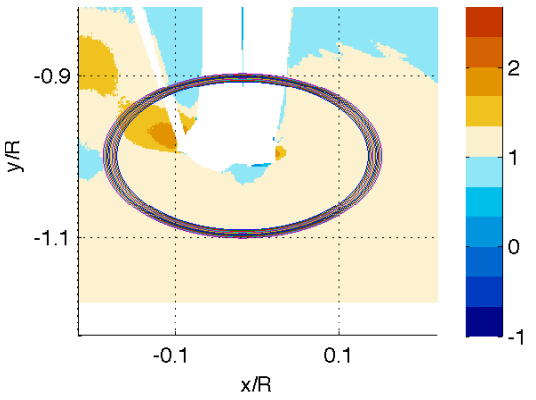

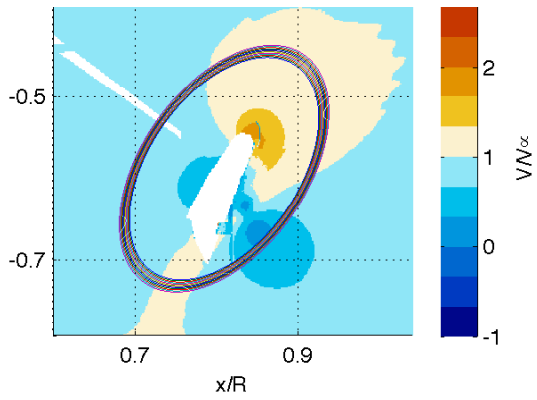

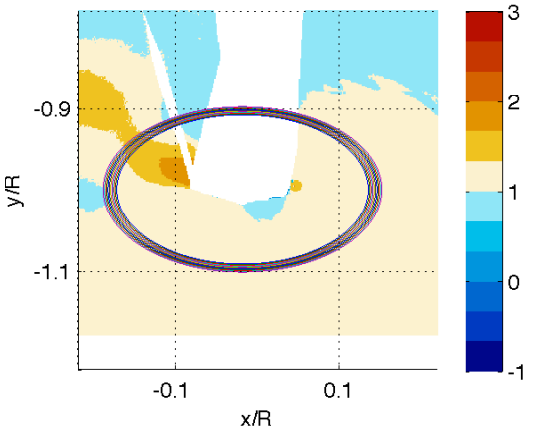

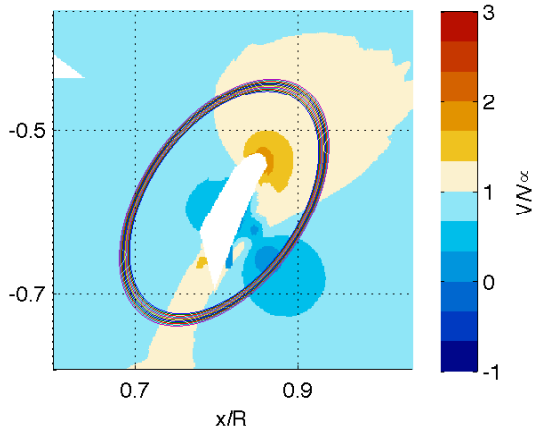

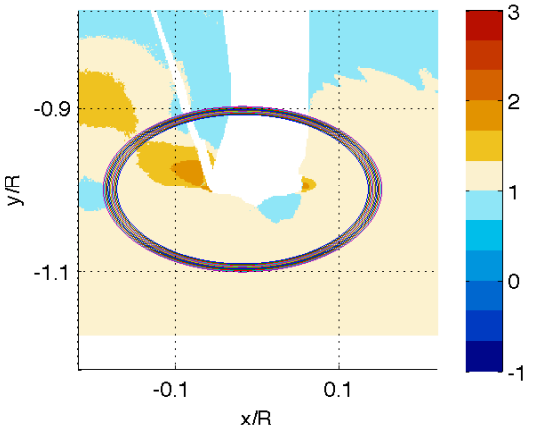

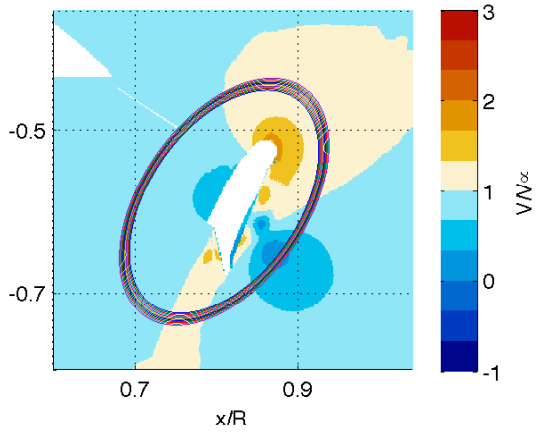

Figure D.12: *The experimental flow field for TSR 2 at* $\theta = 180°$.

Figure D.13: *The experimental flow field for TSR 2 at* $\theta = 235°$.

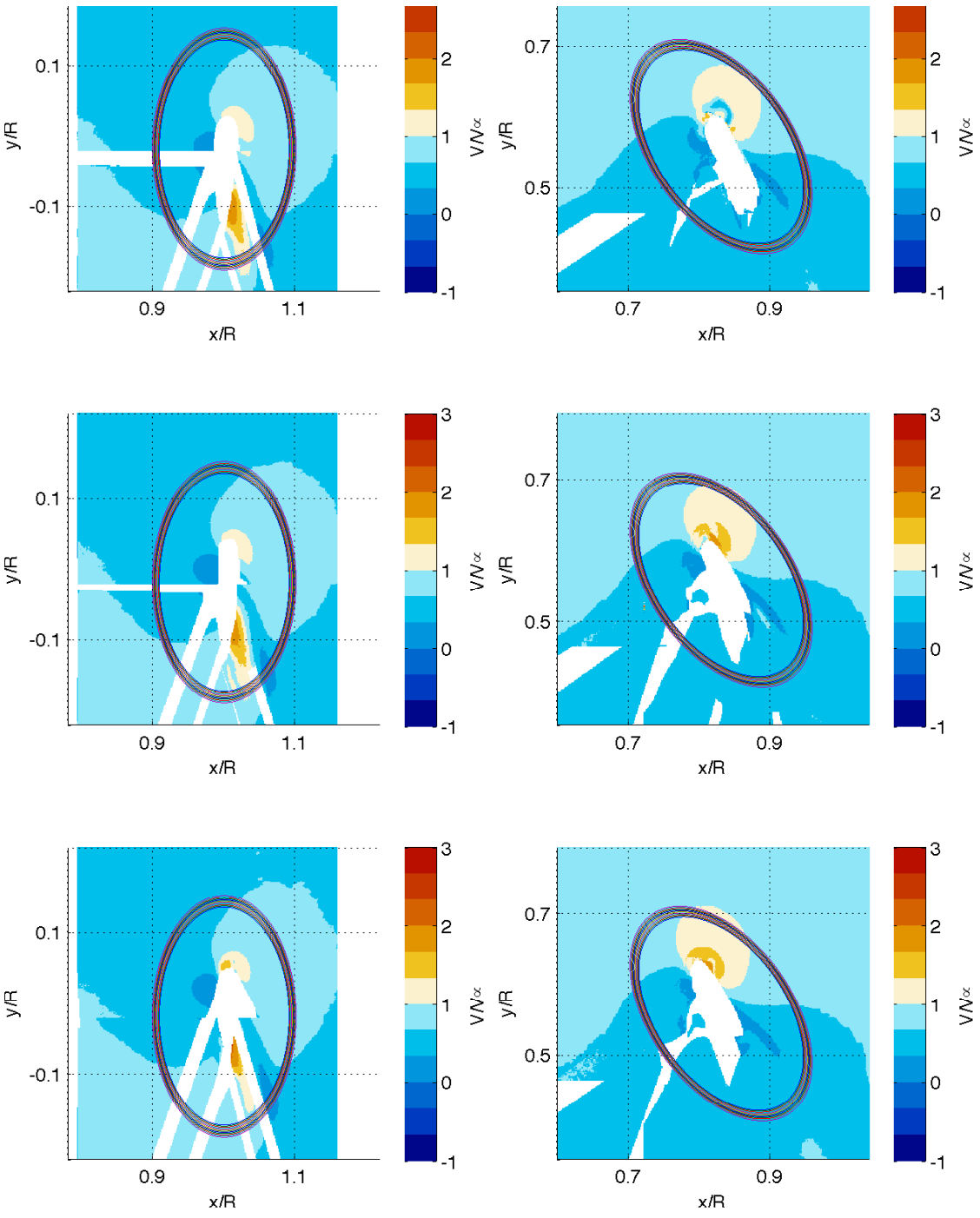

Figure D.14: *The experimental flow field for TSR 2 at $\theta = 270°$.*

Figure D.15: *The experimental flow field for TSR 2 at $\theta = 305°$.*

APPENDIX E

EXPERIMENTAL RESULTS

In this appendix the loads are presented that were calculated with the different contours according to the method described by Noca et al. [28]. In Table E.1 all the results are presented for both: the inertial reference frame, and the moving reference frame described in Section 4.5.6.

Table E.1: *Load results of the experiment for both TSR cases, in the inertial and moving reference frame.*

		TSR 4.5				**TSR 2**			
		Inertial frame		**Moving Frame**		**Inertial frame**		**Moving Frame**	
	θ [°]	mean	var	mean	var	mean	var	mean	var
F_N [-]	0	0.124	0.013	0.116	0.086	-0.035	0.013	-0.035	0.026
	45	2.117	0.040	2.153	0.084	1.345	0.025	1.329	0.053
	90	2.775	0.020	2.786	0.054	0.304	0.138	0.146	0.192
	130	0.709	0.441	0.755	0.498	0.387	0.017	0.230	0.145
	180	-	-	-	-	-0.004	0.024	-0.079	0.026
	235	-0.438	0.013	-0.392	0.034	-0.497	0.013	-0.476	0.010
	270	-0.229	0.020	-0.337	0.066	-0.426	0.033	-0.446	0.022
	305	-0.281	0.011	-0.354	0.029	-0.539	0.014	-0.513	0.023
F_T [-]	0	-0.169	0.020	0.085	0.031	-0.042	0.006	-0.013	0.011
	45	-0.003	0.053	0.119	0.027	0.150	0.020	0.191	0.026
	90	0.158	0.011	0.271	0.024	0.021	0.033	0.300	0.045
	130	-0.464	0.142	-0.001	0.319	-0.039	0.013	0.013	0.045
	180	-	-	-	-	0.030	0.016	-0.031	0.023
	235	0.141	0.006	0.286	0.013	0.007	0.003	-0.046	0.006
	270	-0.103	0.009	0.164	0.023	-0.058	0.019	-0.026	0.028
	305	-0.051	0.007	0.085	0.014	0.047	0.011	0.055	0.016

APPENDIX F

AIAA CONFERENCE PAPER

The preliminary findings from this thesis were presented on the 33rd Wind Energy Symposium at the AIAA SciTech conference in January 2015 in Kissimmee, Florida. The full paper can be found in this appendix.

AIAA SciTech
5-9 January 2015, Kissimmee, Florida
33rd Wind Energy Symposium

Creating a benchmark of Vertical Axis Wind Turbines in Dynamic Stall for validating numerical models

D. Castelein*, D. Ragni*, G. Tescione*, C.J. Simão Ferreira*, M. Gaunaa**
*TUDelft, Kluyverweg 1, 2629HS Delft, The Netherlands.
**DTU, Anker Engelunds Vej 1 Bygning 101A, 2800 Kgs, Denmark.

An experimental campaign using Particle Image Velocimetry (2C-PIV) technique has been conducted on a H-type Vertical Axis Wind Turbine (VAWT) to create a benchmark for validating and comparing numerical models. The turbine is operated at tip speed ratios (TSR) of 4.5 and 2, at an average chord-based Reynolds number of $1.6e^5$ and $0.8e^5$. At both TSR, the velocity fields are presented in the mid (symmetry) plane of the blade for eight azimuthal positions. The velocity fields are directly derived from PIV, while the loads are obtained through an integral approach presented by Noca et al. The experimental data of the velocity fields around the airfoil and the loads on the blade are used for numerical validation. The aim of evaluating the two different TSR is identifying the effect of Dynamic Stall (DS), which is not present at the higher TSR, while dominant at the lower. The DS phenomenon is numerically very hard to model, so a solid benchmark for a VAWT in DS is of great interest. The aim of the paper is to present the experimental flow fields, and the validated loads on the blades for both TSR.

Nomenclature

Greek Symbols

θ	azimuthal Angle,°
ρ	Density, $\frac{\text{kg}}{\text{m}^3}$

Latin Symbols

F	Force, N
R	Radius, m
c	Chord, m

Abbreviations

AoA	Angle of Attack
BEM	Blade Element Momentum
CCD	Charge-coupled Device
CG	Centre of Gravity
$DMST$	Double Multiple Stream tube
DS	Dynamic Stall
FOV	Field of View
$HAWT$	Horizontal Axis Wind Turbine
OJF	Open Jet Facility
PIV	Particle Image Velocimetry
TSR	Tip Speed Ratio
$VAWT$	Vertical Axis Wind Turbine
$2C-PIV$	Two-Component standard Particle Image Velocimetry

I. Introduction

Recent developments in the wind energy sector identify a potential cost reduction for offshore applications with Vertical Axis Wind Turbines (VAWT). Compared to Horizontal Axis Wind Turbines (HAWT), VAWT possess higher potentials for scalability,[18] a simpler design and maintenance with no yaw or pitch mechanisms and a lower center of mass, with the generator not constrained on top of the tower (seen in Figure 1). The reduced maintenance costs and the possibility to displace the electric generator under water are of major interest in floating offshore applications.[12] Moreover some previous studies on VAWT[13] hypothesised a faster wake recovery, leading to a reduction of the turbine spacing and more clustered arrays in a wind farm scenario.

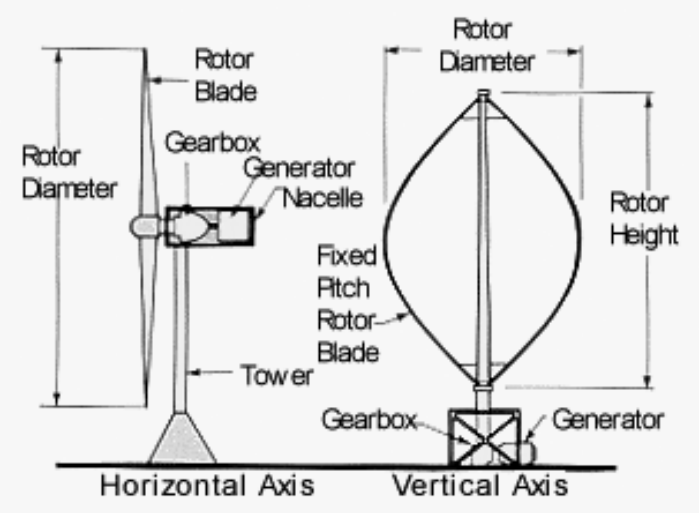

Figure 1. Benefits of a VAWT.

In order to supply the growing interest and questions of VAWTs, there is a need for more accurate numerical models. This can only be achieved by validating those numerical models on experimental data, and therefor as many different experimental cases are required. The emphasis of this experiment lies on dynamic stall, thus especially a low TSR is investigated (TSR 2).

Previous experimental work on the effect of dynamic stall on VAWT analysed the rotor from a performance point of view (power and loading, see Laneville and Vittecoq[1]) or using flow visualisation techniques without quantification of the flow (see Brochier et al.[10]). Fujisawa and Shibuya[14] and Fujisawa and Takeuchi[15] developed a first attempt at flow field measurements of a Darrieus using PIV at Reynolds numbers Re = 3000 and Re = 1000 (water flow).

In the last decade Paraschivoiu[17] compared experimental measurements of the average 2D induction field with prediction models, which poorly estimated the wake energy recovery. On the computational side, most of the numerical models are based upon actuator disk and stream tube models, which have been adapted from the Horizontal Axis Wind Turbines (HAWT) field, not entirely addressing the underlying physics of a VAWT, especially not when DS occurs.[8]

Simão Ferreira[7] visualised the flow around a VAWT by means of PIV. This was done for TSRs of 2, 3 and 4 with $Re = 5e^5$ & $7e^5$. This research focussed on visualising the vortex shedding and vortex roll-up occurring due to dynamic stall. Therefor only flow fields from the upwind to the leeward position of the turbine were presented. Also, in this research there was no force extracted on the blade from this experimental data.

Later research of Simão Ferreira[8] compared CFD simulations with the experiment conducted in previous research.[7] This was done in order to validate which model simulated the experiment best in terms of shed

vorticity. This was found to be the DES (Detached Eddy Simulation) model. In this research, loads on the blades were also not evaluated.

This paper will present velocity fields at eight azimuthal positions for a VAWT at TSRs 4.5 and 2 . These velocity fields will be made publicly available for future research on DS. This paper will also present the force acting on the blade for those fields, calculated with the force calculation method by Noca et al.,[9] as proposed by Simão et al.[6] These loads are also made publicly available for the validation of numerical models.

II. Methodology

A. System of reference and conventions

To make the presentation and the following discussion on the results easier to follow, some common terminology has to be defined. Following the work of Simao Ferreira[5] and Tescione et al.,[11] the blade orbit is divided in 4 regions:

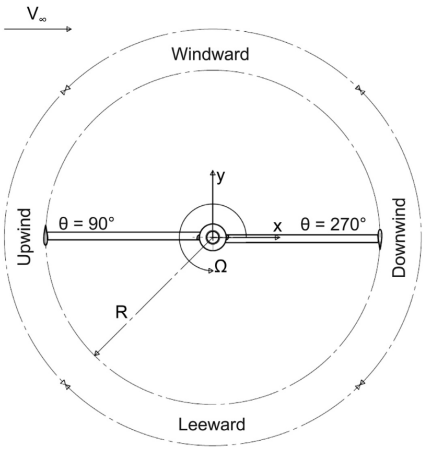

- upwind: $45° < \theta < 135°$;
- leeward: $153° < \theta < 225°$;
- downwind: $225° < \theta < 315°$;
- windward: $315° < \theta < 45°$;

Figure 2. Schematic of the blade motion on a vertical axis wind turbine.[11]

Here, θ is the blade azimuthal position and $\theta = 0°$, $90°$, $180°$ and $270°$ are respectively the most windward, upwind, leeward and downwind positions, as seen in Figure 2. The adopted division refers to the blade orbit. The coordinate system is a Cartesian frame with origin at the turbine center; x-axis directed positively downwind the turbine, positive y-axis pointing to the windward side and z-axis positive upwards. A positive rotation of the turbine is counter clockwise seen from the top.

B. Experimental Set-Up

1. VAWT Model

The model employed in this study is a two-bladed H-type VAWT with radius (R) 0.5 m and height 1.0 m. The blade profiles are NACA0018 with a chord of 6 cm. The boundary layer of the airfoil has been forced to turbulent transition by applying a 3D-turbulator tape developed by Glasfaser Flugzeug (6 mm point distance, 0.20 mm thick, 12 mm width, 60° zig- zag tape) at 8% of the chord, as prescribed in.[19,20,11] The blade-tower connection is obtained with two aerodynamically profiled struts (NACA0030, chord 23mm) per blade, installed at 200mm from the blade tips. The location of the connections is meant to minimise the maximum deformation at blade mid-span and blade tips due to centrifugal effects. The strut-blade connection has been shaped to minimise the flow interference.[11] The model is presented in Figure 3.

The turbine is supported by a 3m steel shaft, connected to a Faulhaber® brushless DC motor used as generator and to monitor the rpm of the turbine. The maximum output power of the motor is 202W,

delivered through a 5:1 gearbox system, allowing for driving the transitory regimes of the turbine to the operating speed. On the shaft a 1-pulse encoder is installed to allow phase locking of the measurement with the azimuthal position of the blade.

2. *Open Jet Wind Tunnel Facility*

The PIV experiments have been performed in the Open Jet wind tunnel Facility (OJF) of TU Delft. The OJF is a closed-circuit, open-jet wind tunnel with an octagonal cross-section of 2.85 x 2.85$[m^2]$ and a contraction ratio of 3:1. The tunnel jet is free to expand in a 13.7 x 6.6 x 8.2$[m^3]$ test section. Driven by a 500 [kW] electric motor, the OJF delivers free stream velocity range from 3$[\frac{m}{s}]$ to 34$[\frac{m}{s}]$ with a flow uniformity of $\pm$0.5[%] and a turbulence level of 0.24[%].[2] A 350 kW heat exchanger maintains a constant temperature of 20$[^\circ C]$ in the test section. A schematic of the wind tunnel is shown in Figure 4.

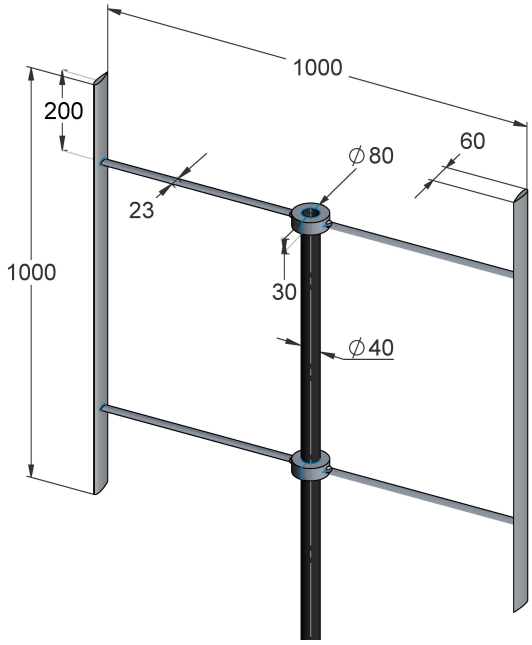

Figure 3. The VAWT Model.

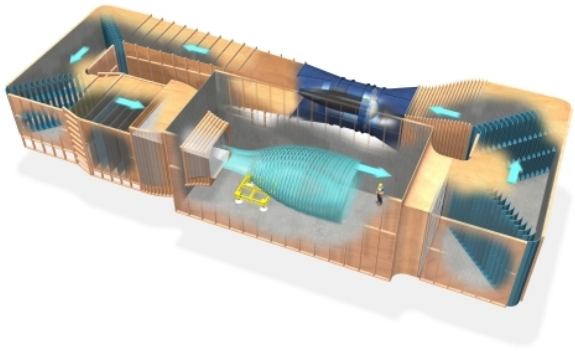

Figure 4. Schematics of the OJF.[2]

3. *Flow Regimes*

The tests are done for two different tip speed ratios and Reynolds number. The operating conditions for both TSRs are given in Table 1.

Table 1. Operating conditions for both tip speed ratios.

Tip Speed Ratio [-]	Free Stream Velocity$[\frac{m}{s}]$	Averaged Chord based Reynolds Number [-]
4.5	9.1	160000
2	10.2	80000

4. *PIV Set-Up*

Two-component standard Particle Image Velocimetry (2C-PIV) measurements are acquired at the mid-span of the turbine at two different tip-speed ratios. Laser illumination is provided by a Quantel Evergreen® laser, by forming a laser sheet of about 30[cm] width and 2[mm] thickness. In order to reduce laser shadows the beam is first split and then recombined into a unique laser sheet (Figure 6). The entire PIV set-up (laser, turbine, wind tunnel) can be seen in Figure 5.

In Figure 6 the shadows of both sheets can be seen. Although these shadows are compensated by the light of the other sheet, there is still a small area behind the blade that is not illuminated. Theoretically, this is the only blind spot that will exist. In this area no particles can be captured, and thus no velocity components can be found. This is why these areas should be minimised.

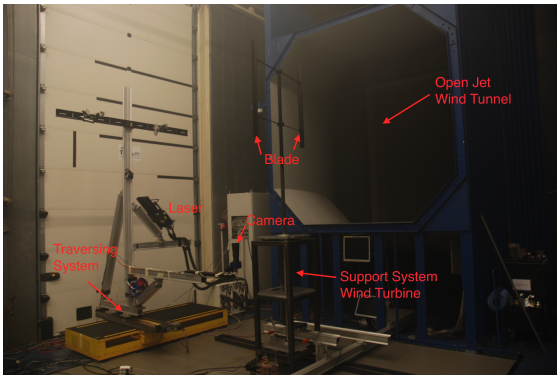

Figure 5. The Set-Up for the PIV System.

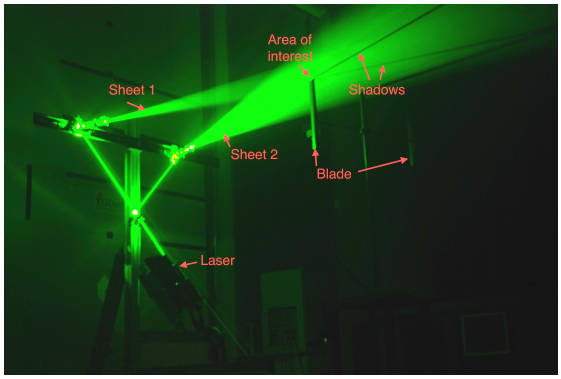

Figure 6. The Set-Up for the laser.

The accuracy of the phase locking is usually an important source of error in similar experiments. From the experimental data it is possible to conclude that any oscillation of the phase locking azimuthal angle of the different samples is imperceptible and much smaller than the uncertainty of the actual value of the phase locking azimuthal angle, estimated at $\pm 0.03°$. This oscillation is the result of variations during the rotation of the aerodynamic torque and reaction of the controller for torque at the generator. This low level of uncertainty in the azimuthal position can be considered as negligible.

The bias associated with the angle of attack of the blade (due to uncertainty in the definition of zero position and due to blade bending), was estimated at a maximum of $\pm 0.25°$, based on observations at the most upwind position of the rotation.

5. *Acquisition & Processing*

Images are obtained by a LaVision Pro LX CCD camera with 4872x3246 pixel and 7.4[m] pixel pitch, positioned perpendicularly beneath the mid section of the turbine blade. A combination of two to four positions per field of view was employed to fill the area of the lower strut by exploiting the prospective view of the camera (Figure 7). Both laser and camera were installed on a traversing mechanism, as seen in Figure 5.

In Figure 15 all the acquisition positions are displayed for both TSR cases. For two positions only two pictures were taken: 90 and 270 [°]. Here the blade and strut chord are parallel to the long axis of the FOV. Only two pictures are needed to capture the entire field around the blade and still remove the lower strut. In Figure 15 all the measuring positions with the corresponding number from Table 2, can be seen. All the acquisition positions are expressed in both the turbine and the camera reference frame in Table 2.

LaVision® Davis software was used the process the images captured by the camera, to a velocity field. These field were imported in MATLAB® to stitch all the individual field from Figure 15 to one entire field.

Figure 7. More Camera Positions are used to Remove the Lower Strut in the stitched Velocity Field.

Reflections, errors, and shadows in these fields were removed as much as possible.

C. Noca Force Calculation Method

From the resulting velocity fields different methods are used to compute the pressure fields and, by integration, the forces around the blade. The methods rely on the direct use of the velocity in an unsteady Bernoulli equation[4] or by the use of the vorticity.[3] By integrating these quantities along contours around the blade the forces can be derived with the Noca-method.[9]

The force per unit unit density can be calculated with Equation 1. The representation of this equation is shown in Figure 8.

$$\begin{aligned}\frac{F}{\rho} =& -\frac{\mathrm{d}}{\mathrm{d}t}\int_{V_{(t)}} u\mathrm{d}V \\ &+ \oint_{S_{(t)}} \hat{n}.\left[-\frac{p}{\rho}\vec{I} - (u-u_S)u + T\right]\mathrm{d}S \\ &- \oint_{S_{b(t)}} \hat{n}.\left[(u-u_S)u\right]\mathrm{d}S\end{aligned} \tag{1}$$

Where T is the viscous stress tensor (Equation 2).

$$T = \mu(\nabla u + \nabla u^T) \tag{2}$$

In Equation 1 two terms will pose problems: one being the velocity integral over the entire integration area ($\mathrm{d}V$) and the other the pressure term (p). The integration over the entire field can be made impossible due to shadow effects or reflections.The pressure terms are unknown, and will have to be derived. By deriving those pressure, more errors will occur in the results. This method is disregarded and another method, proposed by Noca et al.,[9] is used to calculate the force on the blades, as proposed by Sim ao et al.[6]

The Noca et al.[9] method uses a Flux Equation formulation seen in Equation 3.[16] The representation of

this equation is shown in Figure 9.

$$\begin{aligned}\frac{F}{\rho} =& + \oint_{S_{(t)}} \hat{n} \cdot \gamma_{flux} \mathrm{d}S \\ & - \oint_{S_{(t)}} \hat{n} \cdot [(u - u_S)u] \, \mathrm{d}S - \frac{\mathrm{d}}{\mathrm{d}t} \oint_{S_{b(t)}} \hat{n} \cdot (ux) \mathrm{d}S\end{aligned} \tag{3}$$

With the flux term (γ_{flux}), shown in Equation 4.[16]

$$\begin{aligned}\gamma_{flux} =& \frac{1}{2}u^2\vec{I} - uu - \frac{1}{N-1}u(x \times \Omega) + \frac{1}{N-1}\Omega(x \times u) \\ & - \frac{1}{N-1}\left[(x \cdot \frac{\partial u}{\partial t})\vec{I} - x\frac{\partial u}{\partial t} + (N-1)\frac{\partial u}{\partial t}x\right] \\ & + \frac{1}{N-1}\left[(x \cdot (\nabla \cdot T)\vec{I} - x(\nabla \cdot T)\right] + T\end{aligned} \tag{4}$$

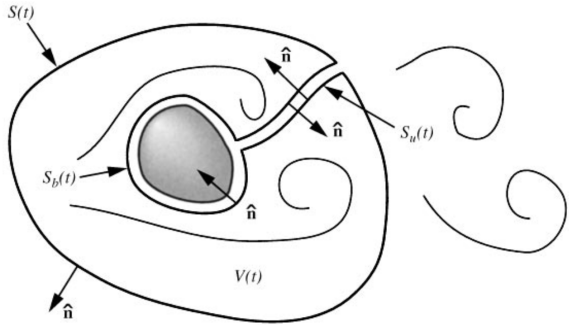

Figure 8. Control volume analysis.[9]

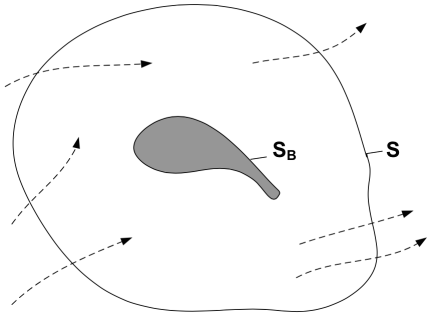

Figure 9. Representation of the control volume bounded by the outer contour S and the body contour S_B.[5]

As can be seen in Equation 3 & 4, the pressure term as seen in Equation 1 has vanished due to the use of the vorticity. Since the vorticity can be directly calculated from the velocity field, less errors will occur with this method. The inputs this model needs are:

- X-Y Coordinate
- Velocity vector ($[VxVy]$)
- The flow acceleration ($[\frac{\partial U}{\partial t}\frac{\partial V}{\partial t}]$)
- Density (ρ), viscosity (μ)

All the inputs, except for the acceleration terms ($\frac{\partial U}{\partial t}\frac{\partial V}{\partial t}$), came directly from the experiment post-processing. For the acceleration term, for every azimuthal position (A) seen in Table 2 also the angles $A + -1°$ are taken. The acceleration terms are computed with Equation 5.

$$\begin{aligned}\frac{\partial U}{\partial t} &= \frac{(U_{A+1} - U_{A-1})}{2 \cdot \mathrm{d}t} \\ \frac{\partial V}{\partial t} &= \frac{(V_{A+1} - V_{A-1})}{2 \cdot \mathrm{d}t}\end{aligned} \tag{5}$$

With dt being the time it takes the blade to travel 1°.

Since more positions have been used to calculate this acceleration term, more "bad" regions with lost velocity components will exist. to minimise the error, it was opted to remove all the regions from the corresponding fields from all three azimuthal angles when calculate the acceleration terms to derive the force.

1. Error in choice contour

When choosing a contour for the evaluation of the forces according to Noca et al.[9] it could be that due to an error in the velocity field (shadow, blind spot, bad post-processing) there is an offset between the calculated force and the actual force acting on the blade. These areas are presented in Figures 16 - 25 by the blue lines. Over these areas, the velocities are interpolated. This interpolation can add an uncertainty in the force calculation.

To compensate, multiple contours are evaluated on each velocity field. The mean and standard deviation are calculated with the results, and presented in the graphs by a circle and a line accordingly.

2. Validating Noca-method

To validate the Noca method,[9] the velocity fields are retrieved from the inviscid panel model developed by Simão Ferreira.[5] This simulation was modelled for a TSR of 4.5 with a solidity of 9.5, to compensate for the in-viscosity[5] of the numerical model. The forces extracted from the model, are presented by the cyan line in Figure 10. They will be used as a reference for the validation of the Noca method.

Since there are a lot of regions where the velocities in the fields are unknown, the only option is interpolating over these region. To be sure this interpolation works correctly, the areas that were masked due to reflections and shadows in the experiment, are also masked in the numerical fields. If the Noca method is implemented correctly and the interpolation over the masked regions is working correctly, the Noca method should give the same forces as the numerically calculated panel model forces.

To get an idea of the contours, one of the Noca method[9] contours is visualised on the velocity field in Figure 16 by the yellow line. The resulting mean force, and its standard deviation can be seen in Figure 10 in green.

In Figure 10 in green, the results of the Noca method are shown, and they are matching well with the panel model results. It can be accepted that the Noca method is correctly implemented, that the interpolation is working well, and that this method can be used to calculate the forces of the experiment.

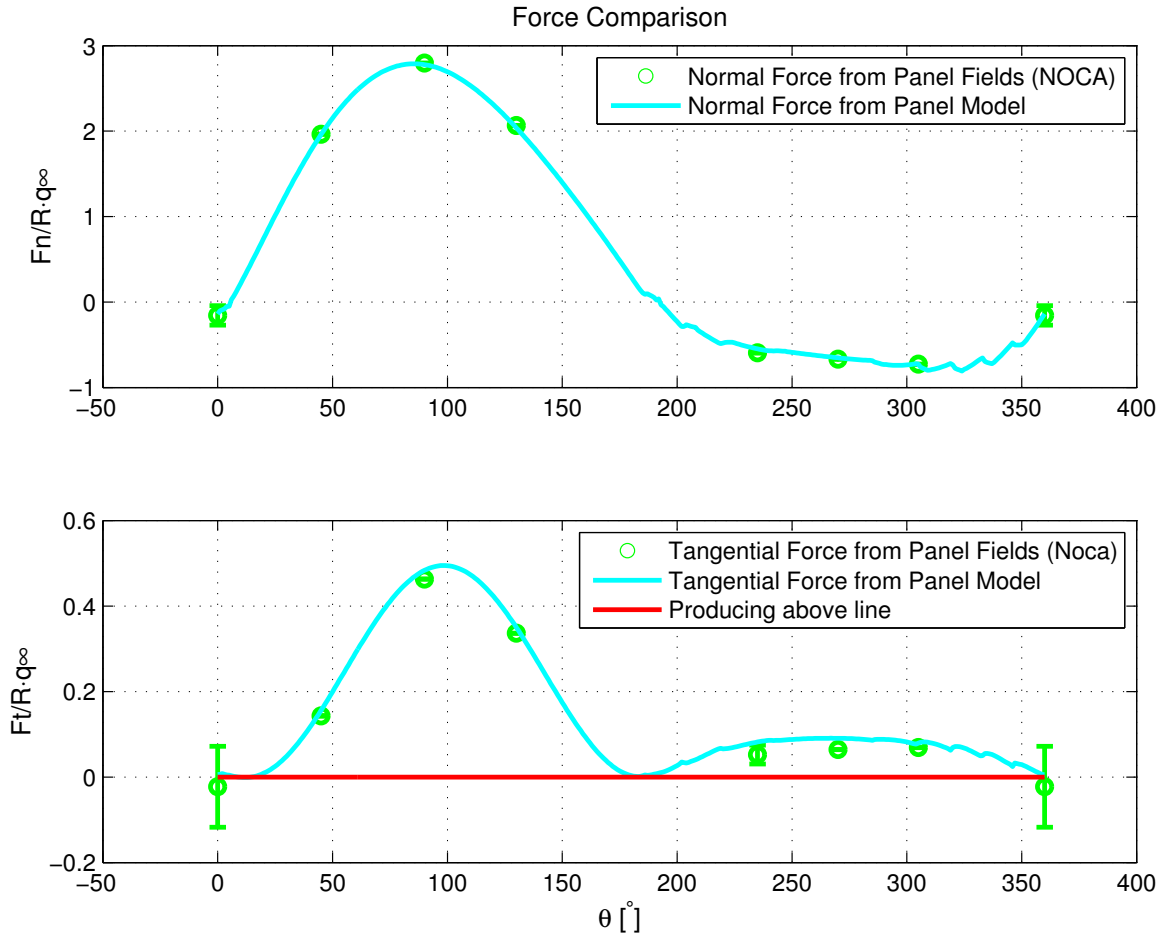

Figure 10. The Validation of the force calculation method according to Noca et al.[9] on results from the inviscid panel model by Simão Ferreira[5] at TSR 4.5 and solidity of 9.5, to compensate for the in-viscosity.

III. Results

A. Velocity Fields

In Figure 11 the velocity fields for TSR 4.5, and in Figure 12 the velocity fields for TSR 2 of the experiment can be seen. Here the velocities are non-dimensionalised by the free stream velocity ($\frac{V}{V_\infty}$). The coordinates are non-dimensionalised with the radius ($[\frac{X}{|R|}\ \frac{Y}{|R|}]$), and the forces by $q_\infty \cdot R$ ($\frac{F}{\frac{1}{2}\rho V_\infty^2 \cdot R}$).

For both TSR (Figure 11 & 12) it can be seen that the turbine is slowing down the stream. The velocities downwind are much lower than the velocities upwind, which proves that energy is extracted from the flow.

In the windward position (close-up in Figure 16) the wake from the previous blade, as well as from 2 passages before, can be seen in this field. Comparing this to the panel code field in Figure 17 the experimental and numerical simulations present a similar wake convection.

A close-up from the most upwind positions is also given for TSR 4.5 in Figure 18, as well as the numerical field for TSR 4.5 in Figure 19. The close-up for this position for TSR 2 is given in Figure 23 where the blade is clearly subjected to DS.

The downwind positions in Figure 20 and Figure 24 clearly show the wake interaction from the mast with the blade, whereas in Figure 21 this is not seen, since the mast is not modelled.

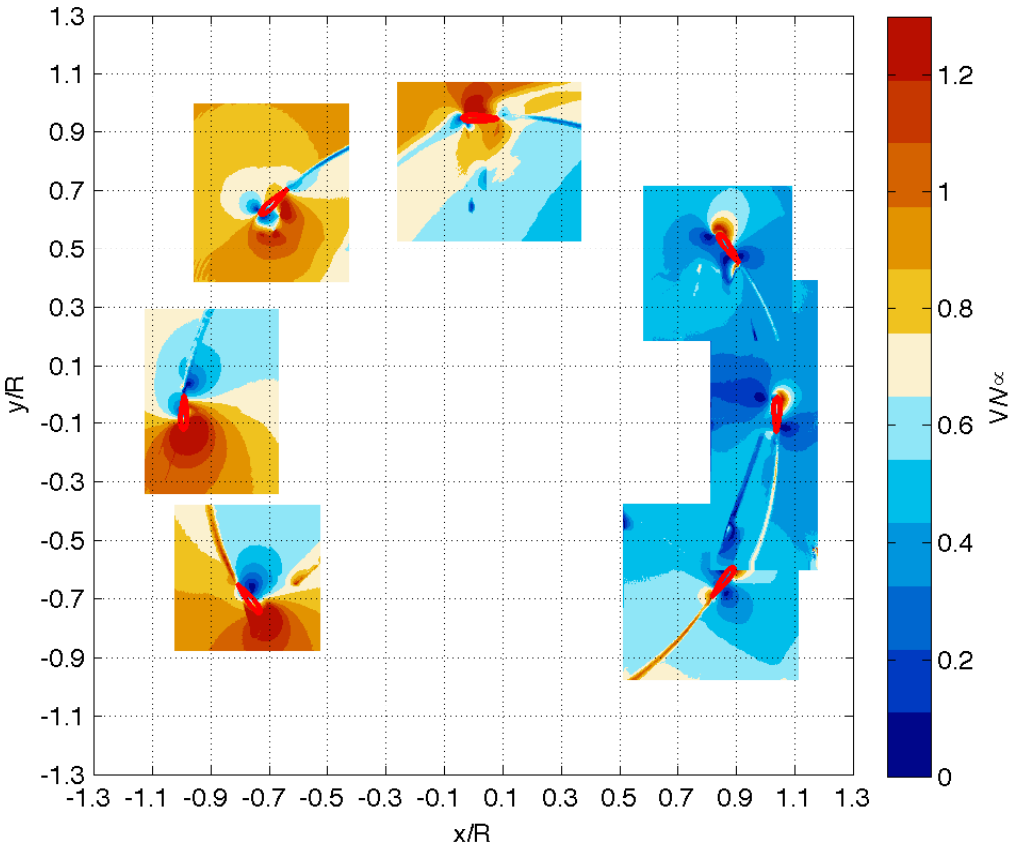

Figure 11. TSR 4.5: experimental Velocity fields.

B. Forces

The forces resulting from the experiment are seen by the blue dots in Figures 13 & 14. The dots represent the average from 12 integration contours that were taken around the blade. The line is the standard deviation difference from this averaged value.

TSR 4.5 (Figure 13):

Overall the normal force is following the trend that is expected from forces on a VAWT. The tangential force on the other hand is interesting. These forces suggest the turbine is not producing anything from leeward to almost upwind position. For reference, a turbine that is producing has a positive tangential force, and is above the red line in Figure 13.

At $\theta = 270°$ there is the wake from the mast hitting the blade. Here it can be seen that the deviation is larger, as can be expected from the turbulence coming from the mast.

The uncertainty can be said low for the normal force, but might be considered high when looking at the tangential force.

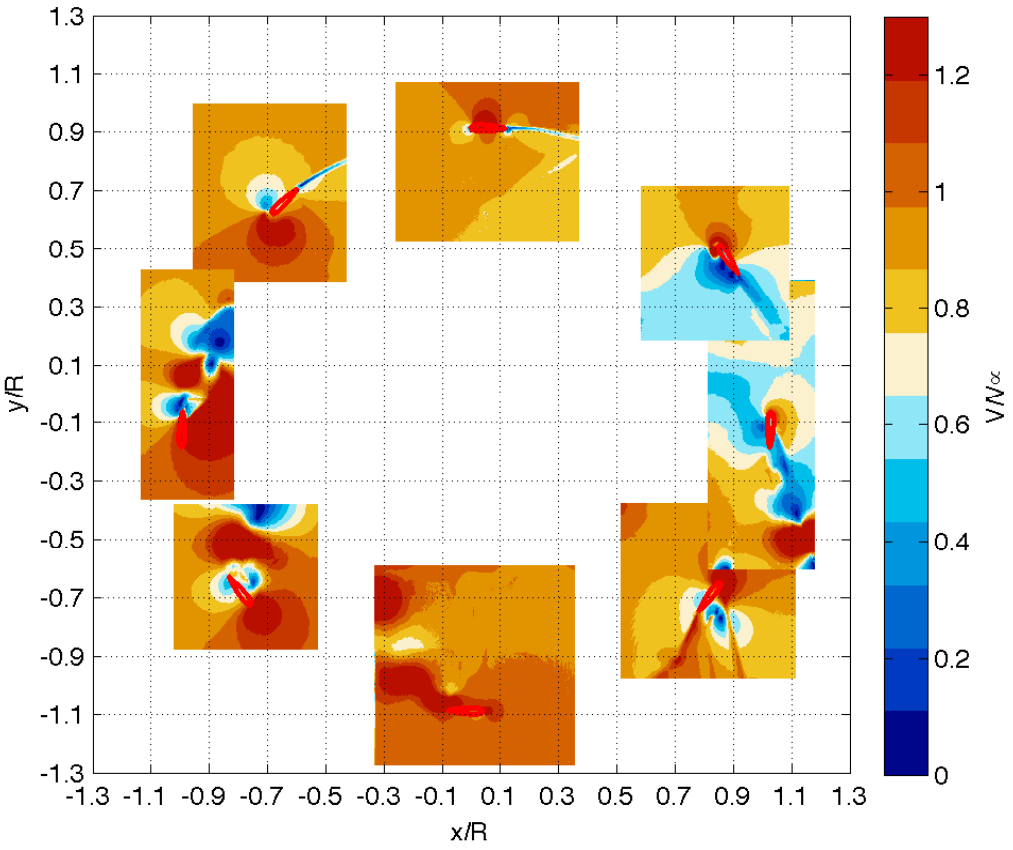

Figure 12. TSR 2: experimental Velocity fields.

TSR 2 (Figure 14):

For TSR 2 it is more difficult to asses the results of the force acting on the blade. Few research is available for commenting on the magnitude of the forces.

What can be seen, is that the forces are following the trend that can be expected when looking at the flow fields in Figure 11. At the azimuthal positions where the airfoil was said to be in stall, the airfoil is not producing, with an exception of $\theta = 180°$.

The tangential force has a big error margin compared to the TSR 4.5. This can be explained by the airfoil being mostly in stall, which makes it is harder to compute the forces acting on the blade. At $\theta = 270°$ the tangential force is again with a big error due to the mast interaction, what is also seen with at the TSR 4.5.

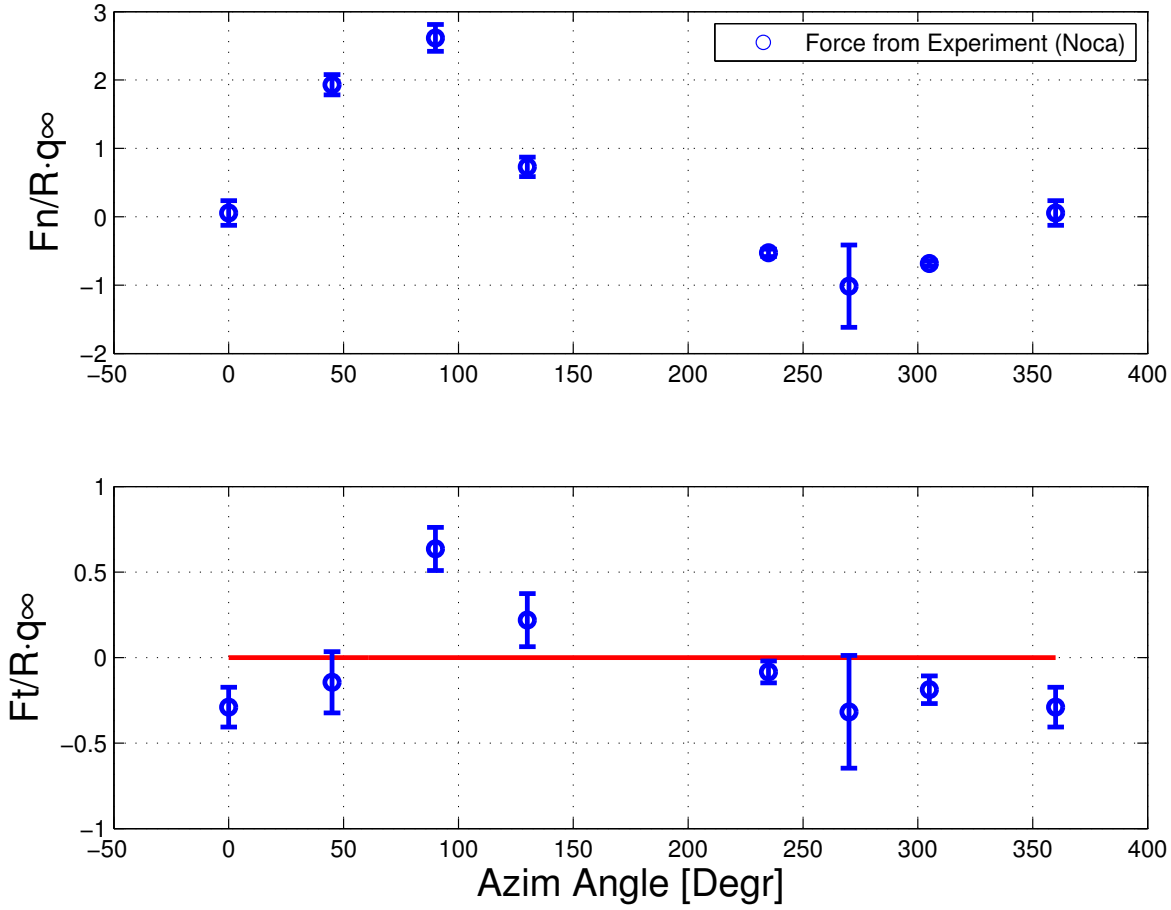

Figure 13. The difference between the forces on all the azimuthal positions for TSR 4.5.

IV. Conclusions & Recommendations

Velocity fields were presented for TSR of 4.5 and 2 for eight azimuthal positions. The normal force on the blades for TSR 4.5, extracted with the method described by Noca et al.,[9] are following the trend that is expected from the VAWT. The results for both tip speed ratio are reasonable and the approach followed in this paper is feasible. However, the uncertainty on the (tangential) forces is still high. The current level of uncertainty in the experimental data does not allow for a detailed analysis of the results. Further research will try to lower these uncertainties, by using a different post-processing method.

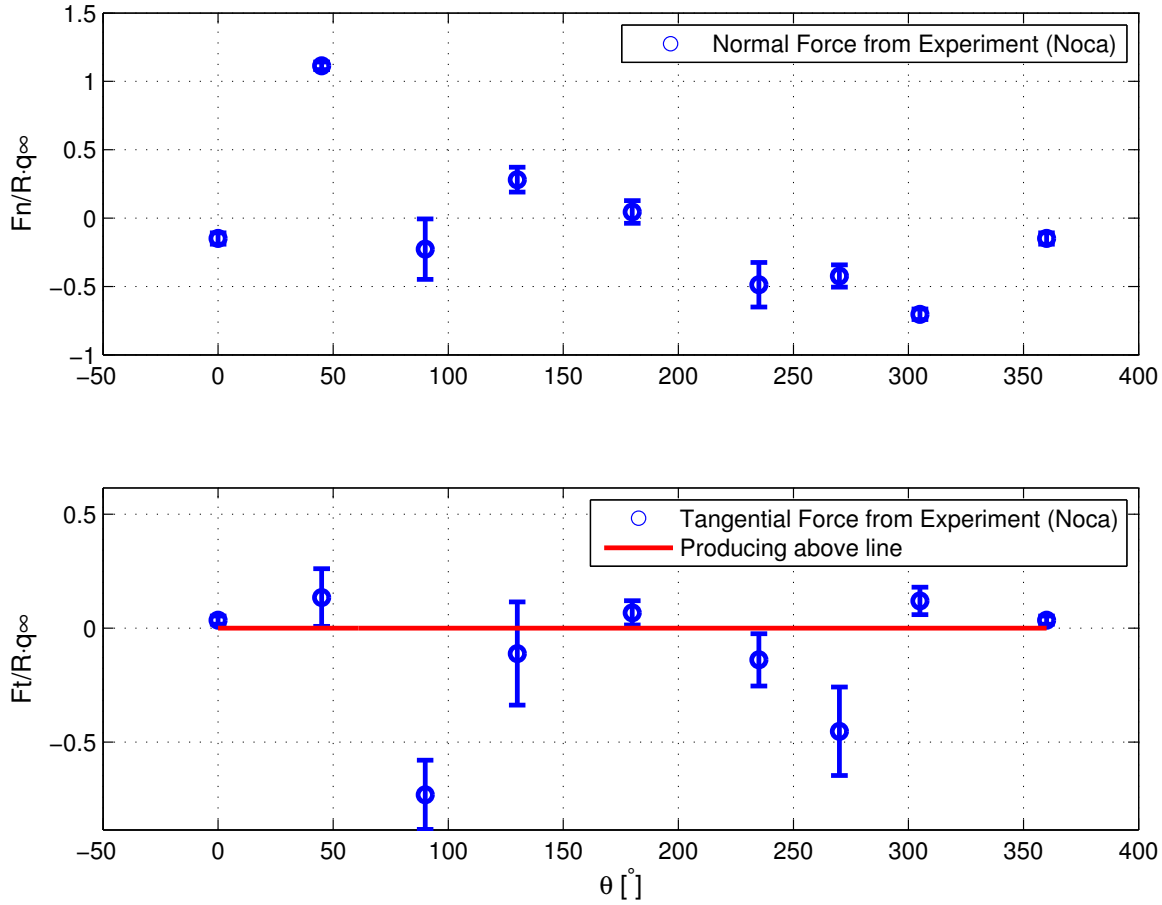

Figure 14. The difference between the forces on all the azimuthal positions for TSR 2.

References

[1]A. Laneville, P. Vittecoq. Dynamic stall - the case of the vertical axis wind turbine. *Journal of Solar Energy Engineering*, 1986.

[2]Aerodynamics Research Group. Open Jet Facility. http://www.lr.tudelft.nl/, March 2014.

[3]B W. van Oudheusden, F. Scarano, E. W.M. Roosenboom,E . W.F. Casimiri, L. J. Souverein. A comparison of methods for evaluating time-dependent fluid dynamic forces on bodies, using only velocity felds and their derivatives. Technical report, Graduate Aeronautical Laboratories, California Institute of Technology, 1999.

[4]B.W. van Oudheusden, F. Scarano, E.W.M. Roosenboom, E.W.F. Casimiri, L.J. Souverein. Evaluation of Integral Forces and Pressure Fields from Planar Velocimetry Data for Incompressible and Compressible Flows. Technical report, TUDelft, the Netherlands, 2006.

[5]C.J. Simão Ferreira. *The near wake of the VAWT*. PhD thesis, TUDelft, 2009.

[6]C.J. Simão Ferreira, G. van Bussel, G. van Kuik, F. Scarano. On the use of velocity data for load estimation of a vawt in dynamic stall. *Journal of Solar Energy Engineering*, 133(1):011006, 2011.

[7]C.J. Simão Ferreira, G. van Kuik, G. van Bussel, F. Scarano. Visualization by piv of dynamic stall on a vertical axis wind turbine. *Exp Fluids*, 2008.

[8]C.J. Simão Ferreira, H. Bijl, G. van Bussel, G. van Kuik. Simulating dynamic stall in a 2d vawt: Modeling strategy, verification and validation with particle image velocimetry data. *Journal of Physics*, 2007.

[9]F. Noca, D. Shields, D. Jeon. A comparison of methods for evaluating time-dependent fluid dynamic forces on bodies, using only velocity felds and their derivatives. *Journal of Fluids and Structures*, 1999.

[10]G. Brochier, P. Fraunie, C. Beguier, I. Paraschivoiu. Water channel experiments of dynamic stall on darrieus wind turbine blades. *ournal of Propulsion*, 1986.

[11]G. Tescione, D. Ragni, C. He, C.J. Simão Ferreira, G.J.W. van Bussel. Near Wake Flow Analysis of a Vertical Axis Wind Turbine by Stereoscopic Particle Image Velocimetry. Technical report, TUDelft, the Netherlands, 2013.

[12]L. Vita, U.S. Paulsen, T.F. Pedersen. A novel floating offshore wind turbine concept: New developments. *European Wind Energy Conference and Exhibition 2010*, pages 5:3952–3962, EWEC 2010.

[13]M. Kinzel, Q. Mulligan, J.O. Dabiri. Energy exchange in an array of vertical axis wind turbines. *Journal of Turbulence*, pages 13:1–13, 2012.

[14]N. Fujisawa, S. Shibuya. Observations of dynamic stall on darrieus wind turbine blades. *Journal of Wind Engineering and Industrial Aerodynamics*, 2001.

[15]N. Fujisawa, Y. Takeuchi. Flow visualization and piv measurement of flow field around a darrieus rotor in dynamic stall. *Journal of Visualization*, 1999.

[16]F. Noca. *On the evaluation of time-dependent fluid-dynamic forces on bluff bodies*. PhD thesis, California Institute of Technology, 1997.

[17]I. Paraschivoiu. *Wind turbine design: with emphasis on Darrieus concept*. . Polytechnic International Press, Montreal, 2002.

[18]S. Peace. Another approach to wind. *Mechanical engineering*, pages 126(6):28–31, 2004.

[19]T. Nakano, N. Fujisawa, Y. Oguma, Y. Takagi, S. Lee. Experimental study on flow and noise characteristics of naca0018 airfoil. Technical report, Department of Mechanical Engineering, Niigata University, 2006.

[20]W.A.Timmer. Two-dimensional low-reynolds number wind tunnel results for airfoil naca 0018. Technical report, Wind Energy Section, Faculty of Aerospace Engineering, Delft University of Technology, 2008.

Table 2. Measurement Cases for the Experiment.

		Coordinate System				
		Turbine		Traversing System		Azimuth Angle
	#	X [m]	Y [m]	X [m]	Y [m]	θ [°]
TSR = 2 & TSR = 4.5	1	0.11	0.489	0.61	0.489	0
	2	0.1	0.37	0.6	0.37	0
	3	-0.04	0.37	0.46	0.37	0
	4	-0.04	0.489	0.46	0.489	0
	5	-0.28	0.47	0.22	0.47	45
	6	-0.26	0.32	0.24	0.32	45
	7	-0.39	0.25	0.11	0.25	45
	8	-0.39	0.47	0.11	0.47	45
	9	-0.475	0.14	0.025	0.14	90
	10	-0.475	-0.1	0.025	-0.1	90
	11	-0.333	-0.22	0.167	-0.22	130
	12	-0.327	-0.353	0.173	-0.353	130
	13	-0.43	-0.375	0.07	-0.375	130
	14	-0.43	-0.2	0.07	-0.2	130
	15	0.1	0.489	0.6	0.489	180
	16	0.1	0.39	0.6	0.39	180
	17	-0.1	0.39	0.4	0.39	180
	18	-0.06	0.489	0.44	0.489	180
	19	0.48	-0.2	0.98	-0.2	235
	20	0.48	-0.37	0.98	-0.37	235
	21	0.36	-0.37	0.86	-0.37	235
	22	0.36	-0.2	0.86	-0.2	235
	23	0.51	0.1	1.01	0.1	270
	24	0.51	-0.11	1.01	-0.11	270
	25	0.48	0.37	0.98	0.37	305
	26	0.48	0.2	0.98	0.2	305
	27	0.36	0.2	0.86	0.2	305
	28	0.36	0.37	0.86	0.37	305

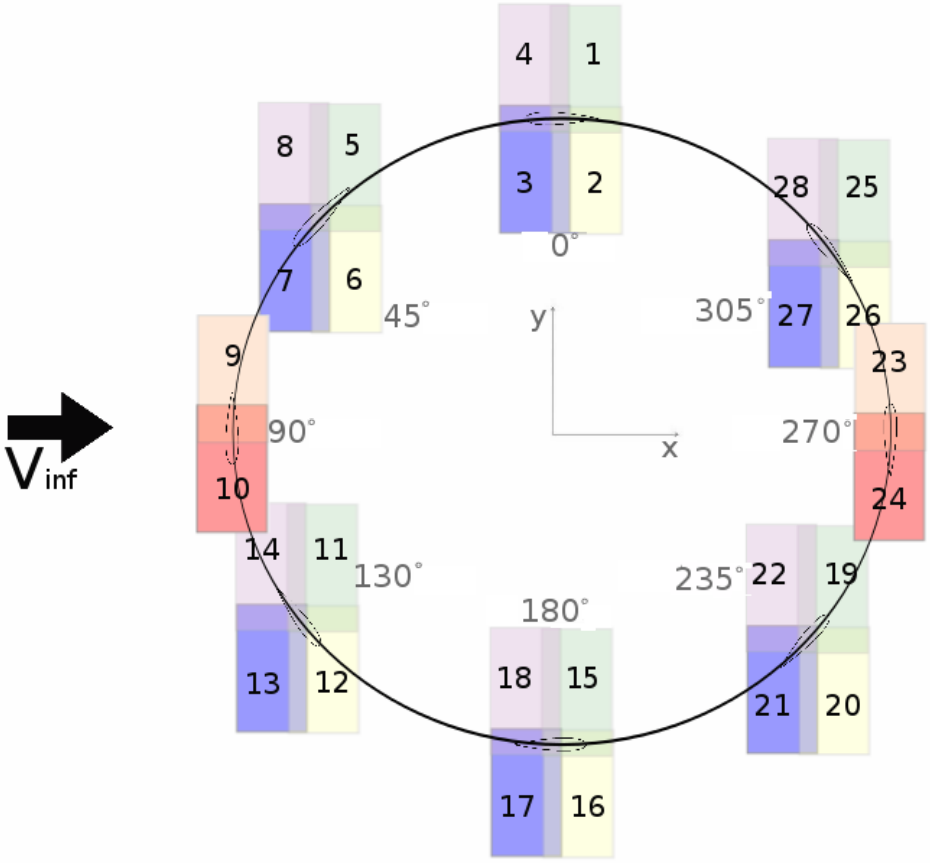

Figure 15. The different positions of the camera.

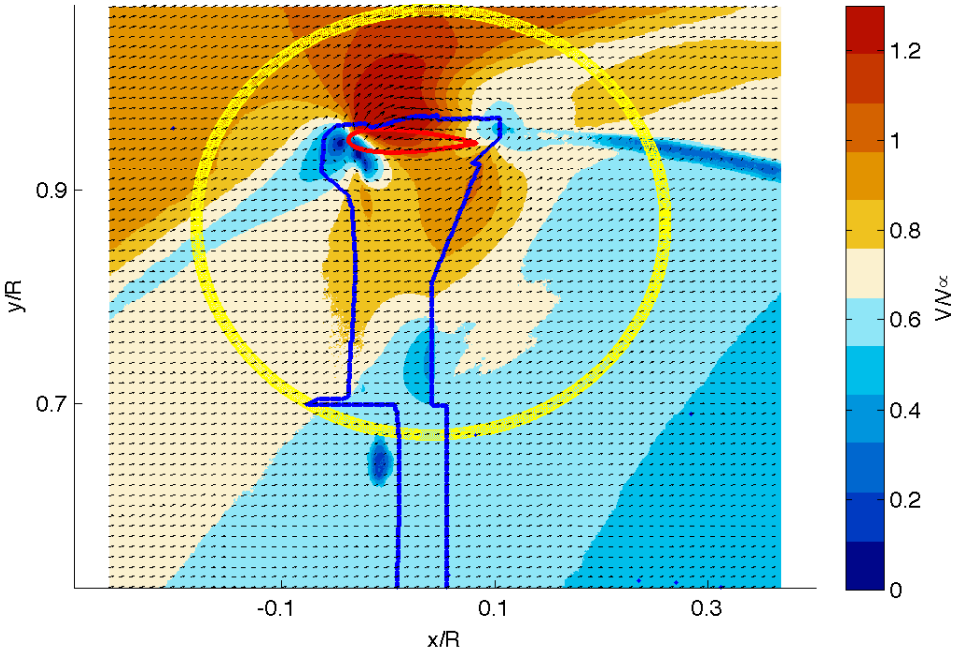

Figure 16. The Experimental Flow field for TSR 4.5 at Azimuth Position 0°.

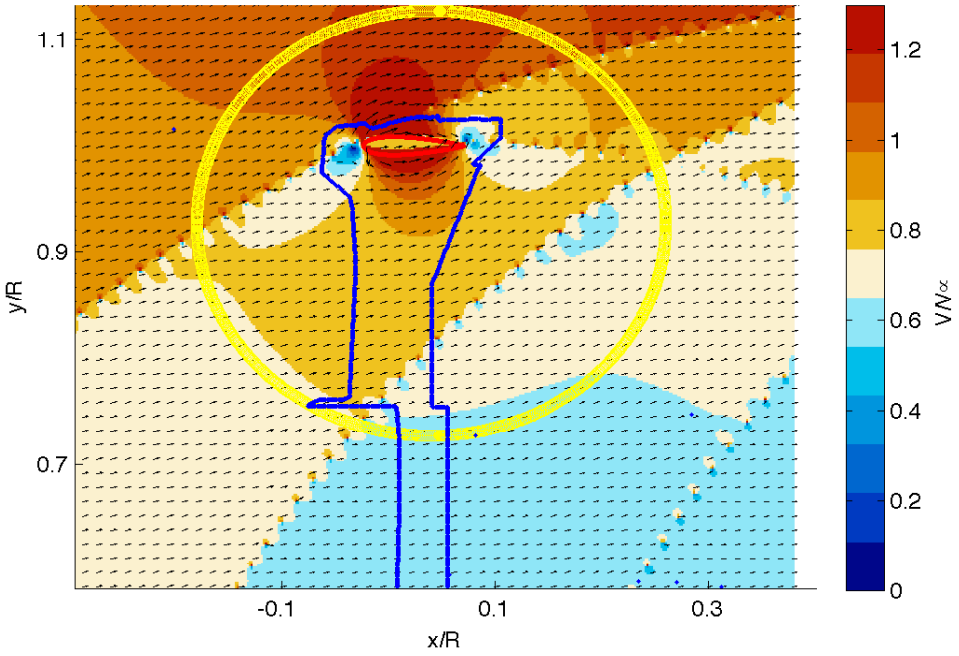

Figure 17. Vortex Model Flow field for TSR 4.5 at Azimuth Position 0°.

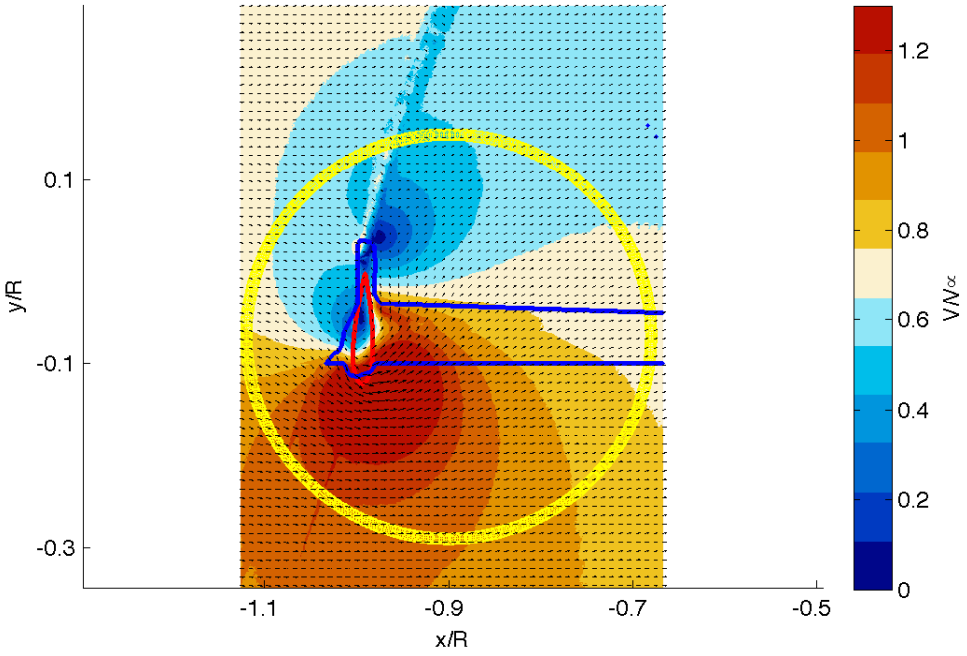

Figure 18. The Experimental Flow field for TSR 4.5 at Azimuth Position 90°.

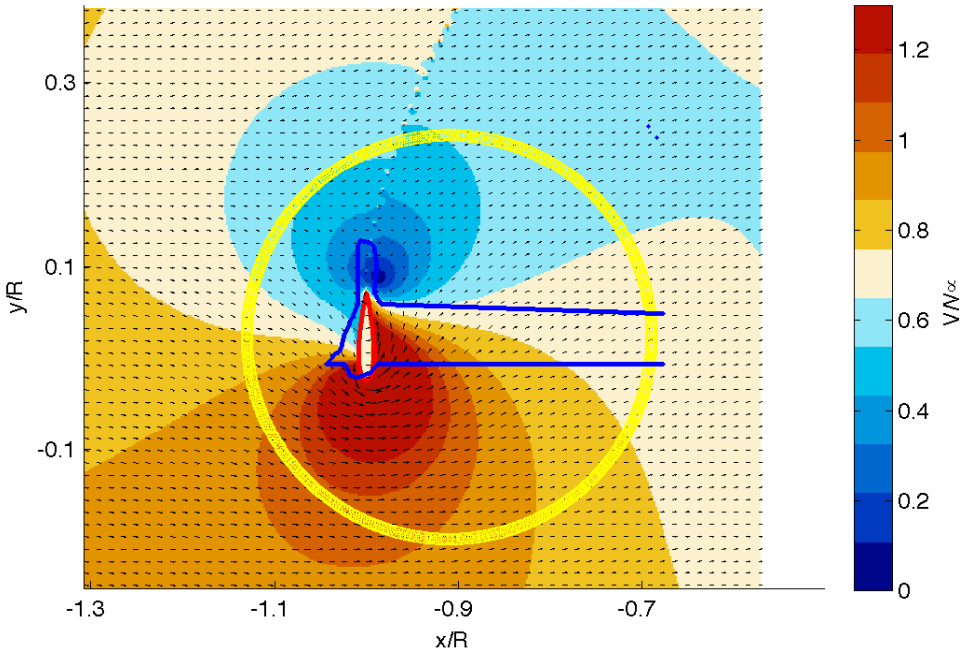

Figure 19. Vortex Model Flow field for TSR 4.5 at Azimuth Position 90°.

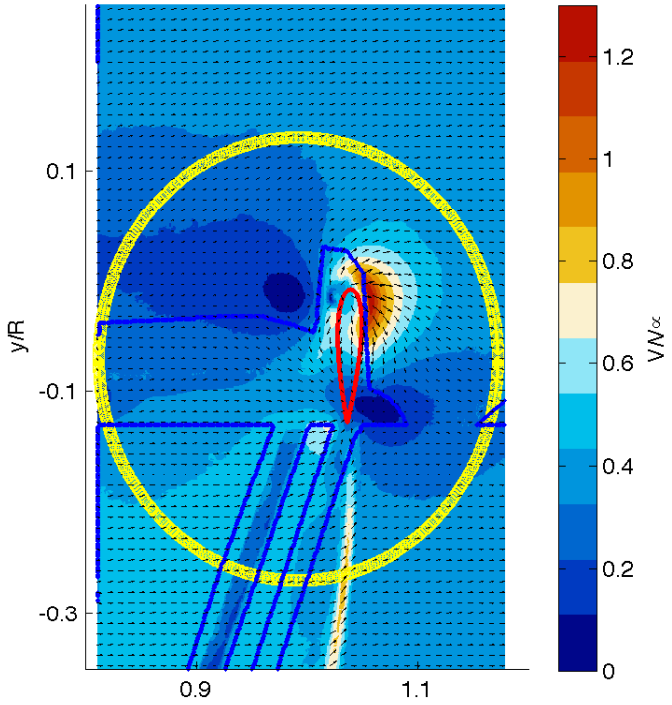

Figure 20. The Experimental Flow field for TSR 4.5 at Azimuth Position 270°.

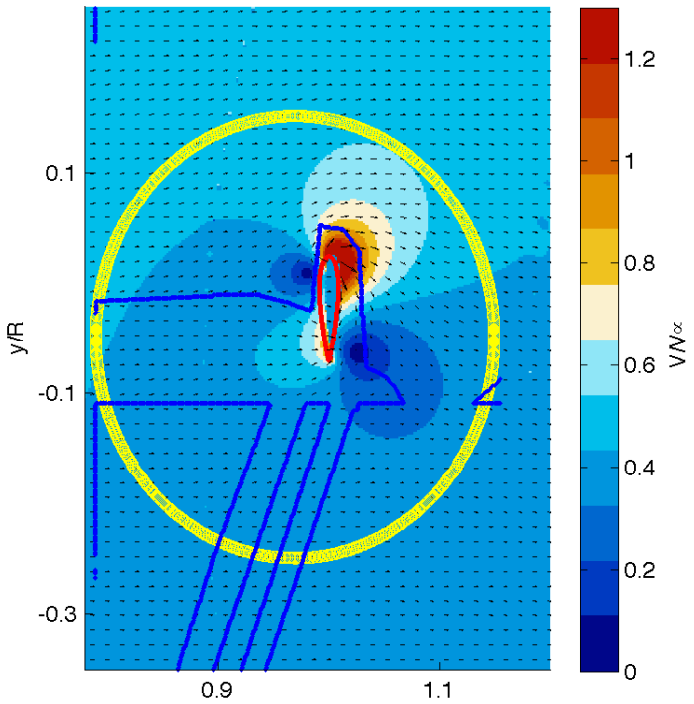

Figure 21. Vortex Model Flow field for TSR 4.5 at Azimuth Position 270°.

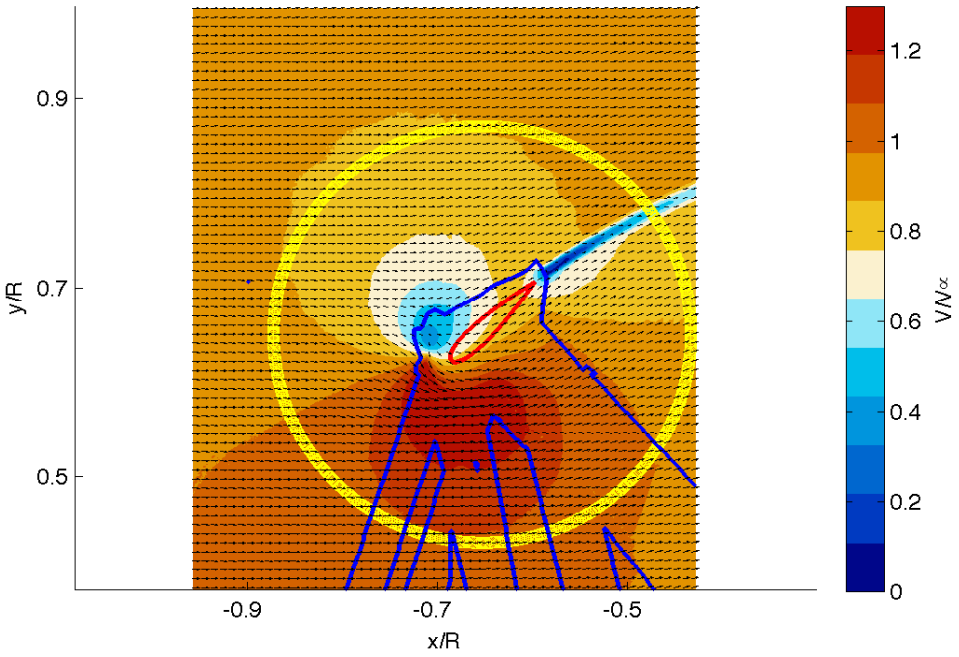

Figure 22. The Experimental Flow field for TSR 2 at Azimuth Position 45°.

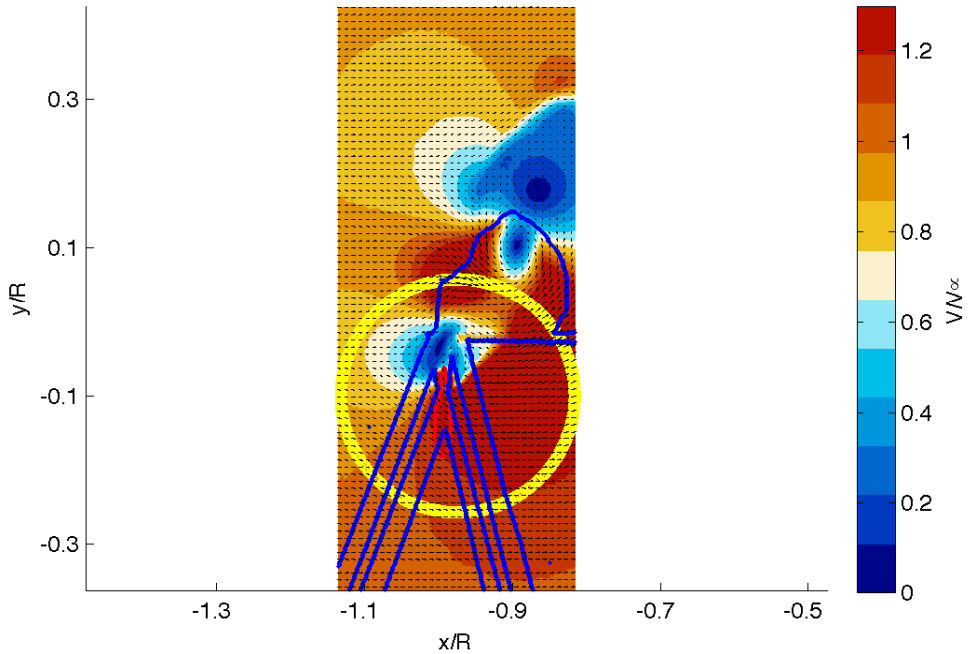

Figure 23. The Experimental Flow field for TSR 2 at Azimuth Position 90°.

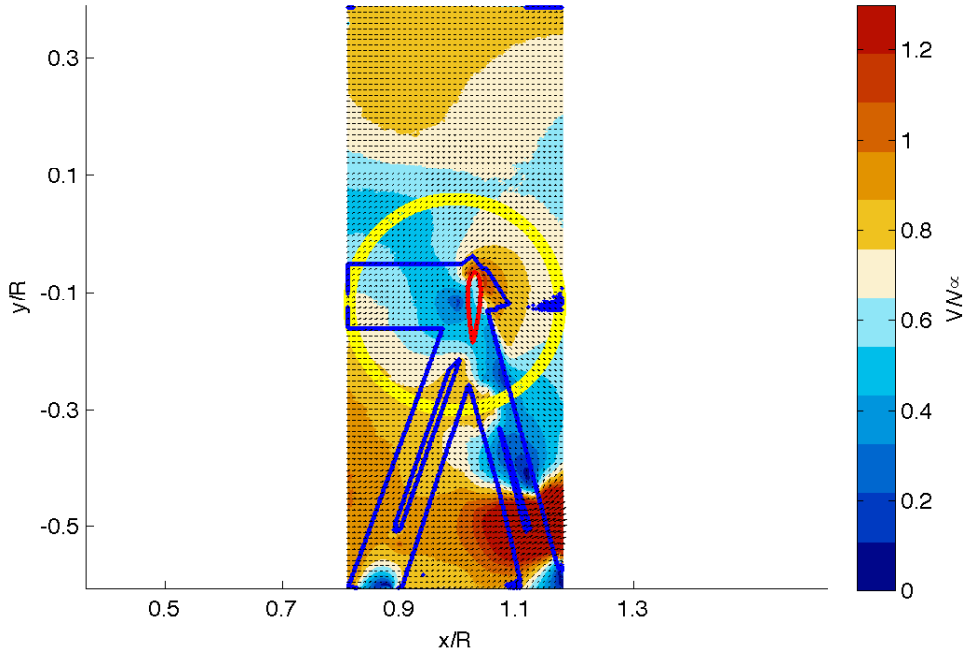

Figure 24. The Experimental Flow field for TSR 2 at Azimuth Position 270°.

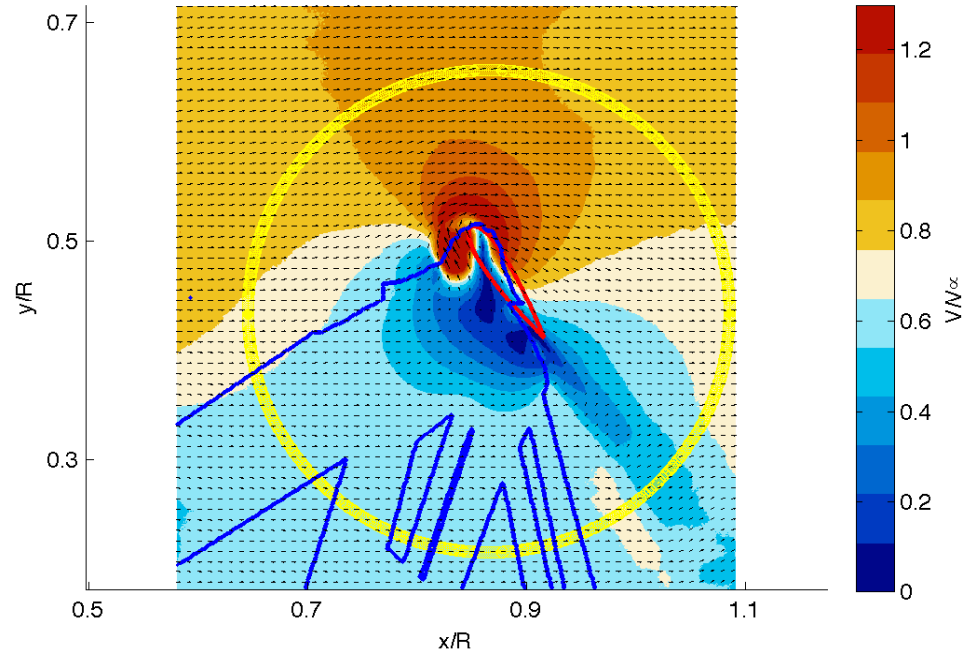

Figure 25. The Experimental Flow field for TSR 2 at Azimuth Position 305°.

Recent developments in the wind energy sector identify a potential cost reduction for offshore applications with VAWTs. Compared to HAWTs, VAWTs possess higher potentials for scalability, a simpler design due to the absence of yaw or pitch mechanisms and a lower center of mass, since the generator is not constrained at the top of the tower. It is believed that these advantages could lead to less maintenance and thus a lower cost. The prospect of the reduced costs and the possibility to displace the electric generator under water are of major interest in floating offshore applications. Moreover some previous studies on VAWT hypothesised a faster wake recovery, leading to a reduction of the turbine spacing and more clustered arrays in a wind farm scenario.

In order to supply the growing interest and questions of VAWTs, there is a need for more accurate numerical models. This can only be achieved by validating those numerical models on experimental data, and therefore many different experimental tests are required. The emphasis of this experiment lies on dynamic stall, thus especially lower TSRs are investigated.

Therefore, an experimental campaign using a phase-locked Particle Image Velocimetry (2C-PIV) technique has been conducted on an H-type Vertical Axis Wind Turbine (VAWT). The turbine is operated at tip speed ratios (TSR) 4.5 and 2, at accordingly average chord-based Reynolds number of 1.6 x 10^5 and 0.8 x 10^5. At both TSR, the velocity fields are presented in the mid (symmetry) plane of the blade for eight azimuthal positions. The velocity fields are directly derived from PIV, while the loads are obtained through an integral approach presented by Noca et al.

The overall goal of this research was to create a benchmark from the experimentally gathered loads, for validating and comparing different numerical models. The aim of evaluating the two different TSR is identifying the effect of Dynamic Stall (DS), which is not present at the higher TSR, while dominant at the lower. The DS phenomenon is numerically computationally expensive to model all scales of phenomena, so a solid benchmark for a VAWT in DS is of great interest.

In this thesis project the Velocity fields and the loads for both cases are presented, and a first comparison with different numerical models is performed.

Dieter Castelein